TECHNISCHE UNIVERSITÄT WIEN

DISSERTATION

Solar cells with electrodeposited cuprous oxide absorber and atomic layer deposited zinc-magnesium-oxide buffer

Ausgeführt zum Zwecke der Erlangung des akademischen Grades einer Doktorin der technischen Wissenschaft

unter der Leitung von

O. Univ. Prof. Dr. phil. Emmerich Bertagnolli
am Institut für Festkörperelektronik

und

Dr. Theodoros Dimopoulos
am Center of Energy - Photovoltaic Systems
AIT Austrian Institute of Technology

Eingereicht an der Technischen Universität Wien
Fakultät für Elektrotechnik und Informationstechnik
von

Jatinder Kaur
Matrikelnummer 1526614

Wien, am 10. Juni 2018 _____

ABSTRACT

In order to foster the deployment of photovoltaics (PV) at the terawatt scale, the research for low-cost, earth-abundant and non-toxic PV materials, as well as cost-efficient fabrication processes, is intensified. Metal oxide semiconductors are today widely applied in PV as transparent conductors (transparent conductive oxide or TCOs) and functional interfacial layers. Some of these oxide semiconductors are even use as active solar absorbers, as they have appropriate bandgap to harvest a wide part of the solar spectrum. They are attractive materials as they can serve much functionality in a PV cell, chemically stable and a large number of them are non-toxic and abundant. Most importantly, they can also be fabricated by cost-effective, vacuum- and solution-based fabrication methods, in the form of thin films and nanostructures. This thesis concerns the investigation of metal oxide semiconductor solar cells, based on heterojunction of the cuprous oxide (Cu_2O) absorber and magnesium-doped zinc oxide (ZnMgO) buffer. We focus on the development of the single layers and the formation and engineering of the Cu_2O/ZnMgO heterojunction, so as to optimize the solar cell power conversion efficiency.

Cu_2O, the most investigated metal oxide absorber, is a p-type semiconductor with a band gap of ~2 eV, which makes it theoretically possible to yield efficiencies up to ~20% for single-junction solar cells (Shockley-Queisser limit). Cu_2O is non-toxic, abundant and can be fabricated with non-vacuum deposition techniques, such as by electrochemical deposition (ECD). ECD is a solution-based fabrication process, in which the material usage and energy consumption is very low, while it is easily up-scalable to industrial-scale production. It is therefore an ideal fabrication method for low-cost, thin-film solar cells.

A suitable n-type layer, forming the heterojunction with the p-Cu_2O, is vital to obtain high power conversion efficiencies. Most important is the conduction band alignment at the p/n heterojunction. Zinc oxide (ZnO) is one of the most studied heterojunction partner for Cu_2O. It is an intrinsic n-type semiconductor with a wide band gap of 3.4 eV, but its conduction band alignment with Cu_2O is far from ideal. Doping the ZnO with Mg offers the possibility to modify the electronic band structure of the material. By increasing the Mg content, the bandgap of ZnMgO increases, while the crystal structure of ZnO is maintained. The increase of bandgap is accompanied with a smaller electron affinity, which improves the alignment of the conduction band with Cu_2O.

Further, to control the defect density at the Cu_2O/ZnMgO interface, the atomic layer deposition (ALD) method is employed for the fabrication of the ZnMgO layer. ALD is a vacuum technique, widely applied in the semiconductor industry and of high-potential for thin-film PV. It is based on the sequential and self-limiting surface reactions to produce films of high quality and unsurpassed homogeneity even on 3-dimensional substrates.

In the thesis we also sought to replace precious metals, used as solar cell electrodes in the literature, with lower-cost alternatives. The optimized solar cells in this thesis are precious-metal-free, almost exclusively composed of metal oxide semiconductor layers. For this, a highly conductive and reflective electrode, based on chromium (Cr) and indium-tin-oxide (ITO) was developed by sputtering. The ECD absorber deposition was optimized for the Cr/ITO electrode, in order to obtain void-free and large-grain Cu_2O films. Finally, sputtered aluminum-doped ZnO (AZO) was used as front transparent contact to complete the solar cell. Best cells showed promising PV performance, with short circuit current density of 6.8 mA/cm^2, open circuit voltage of 550 mV, fill factor of 45% and power conversion efficiency of 1.67%.

ACKNOWLEDGMENTS

I would like to acknowledge a number of people for their support and encouragement throughout my doctoral study. First and foremost, I am incredibly grateful to my supervisors, Dr. Theodoros Dimopoulos, Photovoltaic System, Austrian Institute of Technology, and Prof. Emmerich Bertagnolli, Vienna University of Technology, for providing me with the opportunity to conduct this research work, for the continuous assistance and invaluable suggestions over the years. It has been a pleasure working with you both. Further, I would like to thank Dr. Ole Bethge, Vienna University of Technology for his guidance and encouragement during my stay at TUWien.

I would like to thank all my fellow group members from Photovoltaic System at AIT for creating a pleasant working environment. Thank you all.

I would like to thank my university fellow group members for being supportive and helpful. Thank you Dr. Bernhard Lutzer, Silvia Greil, Erich Riegler.

Further, special thanks to my friends Imran, Neha and Ankit for their love and support.

Finally, I would like to express my heartwarming gratitude to my family who greatly supported my studies and encouraged me. Special thanks to my relatives and friends in India for their unconditional love and support.

Table of Contents

List of symbols

A	area	n	number of electrons transferred
Ag	silver	N_A	acceptor carrier concentration
Au	gold	N_D	donor carrier concentration
Cr	chromium	n_i	intrinsic carrier concentration
D	diffusion coefficient	OH^-	hydroxide ion
E	electric field	P_{in}	incident power
e	charge of an electron	q	electric charge
E_C	conduction band	R	gas constant
E_F	Fermi level	R_s	series resistance
E_g/E_G	band gap	R_{sh}/R_p	shunt resistance
E_V	valence band	T	temperature
F	Faraday constant	Ti	titanium
FF	fill factor	V	voltage
ΔG_e	electrochemical activation energy	V_{bi}	built-in voltage
h	Planck constant	V_{mp}	voltage at maximum power point
I_{mp}	current at maximum power point	V_{OC}	open circuit voltage
J	current density	*w*	depletion region width
J_{max}	maxima in current density (ECD)	α	absorption coefficient
J_0	reverse saturation current	α_A	anodic charge transfer coefficient
J_{ph}	photo-generated current	α_C	cathodic charge transfer coefficient
J_{SC}	short-circuit current density	ε	dielectric constant
k_B	Boltzmann constant	ε_0	permittivity of free space
L_e	diffusion length of electron	λ	photon wavelength
L_h	diffusion length of hole	ν	photon frequency
M	molar mass	τ_e	lifetime of electron
n	ideality factor	τ_h	lifetime of hole

List of Abbreviations

ALD	atomic layer deposition
AZO	Al doped Zinc oxide
CE	counter electrode
Cu_2O	cuprous oxide
CuO	cupric oxide
CH_3 CH (OH) COOH	lactic acid
$CuSO_4.5H_2O$	copper (II) sulfate pentahydrate sulfate
CV	cyclic voltammetry
C-V	capacitance voltage
ECD	electrochemical deposition
FTIR	fourier transform infrared spectrometer
ITO	indium doped tin oxide
j-V	current density voltage
NaOH	sodium hydroxide
PCE	power conversion efficiency
PV	photovoltaic
PLD	pulsed-layer deposition
RE	reference electrode
RF	radio-frequency (sputtering)
SE	spectroscopic ellipsometry
SEM	scanning electron microscopy
WE	working electrode
XPS	X-ray photon spectroscopy
XRD	X-ray diffraction
ZnO	zinc oxide
ZnMgO	magnesium-doped zinc oxide

Chapter 1

Introduction

1.1 Motivation

The global primary energy resources rely mainly on fossil fuels, in the form of coal, oil, and natural gas. However, combustion of fossil fuels produces air pollutants, such as nitric, sulfuric and carbonic acids, which have serious consequences on our climate. The release of CO_2, a main greenhouse gas, from anthropogenic sources, has an adverse impact on global temperature and sea levels, a phenomenon known as global warming. At present, the amount of CO_2 in the atmosphere is $3.5 * 10^{12}$t [1] and results could be disastrous, if this amount continues to rise.

The increase in environmental problems and world population demands clean energy, which has stimulated the utilization of renewable sources such as solar, wind, geothermal, hydropower. The world currently faces one of the biggest challenges for the deployment of renewable energy sources. The progress is steady but it needs to be largely intensified in order to make a significant impact in the immediate future. For this to happen, also the research in clean energy resources must be encouraged and firmly fostered.

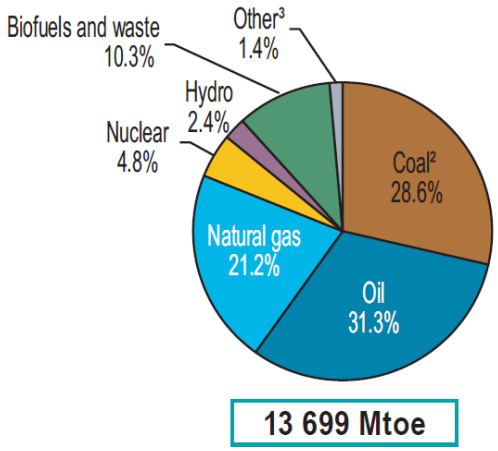

Figure 1.1: World's total primary energy supply by fuel (Mtoe) in 2014

According to the International Energy Agency (IEA), in 2014, the world's total primary energy supply was approximated to 13,699 Mtoe (Million tons of oil equivalents, corresponding to 18 TW-year) as shown in Figure 1.1. Fossil fuels represent the lion's share with 81.1% of total energy, whereas renewable energies based on solar photovoltaics, solar thermal, geothermal, wind, tide/wave/ocean and others, supplied only 1.4% of the total energy. Due to population and economic growth, different scenarios have been proposed for our future energy needs. The global energy consumption will raise the demand for energy to 27 TW by 2050, and more than triple the demand to 45 TW by 2100 [2]. At the same time, the global movement for 100% renewables is gaining continuously momentum, especially since the Paris City Hall Declaration, which calls for 100% renewable energy or 80% reductions in greenhouse gas emissions by 2050 [3].

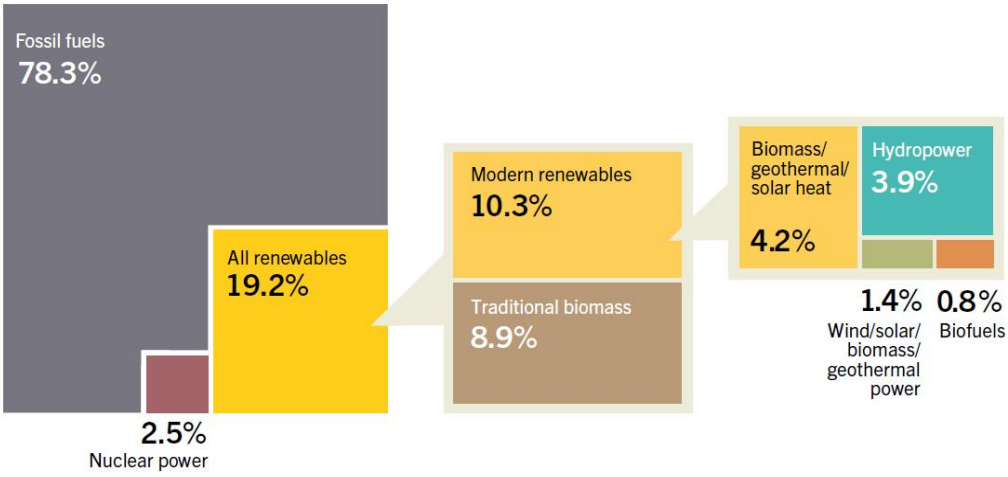

Figure 1.2: Estimated Renewable Energy Share of Global Final Energy Consumption, 2014 [3]

Renewable energy is the world's fastest growing energy source, increasing by 2.6% per year. According to the Global energy consumption in 2014, an estimated share of 19.2% was provided by renewable energies [3]. Figure 1.2 shows the renewable energy share of global energy consumption in 2014.

Solar photovoltaics' is a major pillar of renewable energy production. The installed PV capacity continuously grows for more than a decade. In 2017, the solar PV market experienced record growth, adding 98 GW new installations, to attain total installed PV capacity of 402 GW (figure 1.3). Despite this fast growth, for PV to make significant impact in the future's energy mix, it needs to be deployed in the TW scale. To achieve this, decreasing

the PV cost, increasing the power conversion efficiency and increasing its production throughput, is necessary.

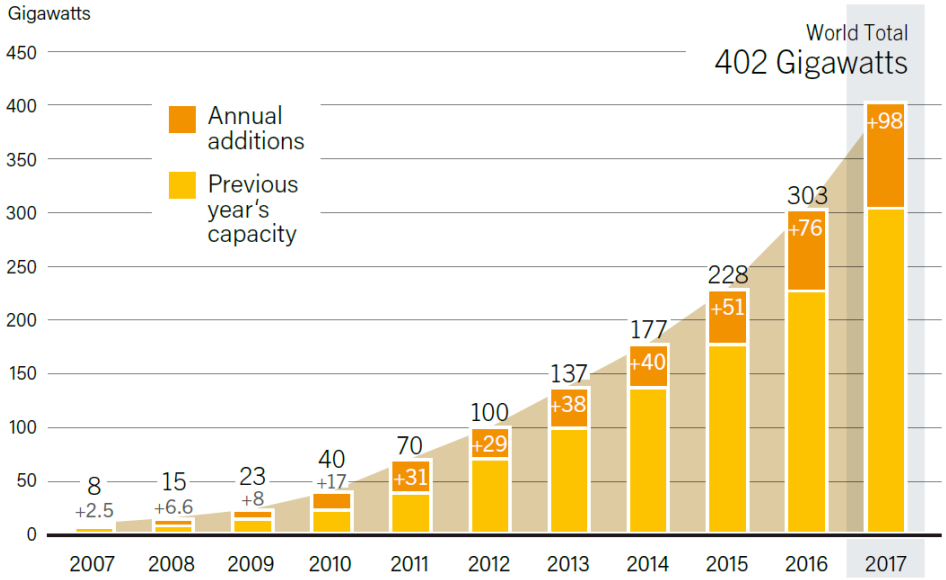

Figure 1.3: Solar PV Global Capacity and Annual Additions, 2007-2017 [4]

Today, 93% of the PV production is crystalline silicon (c-Si) modules, a technology based on mono- or poly-crystalline Si wafers, with a thickness of ~200 μm, having cell and module efficiency of 26.7% and 24.4%, respectively [5]. c-Si technology is mature and efficient but has reached its limits in cost reduction and efficiency increase. Also, it uses thick and fragile wafers, which keeps material consumption high and does not allow flexible applications.

In terms of reducing cost, thin-film PV (TFPV) technologies, representing approx. 7% of the current PV production, are a great alternative to c-Si, due to their lower material usage and inexpensive manufacturing, also by roll-to-roll processes employing flexible substrates, like plastic or metal foils. These features are possible because TFPV technologies are based on semiconductor compound absorbers with a direct energy bandgap (in contrast to silicon), which permits to capture light efficiently and transform it into electricity, even for very small absorber thicknesses (in the order of 1-2 μm). These absorbers, such as the commercial CdTe and Cu-In-Ga-S (Se) (CIGS) can be deposited by vacuum and solution-based techniques and lead to solar cells with efficiencies of 21% and 21.7%, respectively [5] i.e. close to c-Si.

However, CdTe and CIGS technologies have issues regarding the toxic nature of cadmium and the scarcity of tellurium and indium. With a focus on TW deployment, the materials

availability is a serious concern for these TFPV technologies [6]. Also, the rising demand of indium and tellurium will increase prices, which deteriorates the cost advantages of CdTe and CIGS technologies. Therefore, the search for low-cost, chemically stable, earth-abundant, non-toxic materials with cost-efficient fabrication procedure is essential for the solar cells applications.

The transition metal oxides have a great potential to fulfill these requirements. *Wadia* et al. [7] examined 23 inorganic semiconductors as PV absorbers, based on the dual constraints of performance and least cost-per-watt. Among them, cuprous oxide (Cu_2O), a compound semiconductor, is a one of the most promising candidates for TFPV applications. There are several advantages of using Cu_2O as PV absorber, such as (1) its non-toxic nature, (2) abundance of the starting material (copper), (3) can be prepared with simple methods at very low cost.

The Cu_2O is a p-type semiconductor, with a direct band gap of 1.9-2.1 eV [8], which gives a theoretical limit of energy conversion efficiency of about 20%. At the moment, the reported power conversion efficiency for Cu_2O-based solar cells is below this limit. The highest efficiencies of 8.1% are achieved for thermally oxidized Cu_2O-based solar cells [9]. However, excessive material usage and high temperature make the thermal oxidation fabrication method unsuitable for large-scale production. In comparison, the electrochemical deposition (ECD) of Cu_2O has a large potential as it takes place close to room temperature and from solutions of low-cost chemical reagents. In addition, ECD is easily up-scalable, high throughput and roll-to-roll compatible. To create a working solar cell, the p-type absorber needs to be combined with an n-type "window" layer, to form the heterojunction. The use of atomic layer deposition (ALD) to deposit the n-type layer has been shown to improve the interface quality at the heterojunction and lead to increase efficiencies [35].

1.2 Goal of this thesis

In this thesis, the properties of the ECD-Cu_2O absorber combined with ALD-grown $Zn_{1-x}Mg_xO$ layers are investigated. The main goal of this work is to enhance the photovoltaic performance of ECD-Cu_2O/ALD-$Zn_{1-x}Mg_xO$ heterojunction solar cells by optimization of the deposition of the different material components (electrodes, absorber, window layer, etc) and by careful engineering of the heterojunction energetics (energy band alignment). At the same time, the major focus was on the employment of low-cost materials and processes

which are up-scalable to industry standards. More in detail, we have optimized the electrochemical deposition of the Cu_2O absorber on the precious-metal-free, conductive electrode so as to obtain suitable absorber properties. Next, the $Zn_{1-x}Mg_xO$ layers were investigated as a function of Mg content in order to improve the band alignment at the p/n heterojunction. Finally, the PV performance of the $Cu_2O/Zn_{1-x}Mg_xO$ heterojunction solar cells was investigated as a function of the Mg content.

Chapter 2

Theoretical background

The aim of this chapter is to describe the basic concepts related to the solar cell device operation for efficient photovoltaic energy conversion. The first section of the chapter is devoted to the PV basics and the working principle of a solar cell device. The second section describes the different fabrication architectures of solar cells in order to efficiently harvest the solar energy to maximize the power conversion. Then, in the end, earth abundant cuprous oxide (Cu_2O) material properties and a brief history of Cu_2O-based solar cells is discussed together with the Zinc oxide (ZnO) material properties.

2.1 Basic solar cell concepts

One way to exploit the solar energy is by converting it into electricity through the use of photovoltaic cells, also called solar cells. The photovoltaic (PV) effect was discovered by *Edmond Becquerel* in 1839[10] for an electrochemical type of cell. Currently, in their most familiar form, solar cells are solid state semiconductors diodes.

The operation of such a cell is based on the absorption of light by a semiconductor absorber and the subsequent generation of electron-hole pairs. The electrons and holes are subsequently separated by the electric field present in the solar cell device and the charge carriers are then transported to an external electrical circuit, generating power. The photovoltaic energy conversion can be broken down into 4 essential parts (see figure 2.1), briefly explained in the following sections.

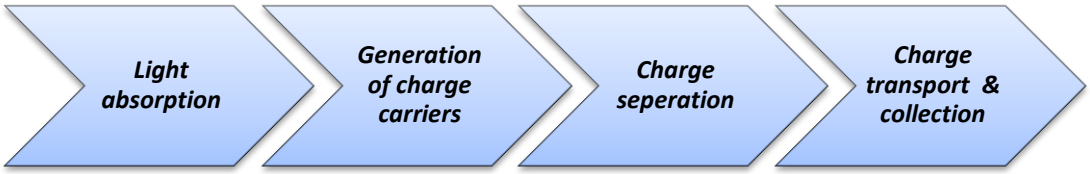

Figure 2.1. The essential steps of photovoltaic energy conversion

2.1.1 Light absorption

2.1.1.1 Solar radiation

The sun light provides a wide spectrum of electromagnetic radiation. The amount of energy received from the sun per unit area per unit time defines the spectral irradiance. Figure 2.2 shows the spectral irradiance as a function of wavelength for direct sunlight at the top of the earth's atmosphere and at sea level. The spectrum of the solar radiation very closely matches that of a black body. The solar spectrum covers a part of the ultraviolet (UV), the visible (VIS) and the near-infrared (NIR) window, up to ca. 2500 nm. The main spectral range of the solar radiation flux is in the visible region, with a maximum at about 550 nm. At sea level the spectral irradiance is attenuated due to the light losses in the atmosphere.

As the solar radiation passes through the earth's atmosphere, some of it is absorbed or scattered by molecules, such as water and CO_2. The ozone layer (O_3), situated at 20-30 km from the earth's surface absorbs about 98% of the UV radiation. Some of the radiation is reflected straight back out into space, whilst the rest reaches the earth's surface. Once the radiation arrives at the surface, some of it is reflected back into the sky. As a consequence, after the absorption and dispersion in the atmosphere, the spectral range of solar radiation flux reaching the earth's surface is changed. About 8.03% of the radiation reaching the earth's surface is in the UV range, 46.41% in the visible and the rest 46.40% falls into the NIR.

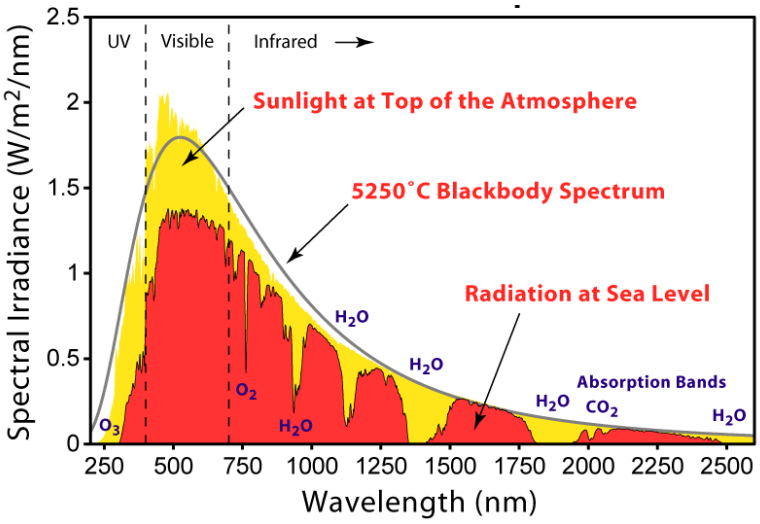

Figure 2.2. The solar radiation spectrum [11]

The attenuation of the sun's radiation flux in the earth's atmosphere is characterized by the quantity called air mass (AM), which mathematically is expressed as the secant of the solar

zenith angle (θ) i.e. secθ. There are different types of AMs. AM0 signifies the solar spectrum outside the earth's atmosphere (extra-terrestrial spectrum) and is mostly used as reference for space solar power systems. AM1 corresponds to the sunlight passes through an air mass of one i.e. the sun is directly overhead with $\theta=0^0$. The intensity of the solar radiation weakens with the sun's angle approaching the horizon, since the rays have a larger path in the atmosphere, or air mass, to penetrate. An efficient PV system design has to take into consideration these variations associated with the solar spectrum. The most widely used air mass for the PV testing is AM1.5. It corresponds to sun irradiance at angle with the earth's surface given by $\theta= 48.2^0$. AM1.5 is utilized as reference for evaluating the performance of solar cells for terrestrial use.

2.1.1.2 Solar absorber

The solar absorber has a pivotal role in the solar cells, since this is where the light is absorbed to generate electrical carriers. The optical properties of semiconductors define the suitable candidates to serve as solar absorbers. The degree, to which photons are absorbed, is related to the *optical bandgap* (E_g) of the semiconductor. Depending on the energy band structure, semiconductors can have either a *direct* or *indirect band-gap*. *Direct band gap* occurs when the conduction band (CB) minimum and valence band (VB) maximum occur at the same momentum (*k* value), i.e. the transition from the VB to the CB does not require change of the electron's momentum. On the other hand, for the *indirect band gap*, the CB minimum and VB maximum occur at different momentum values, a change of the electron's momentum is required for its transition, provided by the crystal, in the form of a phonon.

The solar spectrum spans photon energies from 0.5 to 3.5 eV. In 1961, *Shockley* and *Queisser* [12], through the so-called "detailed balance analysis" approach, predicted the maximum power conversion efficiency limit of an ideal single junction solar cell, by taking into account the fundamental intrinsic radiative recombination losses. The first intrinsic loss is related to the inability of a single energy band-gap solar cell to properly match the broad solar spectrum. The second loss is related to the radiative recombination, as explained in-detail in section 2.1.2 (figure 2.4). The calculation indicates that the maximum power conversion efficiency limit is 33% under AM1.5 light. This maximum is marked for a solar absorber with a direct bandgap of 1.34 eV. Figure 2.3 (a) illustrates the graph of theoretical conversion efficiencies as a function of absorber band gap according to the *Shockley and Queisser* limit.

Energy loss mechanisms in the semiconductor are illustrated in figure 2.3 (b). Some of the photons are reflected from its surface, depending on the incident angle of the photon and the surface structure of the semiconductor. If the photons have energies lower than the band gap then they cannot contribute to the output power as shown in (1). The photons with excess energy as compared to the band gap generate carriers with higher kinetic energy and this energy will contribute to heat (charge carriers thermalize to the band edges) as shown in (3). Only photons with energies matching the band gap can be harvested without energy loss (2).

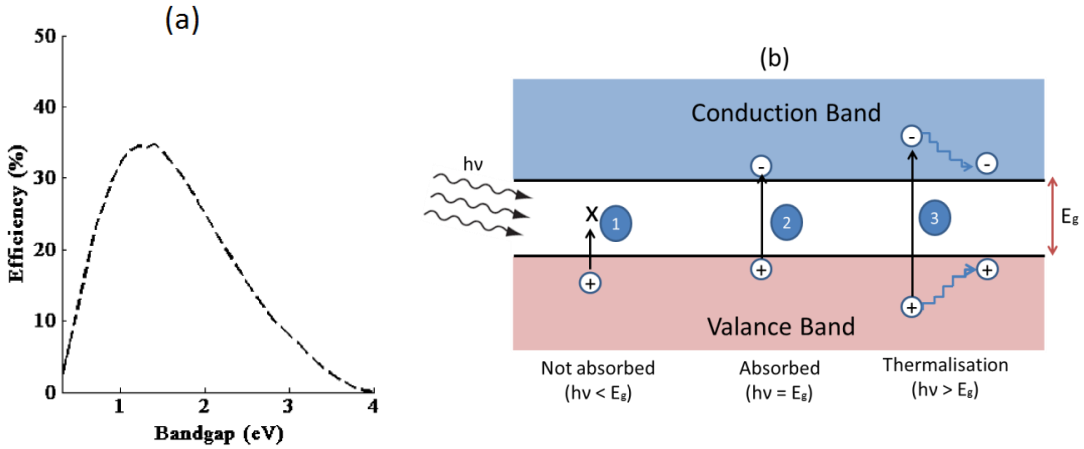

Figure 2.3. (a) Theoretical conversion efficiencies based on Shockley and Queisser limit [13], (b) three optical phenomena in the semiconductor material when exposed to solar radiations

The probability for the absorption of a photon of energy hv is defined by the absorption coefficient α (hv). It is an important material property of a semiconductor that determines how far into the semiconductor light of a particular wavelength can penetrate before it gets absorbed. The indirect band gap semiconductor, usually, has a smaller absorption coefficient than a direct band gap semiconductor. As a reference, for 600 nm, α is about $10^5 cm^{-1}$ and $10^6 cm^{-1}$ for indirect (e.g. Si) and direct (e.g. GaAs) band-gap semiconductor, respectively [14].

The optical properties of semiconductors are characterized by the complex refractive index, $\tilde{n} = n - ik$ where the real part n is called the refractive index and determines the propagation velocity of light in the medium, whereas the imaginary part k is called the extinction coefficient and determines the light absorption. The absorption profile of photons

is calculated by using the Lambert-Beer absorption formula. The intensity I of light travelling in a homogeneous absorbing medium reduces exponentially as:

$$I(x) = I(0)e^{-\alpha.x}$$

where *I(0)* is the initial intensity, x is the path length and α is the absorption coefficient. The extinction coefficient *k* is related to the absorption coefficient α by the relation $k = \alpha\lambda/4\pi$. This intrinsic property is very efficient in determining which material is useful for solar cell light absorber. The inverse of the absorption coefficient is called the absorption length.

For an efficient solar cell, absorbers with appropriate band-gap and absorption coefficient are necessary. If *indirect band-gap* semiconductors are utilized as PV absorbers then they need to be much thicker than *direct band-gap* semiconductors, in order to absorb the same amount of photons. In terms of reducing material consumption, thin layers of direct bandgap semiconductors are advantageous. Taking into account the above, the absorber's band gap should be in the optimum range (~1.3 eV), as predicted by detailed balance analysis, with a high absorption coefficient. For large-scale deployment, the absorber should also be abundant, stable and of low environmental impact.

2.1.2 Charge generation and recombination

Charge generation occurs when the semiconducting material absorbs photons and excites electrons to the CB, leaving a hole in the VB, thus creating electron-hole pairs. These free charge carriers in CB (electrons) and VB (holes) can be used for electric current before they recombine.

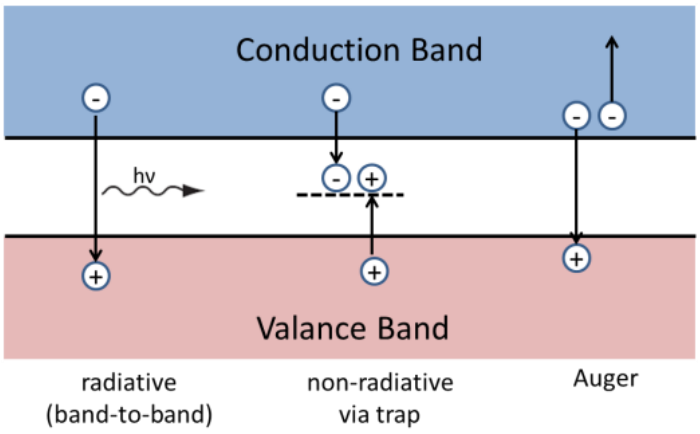

Figure 2.4. The recombination process in semiconductors

There are three types of recombination occurring in semiconductors, *radiative* (band-to-band) *recombination*, *Auger recombination,* and *Shockley-Read-Hall* (SRH) *recombination*. The recombination processes are shown in figure 2.4. **Radiative recombination** is the opposite of absorption, in which an electron from the conduction band recombines with a hole in the valence band, leading to the generation of a photon. **Auger recombination** is a three carrier's process, in which an electron and a hole recombine in a band-to-band transition, but rather than emitting the energy as heat or as a photon, the energy is given to a third carrier, an electron in the conduction band. This electron later thermalizes to the conduction band edge. Recombination via defect levels is called **Shockley-Read-Hall (SRH) recombination**. The defect energy levels within the band-gap are caused by the presence of impurities or structural defects. They are also called trap levels because they act as traps for charge carriers. These levels can facilitate a two-step recombination process where conduction electrons are trapped in the defect level and then relax to the valence band, thereby annihilating a hole in the process [15].

2.1.3 Charge separation, transport and collection

After the photo-generation of electron-hole pairs, the electrons and holes need to be separated and transported at the opposite device terminals before they recombine, in order to perform work in an external circuit. A *p-n* junction of two semiconductor materials with different electronic properties is used to separate and transport the photo-generated electron-hole pairs. This takes place by two mechanisms. One is carrier drift, which is induced by the built-in electric field at the *p-n* junction, driving electrons and holes at opposite directions. The other is carrier diffusion from regions of higher to lower concentration. The *p-n junction* and the aforementioned drift and diffusion mechanisms are briefly explained in the following:

In its most common form, a solar cell is a *p-n* junction, where a p-type (high hole concentration) semiconductor is in contact with an n-type (high electron concentration) semiconductor material. If the p- and n-type regions are made from the same semiconductor (using different dopants) the structure is called a **homojunction** and if they made from different semiconductors, then it is referred as **heterojunction**. Holes are majority charge carriers and electrons are minority carriers in the p-region, while the opposite holds in the n-region. In an intrinsic semiconductor, the Fermi level lies around the middle of the bandgap. In a p-type semiconductor it is closer to the VB, while in the case of an n-type material it lies closer to the CB.

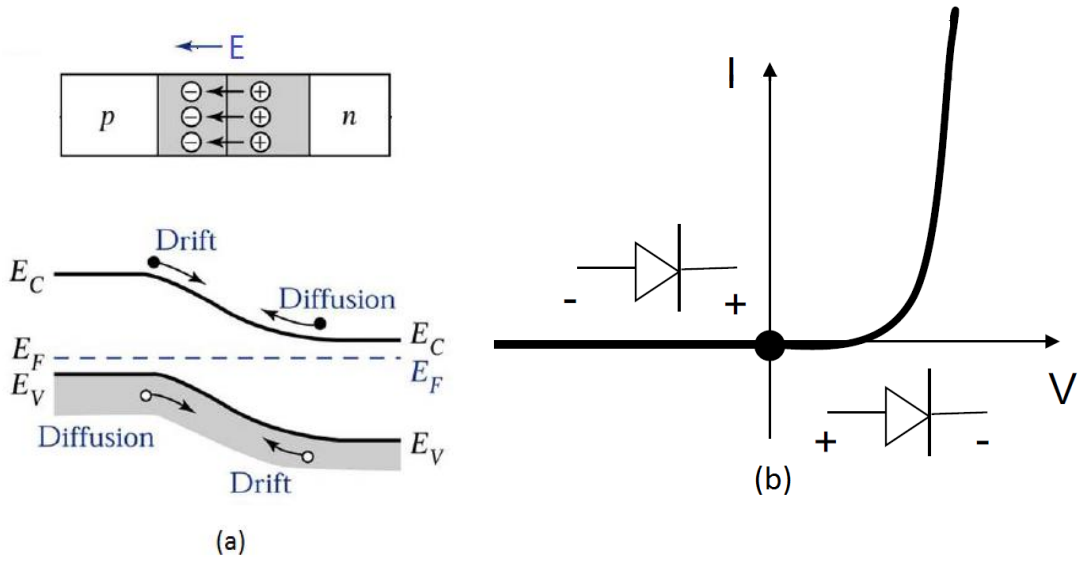

Figure 2.5. (a) p-n junction under equilibrium, (b) the corresponding IV characteristic of diode under dark for the forward bias and reverse bias conditions with diode symbol [16]

When the p-type and the n-type regions are joined, a carrier concentration gradient forms at the interface. This gradient leads to the diffusion of holes from the p-region into the n-region leaving behind immobile negative ions as shown in the figure 2.5 (a). Similarly, the diffusion of electrons from the n-region into the p-region leaves behind immobile positive ions. The system eventually reaches equilibrium, with the CB and VB shifting in such way that the Fermi levels of the p-and the n-region are aligned. The region of immobile ions at the junction is referred as **depletion region** or **space-charge region**. This region is depleted of mobile charge carries and creates a built-in voltage across the interface, which varies as a function of donor and acceptor carrier concentrations and can be expressed as:

$$V_{bi} = \frac{kT}{q} ln\left(\frac{N_D\, N_A}{n_i^2}\right)$$

where k is the Boltzmann constant, T is the absolute temperature, q is the electron charge, N_D, N_A and n_i are the donor, acceptor and intrinsic carrier concentration, respectively. The built-in voltage prevents further diffusion of electrons and holes. The net current flow across the junction is zero, as the current caused by the electric field is compensated by the current caused by the carrier gradient.

Figure 2.5 (b) shows the current-voltage (I-V) characteristic of a *p-n junction* (diode) in dark. If an external field is applied at the p and n terminals, it can act against or in favor of the built-in electric field, bringing the system out of equilibrium and causing a current flow. When the junction is forward-biased, the direction of the external field opposes the built-in field. Holes can then be injected from the p- to the n-region and electrons from the n- to the p-region. The current presents an exponential dependence on the bias (figure 2.5(b)). When the junction is reverse-biased, the external field is at the same direction with the built-in field, thus preventing majority carriers from overcoming the junction barrier, but sweeping minority carriers over the junction. As a result, there is a current flow in the reverse direction, almost independent of bias and orders of magnitude smaller than in the case of forward bias (saturation current). The current of an ideal diode in the dark is given by the formula:

$$I_d = I_0 \left(e^{\frac{qV}{nk_BT}} - 1 \right), \qquad (1)$$

where V is the voltage, I_0 is the dark saturation current and *n* is the diode ideality factor. The non-ideal behavior of the device is reflected in the values of *n* greater than 1. Non-ideality is the result of different transport mechanisms that can contribute to the diode current. For example, ideality factor of one indicates that the current is limited by the recombination of minority carriers outside the space charge region whereas ideality factor of two illustrates that the current is dominated by generation and recombination in the space charge region [17]. However, recombination through interface states at the junction, tunneling through the barriers may give rise to *n* values significantly greater than 2.

A typical solar cell structure is shown in figure 2.6, illuminated through the n-side of the junction. The n-layer is thin and of high bandgap, so that most of the photons are absorbed in the low bandgap and thicker p-layer (absorber). Short wavelength photons are absorbed close to the junction and longer wavelengths deeper in the absorber's bulk. If the electron-hole pairs are generated in the depletion region then they can be efficiently separated by the built-in electric field, enabling high carrier collection efficiency. The probability of carrier recombination is less in this case. If, on the other hand, the electron-hole pairs are generated deep into the p-side, then the charge carriers can only reach the depletion region by diffusion. The diffusion length of electrons and holes, L_e and L_h, is their mean path length: $L = \sqrt{D\,\tau}$, where D is the diffusion coefficient and τ_e, τ_h the recombination time of

electrons and holes respectively. Minority carriers with diffusion length L_e comparable to the absorber thickness can diffuse to the depletion region swept by the built-in electric field and eventually collected. Otherwise, carriers with small diffusion length cannot approach the junction within their lifetime and they recombine. The minority carrier diffusion length should be therefore longer than the thickness of the absorber to achieve efficient charge collection.

In addition to the above, the charge carriers need to be collected by the solar cell terminals with minimal energy loss. To conduct the charges to the external circuit, the contacts should be ohmic and highly selective i.e. the opposite charges carriers should not recombine during collection. Ohmic contacts to the n- and p-type regions promote efficient charge collection with low resistive losses. Higher work function materials are suitable for hole collection, while low work function contacts are suitable for electron collection.

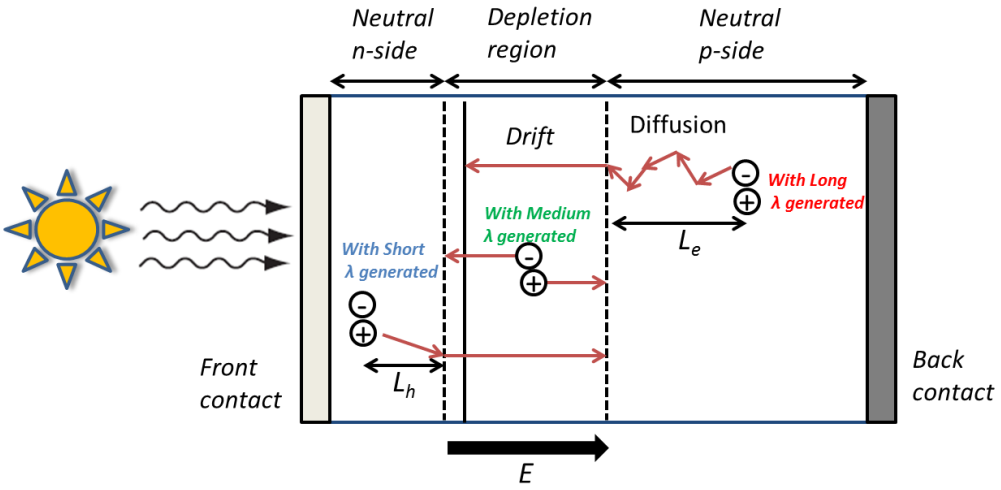

Figure 2.6: The schematic diagram of the typical solar cell consists of p-n junction

As illustrated above, a solar cell in dark is represented with a diode, whose current density is given by eq. (1). An ideal solar cell can be represented by a current source connected in parallel with a diode, as shown in the equivalent circuit diagram in figure 2.7 (a). The illuminated I-V characteristic is based on the superposition principle, which states that the photo-generated current at bias V is given by the superposition of the **photo-generated current** and the current which would flow at bias V in the dark. So, the total current through the circuit is expressed as:

$$I = I_{\mathrm{d}} - I_{\mathrm{ph}} \qquad (2)$$

By using eq. (1) in the above expression, we obtain:

$$I = I_0 \left(e^{\frac{qV}{nk_BT}} - 1 \right) - I_{\text{ph}} \qquad (3)$$

where I_{ph} is the photocurrent related to the photon flux incident on the cell. Thus from the eq. (3) one can obtain the illuminated current from the corresponding characteristic of a diode in the dark by shifting the diode characteristic along the current axis by I_{ph} in to the fourth quadrant as shown in figure 2.7 (b).

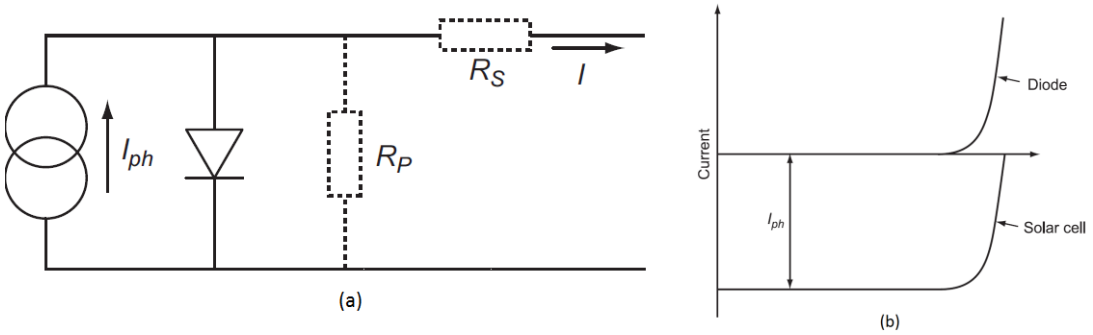

Figure 2.7 (a) The equivalent circuit diagram with parasitic resistances, (b) the superposition principle of solar cells [18]

An ideal solar cell can be simply modeled by an ideal current source and an ideal diode connected in parallel. A real solar cell device deviates from this model due to material imperfections and series resistance of the device. Therefore the equivalent circuit also includes parasitic resistances called series (R_s) and shunt (also called parallel) resistance (R_p) as shown in figure 2.7 (a), which have to be taken into account as they affect the efficiency of the solar cell by dissipating power through ohmic losses. The major contributors to the series resistance are the bulk resistance of the semiconductor and contact resistance between the contacts and the semiconductor. The shunt resistance is due to *p-n* junction non-idealities and impurities near the junction, which cause partial shunting of the junction. The equation (3) can be modified by taking into account the series and shunt resistances as follows:

$$I = I_0 \left\{ e^{\frac{q(V-IR_S)}{nkT}} - 1 \right\} + \frac{V-IR_s}{R_p} - I_{ph} \qquad (4)$$

2.1.4 Photovoltaic performance

The performance of the solar cells is evaluated by three solar cell parameters, which can be extracted from the I-V curve under illumination as shown in Figure 2.8 (a). These are the **short-circuit current (I_{sc}) or short-circuit current density (j_{sc})** i.e. $j_{sc} = I_{SC}/A$, where A is the solar cell area, **open-circuit voltage (V_{oc}),** and **fill factor (FF).** These three parameters then determine the **power conversion efficiency (η)** of a solar cell.

2.1.4.1 Short circuit current (I_{SC})

The short circuit current is produced due to the generation and collection of photo-generated charge carriers, when no external voltage is applied (V= 0). This is the maximum current one can obtain when both terminals are short-circuited, i.e. the resistance between the terminals is zero. Ideally, this current I_{SC} is equal to the photo-generated current I_{ph} of a solar cell.

2..4.2 Open circuit voltage (V_{OC})

The open circuit voltage is the voltage under illumination when the terminals are not connected (resistance is infinite), i.e there is no current flowing in the circuit (I= 0). This is the maximum voltage one can draw from the solar cell when there is no external load connected. In the ideal case, the open-circuit voltage V_{OC} is given by:

$$V_{oc} = \frac{k_B T}{q} \ln\left(1 + \frac{I_{\mathrm{ph}}}{I_0}\right) \qquad (5)$$

From eq. 5 it is clear that by lowering the saturation current I_0 of the pn junction, the open-circuit voltage is improved.

2.1.4.3 Power conversion efficiency (η)

The power obtained at I_{SC} and V_{OC} is zero, even though these are the maximum possible current and voltage obtainable from the solar cell. Figure 2.8 (b) shows the maximum power ($P_{mp} = V_{mp}I_{mp}$) that can be obtained from the solar cell where I_{mp} and V_{mp} are the current and voltage corresponding to the maximum output power P_{mp} under illumination. Therefore, the maximum power conversion efficiency for a solar cell is given by:

$$\eta = \frac{I_{mp}V_{mp}}{P_{in}} \qquad (6)$$

where P_{in} is the power of the incident light at a temperature of 25°C and an irradiance of 1000 W/m^2 in AM1.5.

2.1.4.4 Fill Factor (FF)

The fill factor is defined by the ratio of the maximum power (P_{mp}) of the cell to the product of I_{SC} and V_{OC}:

$$FF = \frac{I_{mp}V_{mp}}{I_{sc}V_{oc}} \qquad (7)$$

By inserting the relationship of eq. (7) into eq. (6), we obtain

$$\eta = \frac{I_{sc}V_{oc}FF}{P_{in}} \qquad (8)$$

In order to maximize the output power it is desirable to increase both V_{OC} and j_{SC} while the shunt resistance should be as high (lower value decreases V_{OC}) as possible and the series resistance should stay as low (higher value reduces j_{SC}) as possible. In addition, V_{OC} can be reduced due to low carrier concentration, high temperatures which increase dark current, defects and trap states (i.e. recombination), whereas I_{SC} decreases due to reflection of incident light or poor collection of photo-generated charge carriers.

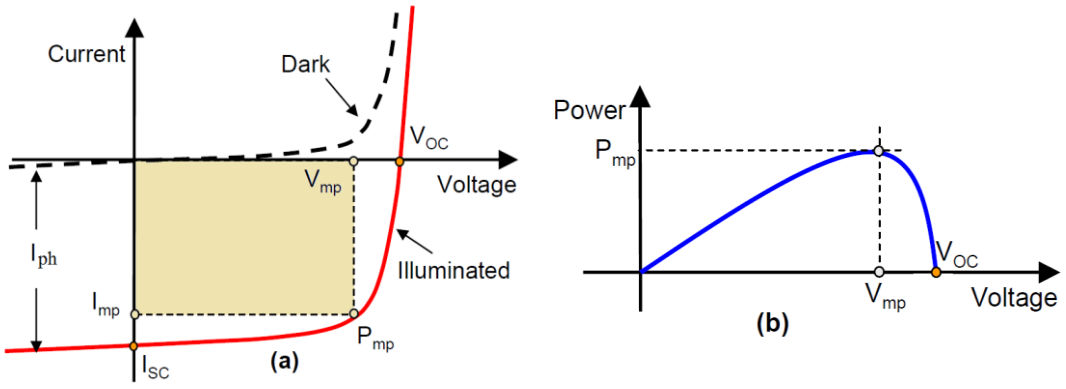

Figure 2.8. (a) Current-voltage characteristic of a solar cell under illumination with solar cell parameters, (b) the output power from the corresponding solar cell under illumination as a function of the bias voltage [19]

2.1.5 Energy band alignment

When the p and n regions of a solar cell are made from different materials, a *p-n* heterojunction is formed. In a heterojunction, the built-in voltage results from the discontinuities in the CB and VB between the two semiconductors due to the difference in the band gaps, electron affinities and ionization potentials. An important consideration in the heterojunction design is therefore the energy band lineups, as they define the carrier transport and carrier recombination.

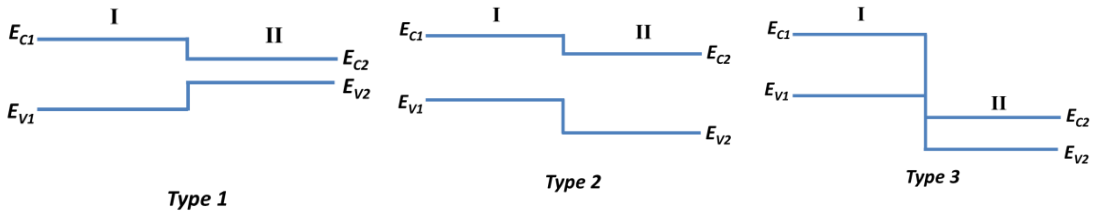

Figure 2.9: Energy band diagrams for three different types of heterojunctions

The semiconductor heterojunctions can be divided into three types, according to the energy band discontinuity, namely Type 1 (straddling gap), Type 2 (staggered gap) and Type 3 (broken gap), as shown in Figure 2.9. In type 1 heterojunction, the smaller band gap semiconductor is completely contained within the wider bandgap semiconductor. In the type 2 heterojunction, both the CB edge and VB edge of semiconductor II are situated lower than the corresponding band edges of the semiconductor I. In type 3 heterojunction, the CB level of semiconductor II lies below the VB level of semiconductor I. An appropriate band alignment at the heterojunction is essential for solar cell operation. Type 1 heterojunction limits the solar cell performance as most of the light is absorbed by semiconductor 2 (n-type) due to its smaller band-gap than semiconductor I (p-type). This type of band alignment is not ideal for perfect light absorption in p-type absorber. Type 3 heterojunction limits the solar cell performance because the band alignment promotes indirect (tunneling) recombination between electrons and holes. For efficient solar cell performance, Type 2 heterojunction is required, as it enhances the light absorption in the p-type absorber and improves the separation of photo-generated charge carriers.

The position of conduction and valence bands give rise to barriers at the interface. If the CB minimum of the n-layer is *above* that of the p-type then this results to a positive barrier (spike) and if it is *below* then it results to a negative barrier (cliff) at the interface, as shown in figure 2.10. If the *spike* or the *cliff* is large, it can degrade the photovoltaic performance of

the cell. *Minemoto et.al* [20] studied the effect of CB offset of n-type (window layer) and p-type CIGS absorber on the solar cell performance. When *spike* was formed at the interface, it acted as a barrier against photo-generated electrons, (figure 2.10(a)) which reduced the current density as well as the FF. On the other hand, when a *cliff* was formed at the interface (figure 2.10(b)) it acted as the barrier against injected electrons when the junction was forward biased, which enhanced the recombination between majority carriers via defects at the interface. The open circuit voltage and FF decreased with increased conduction band offset and the defect density at the interface. From the calculation it is suggested that the optimal solar cell performance can be obtained when the conduction band of n-layer positions higher by 0-0.4 eV than that of the absorber.

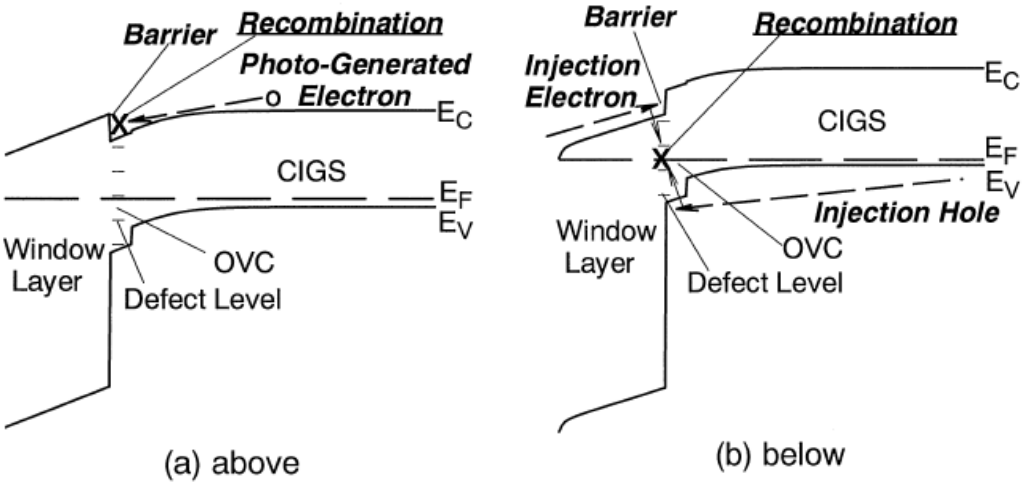

Figure 2.10: Schematics of energy band diagram of window/OVC(ordered vacancy compound)/CIGS structure when the conduction band of window layer is (a) above and (b) below that of CIGS [20]

2.1.6 Summary

In summary, for efficient photovoltaic energy conversion, efficient light absorption, charge separation, charge transport and collection are necessary. Regarding the optical absorption, the optical depth of the device should be high and the reflectivity of the surface should be small. The charge separation and transport are obtained by the intrinsic electric field originating from the p-n junction. For the charge separation, recombination should be as low as possible. The diffusion lengths (L_e, L_h) and lifetimes (τ_e, τ_h) of minority carriers should be long for efficient charge collection.

2.2 Solar cell architectures

There are two major architectures of thin film solar cells: the **substrate type** and the **superstrate type**. In the *substrate* type, the light enters the device through a **transparent contact** opposite to the substrate, as shown in figure 2.11 (a). The transparent contact is usually a transparent conductive oxide (TCO), i.e. a highly doped, wide bandgap semiconductor, such as tin-doped indium oxide (ITO) or aluminum-doped zinc oxide (AZO). Below the TCO, the n-type semiconductor is found that is often called **buffer layer**, forming the heterojunction with the p-type **absorber**. As back contact to the absorber a non-transparent metal is commonly used. In many cases, an additional intrinsic, n-type semiconductor layer with wide bandgap is deposited between the buffer and the TCO, in order to enhance the shunt resistance. This layer is called **window layer**. In the *superstrate* architecture (figure 2.11 (b)) the light enters the device through the transparent substrate (e.g. glass). So, a transparent contact is necessary between the substrate and the n-type buffer. On the other hand, at the opposite side, the contact to the absorber may not be transparent.

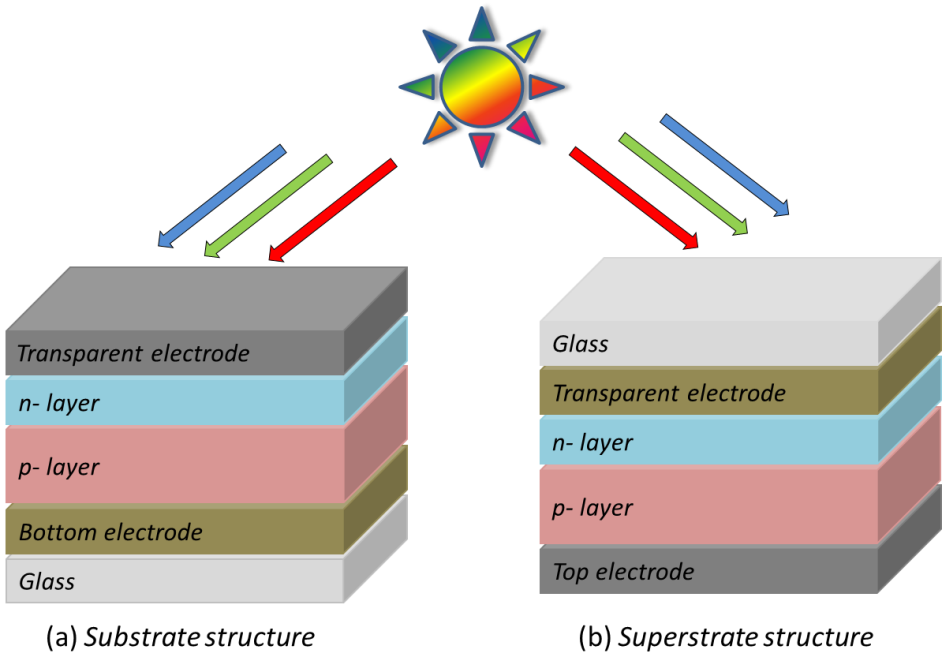

Figure 2.11: Schematics of single junction solar cell in (a) substrate structure, (b) superstrate structure.

Besides, various concepts of solar cells are employed to improve the efficiency beyond the single junction limit as predicted by *Shockley,* by maximizing the spectral response of the solar cells. These concepts include multi-junction solar cells, multi-band or intermediate band gap solar cells (IBSCs) and nano-structured solar cells. These concepts are briefly discussed in

the following sections. Other approaches employ more advanced techniques such as hot carrier, and multi-exciton generation (MEG) solar cells.

2.2.1 Multi-junction solar cells

The main idea behind the use of multi-junction cells is to increase the wavelength range of solar absorption by using multiple heterojunctions, vertically stacked, one on top of the other, in one solar cell. These heterojunctions have absorbers with progressively smaller band-gaps from top (where the light enters the cell) towards the bottom of the stack. This architecture makes it possible to increase the efficiency beyond that of a single junction cell.

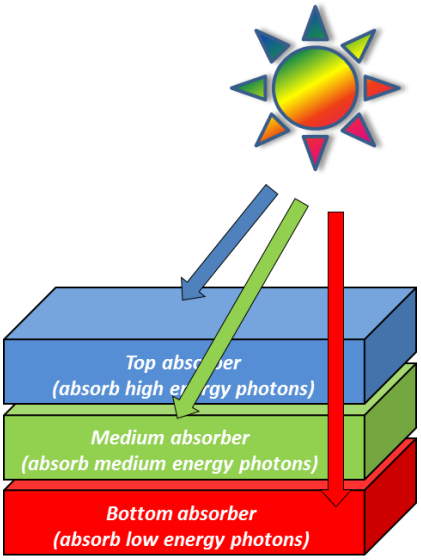

Figure 2.12: Schematic of a triple-junction solar cell structure

Figure 2.12 displays a schematic of a triple-junction solar cell. The sub-cells are combined in such a way that higher energy photons are absorbed in the top junction (highest bandgap absorber), which is, on the other hand, transparent for lower energy photons. These low energy photons are then absorbed by the medium and the bottom (smallest bandgap) absorber, respectively. Thereby, the overall heat loss due to carrier relaxation is also reduced.

Groups III and V semiconductor compounds are particularly appropriate for multi-junction solar cells, as their bandgaps span a wide spectral range, with excellent crystal quality. Double-junction (InGaP/GaAs) and triple-junction (InGaP/GaAs/InGaAs) cells under AM1.5G illumination have shown conversion efficiencies of 30.3% [21], [22] and 37.5% [23], respectively. These cells are expensive and to reduce their cost for terrestrial applications,

small area cells are combined with light concentrator optics. In this concentrated sunlight approach, a system of lenses and mirrors are used to focus sunlight on a small area of solar cells to drastically improve their efficiency. A conversion efficiency of 44 % was achieved for InGaP/GaAs/InGaAs triple junction solar cells when measured with concentrated light of 306-suns [23]. Recently, a four-junction cell of GaInP/GaAs/GaInAsP/GaInAs showed conversion efficiency of 46.1% at 312-suns [24].

Multi-junction solar cells offer high efficiency but they also have a high complexity of device design. The monolithic, stacked architecture of multi-junction cells requires current matching conditions. Indeed, as the different junctions are connected in series, the current flowing through the complete device under illumination, will be the same and determined by the sub-cell producing the smallest current. Therefore, matching the current density generated in each sub-cell is required to achieve the highest efficiency out of the multi-junction device. This is achieved by the appropriate use of materials for the cells and the layers connecting the sub-cells (tunnel junctions).

In the recent years, various other types of multi-junction cells have been investigated, including organic/organic cells [25], [26], inorganic/inorganic (amorphous and microcrystalline silicon (a-Si/µc-Si) [27] and inorganic/organic hybrid cells [28] (a-Si bottom sub-cell and organic top cell). Solar cells based on mixed hybrid halide perovskites have gained attention in recent years due to their high power conversion efficiencies [29] [30] [31]. Single-junction perovskite solar cells of methyl ammonium lead iodide $CH_3NH_3PbI_3$ have reached a conversion efficiency of 22.1% [32]. This high efficiency and bandgap of 1.57 eV of $CH_3NH_3PbI_3$ makes perovskite cells an attractive candidate as a top cell in a tandem configuration, combine with c-Si or thin film absorbers with lower bandgap (such as CIGS). To-date, silicon/perovskite tandem solar cells have reached the highest conversion efficiency of 25.5% [33]. Cu_2O is the most investigated metal oxide light absorber for PV (also used in this work). It has a relatively large band gap of ~ 2 eV and therefore potential to be used in the top sub-cell of a multi-junction device [34].

2.2.2 *Multi-band or intermediate band gap solar cells (IBSCs)*

Better utilization of the solar spectrum can be also achieved if one or more intermediate energy band(s) (IB) are inserted within the band-gap of a semiconductor absorber, as shown in figure 2.13. This approach improves the theoretical efficiency of single-gap solar cells via

the mechanism of two-step absorption of sub-bandgap photons. This concept was introduced with the impurity photovoltaic solar cell in 1960 [35]. In 1997 it gained renewed interest when *A. Luque* and *A. Marti* [36] derived that the theoretical efficiency limit for a single IB device is 63.2% (E_{VB-IB}=1.24 eV, E_{IB-CB}= 0.71 eV, E_g=1.97 eV) under maximum sun concentration (46000 suns). Then, the theory was extended to two IBs, giving a limiting conversion efficiency of 71.7% [37].

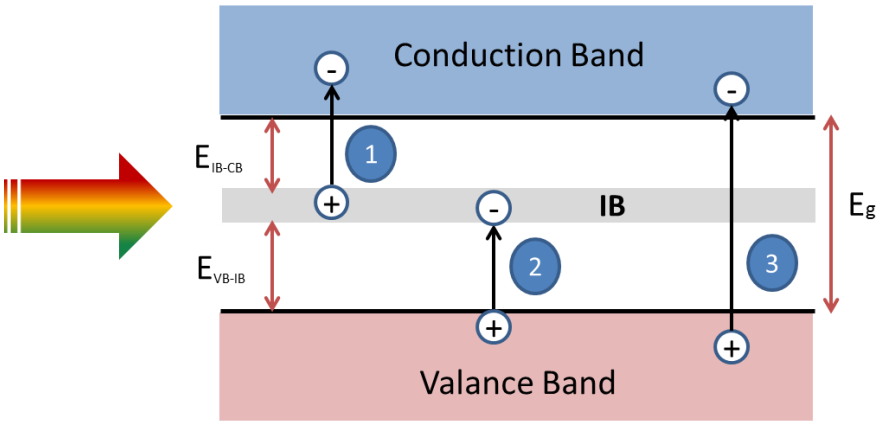

Figure 2.13: Schematic diagram showing the intermediate band (IB) concept

Luque et al. [38] calculated the limiting efficiency of a IBSC as a function of absorber band-gap under 1-sun irradiation. Maximum efficiency of 46.7% is predicted for a band-gap of 2.4 eV. ZnTe has a band-gap of 2.3 eV, i.e. close to the ideal value for IBSC. The introduction of highly electronegative elements (such as oxygen and nitrogen) in semiconductors, leads to the formation of so-called highly mismatches alloys (HMAs). The O-doped ZnTe and N-doped GaAs HMAs are the two most studied materials for thin-film IBSC application [39], [40], with showing absorption of sub-bandgap photons. *Lopez et al.* [41] characterized an IBSC of GaNAs alloys for the first time by utilizing metalorganic chemical vapor deposition (MOCVD) technique. *Tanaka et al* [42] investigated the IBSCs based on ZnTeO epitaxially grown on GaAs substrates and have demonstrated photocurrent induced by a two-photon excitation process. But unfortunately, both these device structures showed efficiency below 1%. Cu_2O (~2 eV bandgap) is also a potential candidate for IBSCs. *Malerba et al*. [43] investigated the effect of N doping (concentrations between 1 and 2.5 at %) on the optical properties of sputtered Cu_2O thin films. It was found that the doped Cu_2O samples exhibited absorption bands at energies below the fundamental optical bandgap. Therefore, it was suggested that Cu_2O could be a potential candidate as intermediate band (IB) material.

2.2.3 *Nano-structured solar cells*

In solar cells, increasing the thickness of the absorber enhances the light absorption but makes it more difficult for the photo-generated carriers to reach the device terminals, especially in absorbers with small carrier diffusion length. The nanostructured solar cell architecture (Figure 2.14 (c)) provides an opportunity to overcome this problem as it decouples the light absorption and charge carrier transport into orthogonal spatial directions [44]–[47]. The "folded junction" design allows extended absorption paths and provides short collection distances for photo-generated carriers. This improves the prospects for many candidate materials for low-cost solar cells, which often suffer from non-ideal light absorption and poor carrier transport properties. Besides, the extended junction area increases the photo-generated current, as compared to a planar junction.

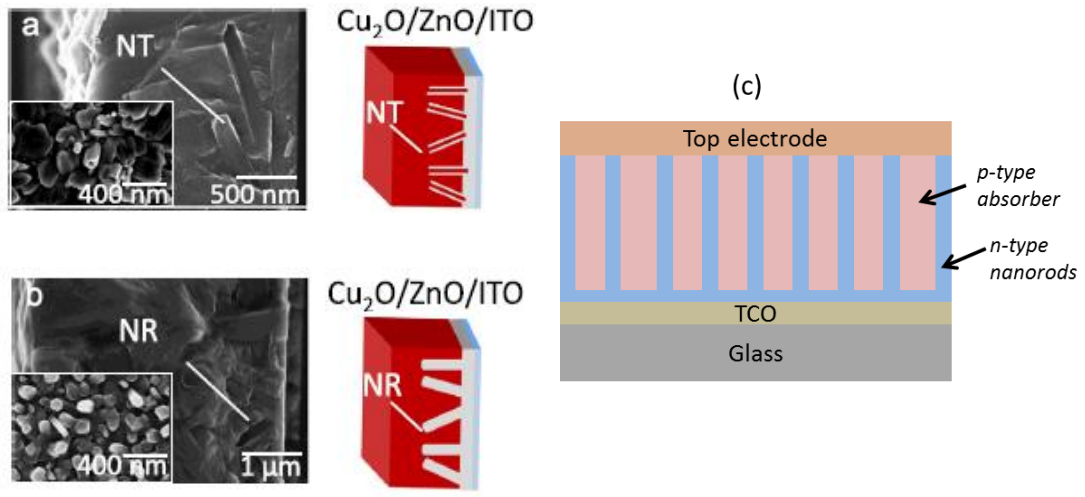

Figure 2.14: Cross-sectional HIM (helium ion microscopy) images of (a) Cu_2O/ZnO-NT and (b) Cu_2O/ZnO-NR solar cells, with insets depicting the electrodeposited ZnO nanostructures before the deposition of the 2.5-3 µm thick Cu_2O film with schematic diagrams of the Cu_2O/ZnO-NT and Cu_2O/ZnO-NR cell structures [48], (c) A typical nanostructured solar cells structure in which n-type ZnO nanorods (NRs) are embedded in the p-type Cu_2O absorber

Certain Cu_2O/ZnO-NRs cells showed very limited performance (0.1% PCE with j_{SC}, and V_{OC} of 2.35mA/cm^2 and 0.13V) [49]. This was due to the incomplete filling of the gaps between the NRs when the Cu_2O absorber was sputtered or e-beam evaporated. *Cui* and co-workers [50] showed improved power conversion efficiency when the Cu_2O was prepared using a two-step electrodeposition. The electrodeposited Cu_2O was found to completely fill the space within the NRs, forming a continuous heterojunctions. *Musselman et al.* [51] reported Cu_2O/ZnO-NR solar cells by electrodeposition. An improved j_{SC} of 5.4 mA/cm^2 was obtained

with V_{OC} of 0.21 V, FF of 32%, and power conversion efficiency of 0.36%. The low V_{OC} was attributed to the low hole mobility of the electrodeposited Cu_2O film. The authors proposed that a higher conductivity of the absorber and a better quality of the junction interface would be key factors for the performance improvement. An improved heterojunction quality and improved conversion efficiency were achieved by using ECD-Cu_2O to fill the space between sparse ZnO NRs [52]. The V_{OC} was improved to 0.514 V, with Jsc of 2.64 mA/cm^2, fill factor of 41.5%, resulting in a conversion efficiency of 0.56% [52]. More recently, higher V_{OC} values were obtained for nano-structured solar cells in which ZnO nanotubes (NTs) and nanorods (NRs) were implemented. Figure 2.14 shows SEM cross-section images of (a) Cu_2O/ZnO-NT and (b) Cu_2O/ZnO-NR solar cells. The open-circuit voltages of 0.66V for Cu_2O/ZnO-NT and 0.71 V for Cu_2O/ZnO-NR heterojunction devices were obtained. However, the low current densities in both cases, lead to limited power conversion efficiency of 0.8% and 0.4% for the Cu_2O/ZnO-NT and Cu_2O/ZnO-NR cell, respectively [48].

2.3 Properties of the Cu_2O

Cu_2O is a promising material for thin-film PV applications due to its non-toxicity and earth abundance. Copper forms two stable oxides: cuprous oxide (Cu_2O) and cupric oxide (CuO). Cu_2O crystallizes in the cuprite (simple cubic) structure as shown in Figure 2.15, in which the copper atoms are arranged in a face-centered cubic (fcc) sub-lattice and the oxygen atoms are arranged in a body-centered cubic (bcc) sub-lattice, with a lattice constant a = 4.27 Å [53]. Cu_2O has a molar mass of 143.09 g/mol, it is soluble in acid and insoluble in water, has a reddish color [54], density of 6.0 g/cm^3 with melting and boiling points of 1235°C and 1800°C, respectively.

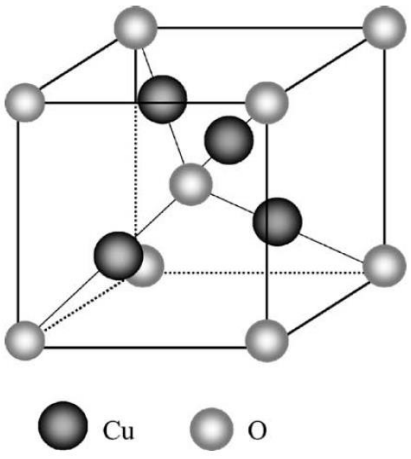

Figure 2.15: Crystal structure of Cu_2O. Black and gray circles represent copper and oxygen atoms, respectively [55]

Regarding its semiconducting properties, Cu_2O is an intrinsic p-type semiconductor, due to negatively-charged cation vacancies. The formation of copper vacancies act as a shallow hole-producer and accounts for its p-type conductivity [56], [57]. The calculated formation enthalpies of various intrinsic defects in different charge states for Cu-rich and O-rich growth conditions of Cu_2O are shown in figure 2.16. It was found that the Cu vacancy formation energy is low in all growth conditions. Furthermore, the oxygen vacancy, which is a potential hole-killer, is only stable in the neutral charge state and thus cannot annihilate holes. Other potential hole killers such as the Cu interstitials and copper antisites have high formation energies and thus have very low concentrations [57].

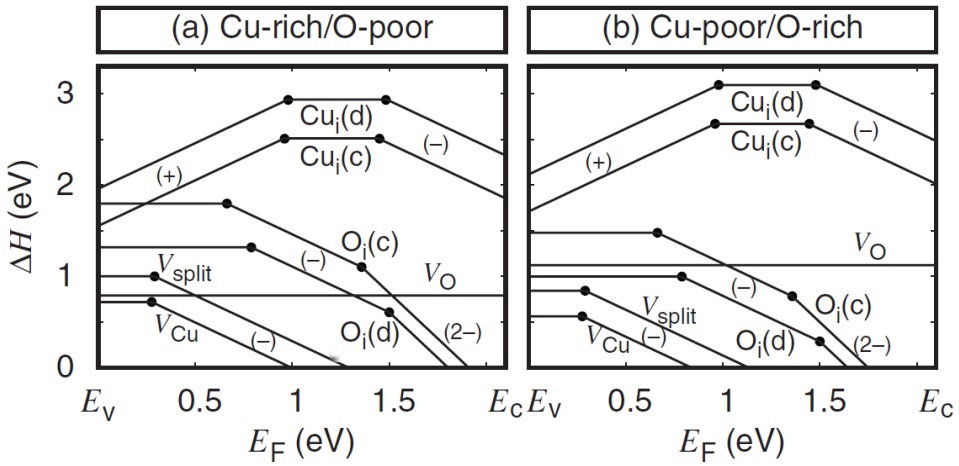

Figure 2.16: Formation energies for intrinsic defects in Cu_2O in (a) Cu-rich/O-poor conditions and (b) Cu-poor/O-rich conditions. Only lowest energy charge states are shown; ionization levels are indicated with a dot [57]

The n-type doping of Cu_2O is difficult to achieve due to the *self-compensation* mechanism [58] i.e. if a native p-type Cu_2O is doped with donors, the dopant ions are self-compensated by native ionic defects. Therefore, one does not expect to obtain an n-type Cu_2O by doping, under equilibrium conditions.

In Cu_2O, the top of the valence band states are predominately of Cu-3d character whereas the bottom of the conduction band states are of Cu-4s character [59],[60]. Cu_2O has a direct band gap of 1.9-2.1 eV [8], which translates to a theoretical energy conversion efficiency limit of ~20% for a single junction cell (Shockley-Queisser limit). Cu_2O has many other interesting properties for application in solar photovoltaics, such as high absorption coefficient of 10^3-10^5 cm^{-1} [61], high hole mobilities (~100 cm^2/Vs) [62] and minority carrier diffusion length in the range of micrometers [63]. However, the electrical properties of Cu_2O depend strongly

on the fabrication methods. Best quality layers, with grain sizes extending to the mm range, are obtained with thermal oxidation of Cu sheets at high temperatures (above 1000 °C). In the case of electrochemically-deposited thin film Cu_2O, with grain sizes in the order of 100s of nanometers, the minority carrier diffusion length is much lower, estimated as ~0.4 μm [64], whereas the hole mobilities are in the range of 4.6 and 12.8 cm^2/Vs [65].

In order to modify the concentration and mobility of majority carriers in Cu_2O, it is useful to investigate the effect that different elements have as p-type dopants. Several elements have been investigated as p-type dopants, such as chlorine (Cl), silicon (Si), nitrogen (N) and sodium (Na). *Biccari et al.* [66] studied Cl doping effects on Cu_2O films produced by thermal oxidation. The free carrier concentration measurements as a function of temperature indicated that Cl acts both as a substitutional donor and as an interstitial acceptor. Cl-doped Cu_2O illustrated conductivity about one order of magnitude greater than the undoped Cu_2O. However, solar cells fabricated from doped films showed low efficiency as the short circuit current was greatly reduced. This was attributed to enhanced recombination in the Cl-doped Cu_2O cells.

Ishizuka et al. [67] studied the effect of group-IV elements such as Si, Ge, Sn, and Pb doping on the structural and electrical properties of Cu_2O. Ge doping was found to induce electrically active acceptors with activation energy of 0.18 eV, comparable to the 0.19 eV value of Si doped Cu_2O. However, with Sn and Pb doping, the Cu_2O films became semi-insulating. It was found that Si and Ge are very useful to control the crystalline and electrical properties of Cu_2O.

Nakano et al. [68] investigated the effect of N doping into Cu_2O films deposited by reactive magnetron sputtering. The N-doped Cu_2O samples showed p-type conductivity with hole carrier concentrations of 10^{16} cm^{-3}. The optical band gap of Cu_2O was found to increase with N doping. The widening of band gap from 2.1 to 2.5 eV was observed for N doping concentrations up to 3%, with the ΔE_V and ΔE_C estimated at 0.17 and 0.23 eV, respectively.

Kikuchi et al. [69] studied the electrical and structural properties of Ni doped and un-doped Cu_2O films prepared by the pulsed laser deposition (PLD). The Cu_2O fraction was found to decrease with increasing Ni content as indicated from the XRD data analysis. The Hall measurements showed p-type conduction in Ni doped Cu_2O films.

Minami et al. [51] studied the impact of incorporating Na into polycrystalline p-type Cu_2O, prepared by thermally oxidizing Cu sheets. By incorporating Na the resistivity was controlled from 10^3 to 10^{-2} Ω cm. A high hole concentration of 10^{13}–10^{16} cm^{-3} was realized while maintaining a Hall mobility above 100 cm^2/Vs. The increased hole concentration with Na doping to charge compensation effects when Na atoms are incorporated at interstitial sites in the Cu_2O lattice. A maximum conversion efficiency of 5.53% was obtained in an n-type Ga_2O_3/p-type Cu_2O heterojunction solar cell fabricated using a Na-doped Cu_2O, having solar cell structure of AZO/Ga_2O_3/Na doped Cu_2O/Au. Cd [70], [71] was also found to be an effective p-type dopant which showed the lowest resistivity of 9 Ω cm when doped with 0.9% into bulk Cu_2O. However, the mechanism of Cd doping into the Cu_2O films is not well understood.

2.3.1 Methods of Production of Cu_2O

Cu_2O can be prepared by various methods including thermal oxidation [72], electrochemical deposition (ECD)[73], anodic oxidation [74], sputtering [75], chemical vapor deposition (CVD) [76], spray pyrolysis [77], and pulse laser deposition (PLD) [78].

Thermal oxidation is the earliest and widely used technique for Cu_2O fabrication procedure for the solar cells. This method was the adopted by *L. O. Grondahl et al., L. C. Olsen et al.* and *A. O. Musa et al*., [79]–[81] to prepare Cu_2O from Cu sheets at high temperature (750 ^{0}C - 1100 ^{0}C). This deposition method is widely used to produce high Cu_2O crystalline quality with micro-meter sized grains and low resistive layers, which are suitable for photovoltaic applications. *U. Trivich* [71] and *N. A. Economou* [82] produced good quality polycrystalline Cu_2O by this method with resistivity in the range of 10^2-10^4 Ω cm. The efficiency of 8.1%, which is the highest efficiency up-to-date for Cu_2O based solar cells, is obtained by Cu_2O films prepared by this method [9].

ECD is very simple, low cost fabrication procedure, can be performed at low temperature range to fabricate Cu_2O thin films. In 1977, *C. Noguet et al*. [83], adopted this method for Cu_2O fabrication. Cu_2O films can be electrodeposited by cathodic reduction of an alkaline solution, either on metallic substrates or on transparent conducting glass slides coated with highly conducting semiconductors [11, 24, 25]. As compared to thermal oxidation process, electrodeposited grown Cu_2O films [82] showed highly resistive thin films. Anodic oxidation is also used to produce Cu_2O film on Cu substrates. The produced film from this method has a bi-layer structure which consists of Cu_2O as an inner layer and a partly hydrated cupric oxide,

$CuO_x(OH)_{2-2x}$ as an outer layer. Corrosion studies have shown that the thickness of Cu_2O layer depends on the type of electrolyte[84], [85].

Sputtering is another method to produce thin and low resistive Cu_2O films. Reactive rf and dc magnetron sputtering from high purity Cu target was used for production of Cu_2O films. *V. F. Drobny* and *L. Pulfrey* [86], studied the electrical and optical properties of sputtered Cu_2O films. The resistivity of the films was controlled over a wide range by varying the oxygen pressure. Cu_2O films of resistivity as low as 25 Ω cm was obtained by this technique. A high quality of Cu_2O films can also be prepared by CVD method. In this process, the substrate is exposed to Cu containing precursor which is thermally decompose in the rector in the presence of oxygen to produce desired film on the substrate [87]. Several important factors such as the deposition temperature, the properties of the precursor, the substrate, and the carrier gas flow rate affect the quality of the deposited film.

There are also other methods adopted to produce Cu_2O such as spray pyrolysis [88]. In this method, Cu_2O films were prepared by spraying the precursor solution on to the hot substrate. The desired films properties can be easily tuned depending on precursor composition and hotplate temperature. PLD [80] has also been used to produce single-phase Cu_2O and CuO films on Si, MgO, Y-ZrO_2 substrates.

2.4 Properties of ZnO

ZnO, is an II-VI compound semiconductor, which crystallizes in three phases, namely wurtzite (hexagonal), zinc-blende (cubic) and rocksalt (cubic). The stable phase under ambient conditions is the wurtzite structure, belonging to the space group $P6_3mc$ where each Zn cation atom is bonded with four O anion atoms that form the corners of a tetrahedron. A schematic diagram of the ZnO wurtzite crystal structure is shown in Figure 2.17. The lattice constants range from 3.2475 to 3.2501 Å for the *a* parameter and from 5.2042 to 5.2075 Å for the *c* parameter. It has high chemical and mechanical stability, together with non-toxicity and high abundance [90].

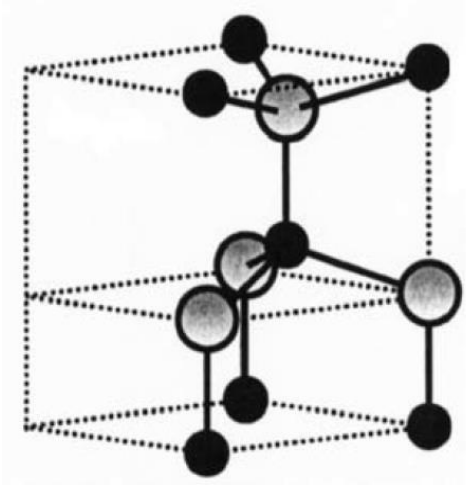

Figure 2.17: ZnO hexagonal wurtzite crystal structures. The shaded gray and black spheres denote Zn and O atoms, respectively [91]

ZnO is an intrinsic n-type semiconductor with wide direct band-gap energy of 3.2-3.45 eV at room temperature [92], [93]depending on the deposition method and growth conditions. Due to its direct band gap, large exciton binding energy (~60meV), high electron mobility (120cm^2/Vs), it is used in a wide range of electronic and optical applications such as transparent electrodes, light emitting diodes, gas sensors, field-effect transistors and solar cells [90], [94]–[96]. ZnO can be prepared by different techniques such as spray pyrolysis [97], sol-gel coatings [98], atomic layer deposition (ALD) [92], [99], pulsed laser deposition [100], magnetron-sputtering [101], chemical vapor deposition (CVD) [102], and thermal evaporation [103]. The fabrication procedure plays a significant role in controlling the properties of ZnO films.

To envisage the native n-type origin of ZnO, understanding the role of native point defects (i.e. vacancies, interstitials, and antisites) and the incorporation of impurities is essential. It was postulated that the unintentional n-type conductivity in ZnO is caused by the presence of oxygen vacancies (V_O) or zinc interstitials (Zn_i) [104]. According to density functional calculations (DFT), it has been shown that oxygen vacancies are deep donors and cannot contribute to n-type conductivity [105]–[107]. In addition, it was found that the other point defects (e.g. Zn interstitials and Zn antisites) are also unlikely causes of the observed n-type conductivity in ZnO. Instead, the n-type conductivity is related to the unintentional incorporation of impurities that act as shallow donors, such as hydrogen (H), which is present in almost all growth and processing environments. According to *Van de Walle* [108], H in interstitial site or in an oxygen vacancy acts as shallow donor and contributes to the n-type

behavior in ZnO. The concentration of the native donors depends on film deposition methods.

The electrical properties of ZnO films can be improved with intentional doping. The Group III (B, Al, Ga and In) or V (N and P) elements of the periodic table can be used as n-type and p-type dopants for ZnO, respectively. It is difficult to achieve p-type conductivity because p-type dopant such as N and P are easily compensated by native defects. The most commonly used dopants in ZnO are Al and Ga, leading to high carrier density and low resistivity, which is crucial for transparent conductive oxide (TCO) applications.

When doped with Mg and Cd, the optical band gap can be tuned either to higher or to lower values respectively as compared to un-doped ZnO, referred as band-gap engineering. The increase in band gap of ZnO by Mg doping is related to the band structure modification. Furthermore, ZnO has the wurtzite crystal structure, while MgO is cubic. If the amount of Mg incorporated into the ZnO crystal is very large, the structure is transformed from the wurtzite to the cubic one [109], [110]. According to the phase diagram, the MgO-ZnO binary system includes less than 4 at% of Mg [111]. However, the experimental solid solubility limit of MgO into ZnO by PLD is as high as 0.33 [109]. For $x < 0.33$, single phase wurtzite structure with linear increase of band gap is exhibited and for $x > 0.33$ to $x < 0.43$ a mixed state without definite increase of band gap is found. For still higher Mg doping, a cubic phase is dominant in the films [50]. The solubility limit depends on the type of fabrication method, substrate, and the temperature during deposition. The Mg doped ZnO layers were already successfully applied as buffer and window layers in chalcogenide solar cells and also in thermally oxidized Cu_2O cells. $Zn_{1-x}Mg_xO$ ($0 \leq x \leq 0.13$) films grown by metal-organic chemical vapor deposition (MOCVD) were used in combination with electrodeposited Cu_2O [112]. The power conversion efficiency of 0.71% was obtained for the $Zn_{1-x}Mg_xO$ ($x = 0.1$) based solar cell with device structure FTO/$Zn_{1-x}Mg_xO$/Cu_2O/Ag. Further, the band offset values of PLD $Zn_{1-x}Mg_xO$ with $x = 0.06, 0.21$ to electrochemically deposited Cu_2O were investigated by *Buonassisi et al.* [113].

2.5 *Schottky-junction and hetero-junction of Cu_2O*

Cu-Cu_2O Schottky junction cell was investigated by *G. P. Pollack* and *D. Trivich* in 1975 [114]. The cell was fabricated by thermal evaporation of a thin layer of Cu onto a thermally oxidized Cu_2O-absorber. A V_{OC} of 0.4V and j_{SC} of 2 mA/cm^2 was obtained for the Cu/Cu_2O schottky junction. In order to improve the V_{OC} and the conversion efficiency, *L. C. Olsen et al.* in 1979

[79], [115] studied the Schottky barrier heights formed by various metals, like Yb, Mg, and Mn, on Cu_2O, i.e. the front Cu contact was replaced by lower work function metals. Contrary to the expectation, the results showed that the barrier height did not scale with the metal work function. In-depth analysis by Auger electron spectroscopy revealed the presence of Cu at the interface. These studies clearly indicated that the surface of Cu_2O was significantly reduced to Cu during the cell fabrication with metals. The power conversion efficiencies of Cu_2O Schottky-barrier solar cells were less than 2% [79], [83] (see figure 2.18).

In the early 1980s a new preparation method for Cu/Cu_2O solar cells was introduced by *R. J. Iwanowski* and *D. Trivich* [116]. In this method, hydrogen (H^+) ions beam was used to reduce the top surface of Cu_2O to Cu to create a metal-semiconductor schottky type junction. The single-step and double-step irradiation processes have been used i.e. Cu_2O samples were exposed first to an H^+ ion beam with the fixed beam voltages between 150 V and 950 V (step I) followed by additional irradiation by low energy H^+ ions with beam voltage of 150 V (step II). The quality of Cu thin films obtained by double-step irradiation process was found to be better than that obtained by a single-step process. This resulted in an improvement in the conversion efficiency of Cu/Cu_2O schottky barrier solar cells up to $\eta \sim 1.5\%$ [117].

It was recognized that for an efficient Cu_2O-based solar cells, heterojunction or metal-insulator-semiconductor (MIS) device structures are required in order to prevent reduction of the Cu_2O surface, which was identified as the reason for low solar cell efficiencies [115]. The first report of Cu_2O heterojunction solar cells was published in 1980 by *J. Herion et al.* [118]. It concerned ZnO/Cu_2O devices, in which the ZnO layer was rf sputtered on thermally oxidized Cu_2O. An efficiency of 0.14% (V_{OC} of 0.342 V and j_{SC} of 2.29 mA/cm^2) was obtained as the Cu_2O surface was reduced to Cu at the ZnO/Cu_2O interface i.e $ZnO/Cu/Cu_2O$ and the cell characteristics were due to the schottky barrier type effect rather than photovoltaic effect of ZnO/Cu_2O heterojunction. This suggested the need to choose a low energy and low damage fabrication method to form semiconductor heterojunction with Cu_2O.

Furthermore, the band alignment of ZnO with Cu_2O is not ideal which was also responsible for the reduction of photo-voltage and thus the efficiency. To reduce the conduction band alignment as well as to improve the conversion efficiency above 1%, various n-type hetero-partners were investigated. *L. Papadimitriou et al.* [119], studied the thermally oxidized Cu_2O heterojunction solar cells with sputtered In_2O_3, SnO_2, CdO and mixtures of CdO and SnO_2 and thermally evaporated ZnSe. Among all, only the heterojunction of CdO/Cu_2O cell showed j_{SC} of 2 $mAcm^{-2}$ and V_{OC} of 0.4 V where no copper metal was found at the interface during surface analysis. *H. Tanaka et al.* [63], [120], [121] studied various TCOs thin film, such as

In_2O_3, ZnO, In_2O_3:Sn (ITO), ZnO:Al (AZO) or AZO-ITO (AZITO) multicomponent oxide, prepared by PLD on Cu_2O sheets. For AZO/Cu_2O heterojunction the efficiency was improved to 1.2% by controlling the deposition temperature during PLD to the range of 150^0C-200^0C.

Cu_2O heterojunction solar cell with efficiency above 2% was reported by *A. Mittiga et al*. [62] in 2006 (see figure 18). The device structure of Au/Cu_2O/ZnO/ITO/MgF_2 consists of a thermally oxidized Cu_2O substrate, a ZnO n-type layer, an indium doped tin oxide (ITO) window layer and an antireflection MgF_2 layer where the ZnO and ITO layers were obtained by ion beam sputtering (IBS). In 2011, *T. Minami et al.* [63], demonstrated the conversion efficiency of 3.83 %, achieved with an heterojunction made from thermally oxidized Cu_2O layer on to which undoped ZnO and AZO were deposited by PLD. They have reported V_{OC} of 0.69V, and j_{SC} of 10.1 mA/cm^2 in their devices. For the same cell structure, efficiency increased to 4.3% (see figure 18) when ZnO was doped with Mg (i.e. $Zn_{0.91}Mg_{0.09}O$) by PLD [122]. The same group demonstrated a conversion efficiency of 5.38% [123] by using Ga_2O_3 as n-type layer prepared by PLD (see figure 18). The efficiency was further increased to 6.1% (see figure 18) by using an aluminum-gallium-oxide as n-type layer and a Na-doped Cu_2O (Cu_2O:Na) sheet prepared by thermally oxidizing Cu sheets with cell structure of MgF_2/AZO/$Al_{0.025}$-$Ga_{0.975}$-O/Cu_2O:Na [124]. The highest conversion efficiency up-to-date is 8.1% [9]. It was reported for Na-doped Cu_2O prepared by thermal oxidation with zinc-germanium-oxide ($Zn_{1-x}Ge_x$-O) as n-type window layer prepared by PLD with solar cell structure of MgF_2/AZO/$Zn_{0.38}Ge_{0.62}O$/ Cu_2O:Na (see figure 18).

2.6 *Electrodeposited Cu_2O Solar cells*

In 2007, *M. Izaki et al.*[125] reported a conversion efficiency of 1.28% for ECD-grown Cu_2O/ZnO heterojunction on a conductive SnO_2-coated glass substrate (see figure 2.18). This was the highest efficiency obtained by electrodeposited Cu_2O photovoltaics devices. Recently, *Y. S. Lee et al.* [126] achieved a conversion efficiency of 2.65% for ECD-grown Cu_2O films by employing an atomic layer deposited amorphous zinc-tin-oxide (ZTO) buffer layer (at 120°C ALD-temperature). The solar cell structure is of substrate-type with Au as bottom electrode i.e. Au (200 nm)/Cu_2O (2.5µm)/ZTO (5 nm)/AZO (80 nm). By decreasing the ALD temperature from 120°C to 70°C for the n-layer, the conversion efficiency increased to 3.06% [127], due to the reduced defect density at the Cu_2O/ZTO heterojunction. The highest conversion efficiency up-to-date for ECD-grown Cu_2O solar cells is 3.97% [96]. This was achieved by incorporating an atomic layer deposited Ga_2O_3 buffer layer between the Cu_2O absorber and AZO with solar cell structure of Au (200 nm)/Cu_2O (2.5µm)/Ga_2O_3 (10 nm)/AZO

(80 nm). By using Ga_2O_3, a V_{OC} of 1.20 V was achieved due to the improved band alignment at the Cu_2O/Ga_2O_3 heterojunction (see figure 2.18). Figure 2.18 shows the summary of the thermally oxidized Cu sheets and electrochemically deposited Cu_2O-absorber solar cell efficiency obtained over the years by using different buffer layers.

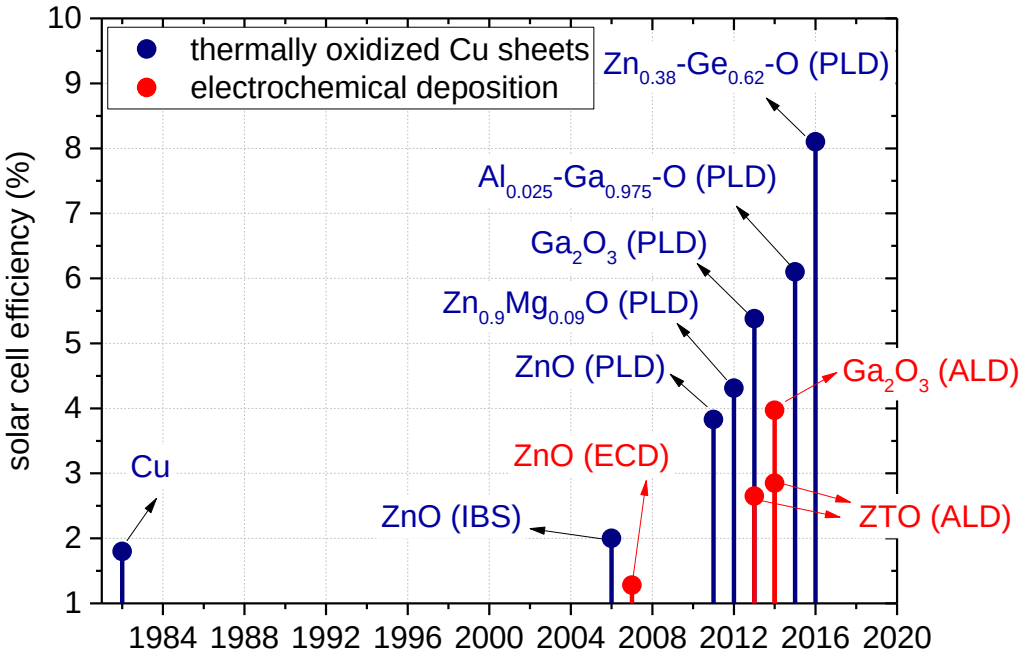

Figure 2.18: Summary of the thermally oxidized Cu sheets and electrochemically deposited Cu_2O-absorber solar cell efficiency obtained over the years where in parentheses display the fabrication method used for buffer layers

Chapter 3

Experimental Methods for film deposition and characterization

This chapter briefly describes the deposition and characterization techniques used in this thesis. For the thin-film deposition, we used sputtering for the solar cell electrodes (metals and transparent conductive oxides), electrochemical deposition for the solar cell absorber (Cu_2O) and atomic layer deposition for the buffer layer ($Zn_{1-x}Mg_xO$). The deposited thin films and solar cells were characterized structurally, chemically, optically and electrically with a range of different techniques, such as X-ray diffraction, scanning electron microscopy, ellipsometry, Fourier transform spectrometry and X-ray photoelectron spectroscopy.

3.1 Deposition techniques

3.1.1 Sputtering

Sputtering is a physical vapor thin-films deposition technique, which takes place in a vacuum chamber. During the sputter process atoms or molecules are ejected out of a solid material *target* through bombardment by energetic gas ions that comprise the so-called *plasma*. The ejected species from the target are deposited on a substrate, forming a thin film. Sputtering was first discovered in 1852 by *William Robert Grove* [128] in a gas discharge tube. Today, apart for thin film deposition, the technique is also used for surface cleaning, etching and analysis purposes.

More in detail, in the sputtering process we have an ionized inert gas (plasma) created and sustained in a vacuum chamber where the target material also resides. Typically, the plasma is composed of positively charged Ar^+ ions and electrons. The target is mounted to a *source* that is connected to a direct current (DC) or radio frequency (RF~14 MHz) electrical power supply. Upon application of a negative potential at the target (cathode), positively charged Ar^+ ions from the plasma are accelerated towards the target and bombard it, ejecting from it atoms, molecules and electrons (called *secondary* electrons). The ejected atoms and molecules from the target will diffuse and eventually deposited on a substrate. The ejected electrons accelerate away from the target, further ionizing the Ar gas, thus sustaining the plasma and the overall sputter process. The secondary electrons can be kept at the target's

proximity- thus enhancing the Ar ionization and the sputter yield-through the presence of a magnetic field. Magnetic field lines emanate from appropriately arranged magnets behind the target (figure 3.1), obliging the electrons to move in closed orbits along these lines at the target's proximity. In this case we speak about *magnetron* sputtering, allowing higher deposition rates.

To sputter conductive targets (metals and semiconductors) we can use both DC and RF power supply. For insulators, however, only RF can be used. Indeed the use of DC would lead to the build-up of positive static surface charge on the insulator, which would stop the sputtering process. This is avoided with the application of an RF power, where the target is alternatively bombarded by positive and negative plasma species, neutralizing its surface charge.

For the sputter deposition of oxides or nitrides a reactive gas-mixture is often used, composed of the inert gas and oxygen or nitrogen, respectively. This type of sputtering is called *reactive sputtering.* The reactive gas chemically reacts with the target atoms to produce the desired compound. The use of reactive gas is obviously necessary if we want to deposit a compound from a single element target. For example to deposit a ZnO film from a Zn target, it is necessary to have oxygen in the sputter gas. But also in the case where a stoichiometric compound target is used, the presence of the reactive gas can be useful for the tuning of the stoichiometry in the deposited film.

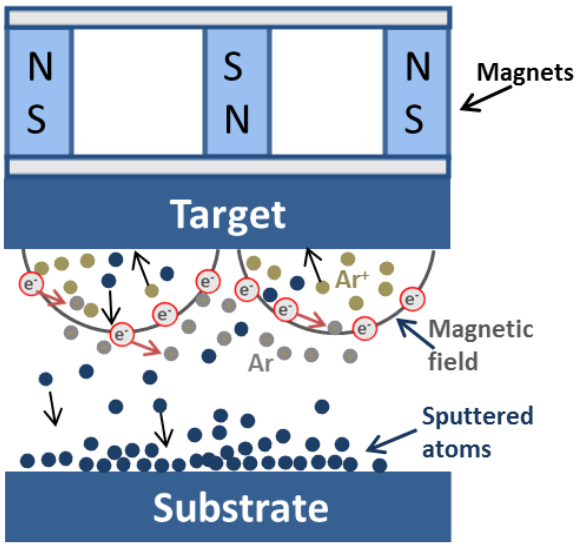

Figure 3.1: Schematic of a Magnetron sputtering process

In this work, a Leybold Univex 450C modular *sputter* system, equipped with 9 DC and 2 RF magnetron sputter sources, was used for the deposition of the Cr, ITO (Indium tin oxide: In_2O_3 doped with 10 wt% SnO_2), Ti, Au, Ag as well as for AZO (ZnO doped with 2 wt% Al_2O_3) films. All films were sputtered at DC mode with plain Ar gas. The oxide films were sputtered from stoichiometric oxide targets. The target-substrate distance was 10 cm and the substrate holder was kept at 25°C during the deposition process. Further details about the deposition parameters of the films will be given in the following chapter.

3.1.2 Electrochemical deposition (ECD)

ECD is a versatile and inexpensive, solution-based deposition technique. It is based on the *Faraday* laws of electrolysis [129] stating that the amount of material transformed at the electrodes depends on the amount of electric charge passed through the electrochemical cell. There is huge interest in utilizing this technique because of its low-cost, low-temperature deposition and up-scaling capability for large area and high throughput production.

A three-electrode ECD setup (Figure 3.2) involves the *working electrode* (WE) where net reduction takes place, the *counter electrode* (CE) where net oxidation takes place and a reference electrode (RE). The processes taking place at the WE need to be considered, whereas the CE completes the circuit and balances the charge during electrodeposition. To accurately measure the potential at the WE, the RE is used. So, in this three-electrode cell set up, the current (I) flows between WE and CE. The RE (placed at the proximity of the WE) enables one to measure the potential of the WE.

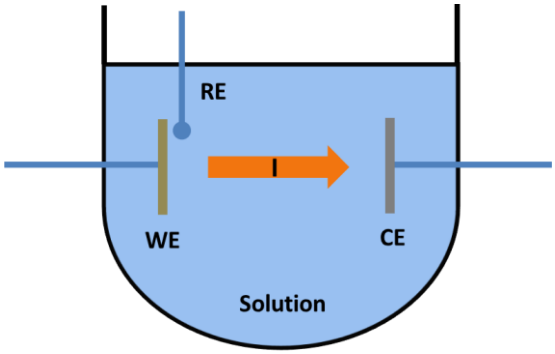

Figure 3.2: Schematic of the ECD experimental set up with three electrodes namely: substrate (WE), Ti/Pt (CE), and Ag/AgCl (RE)

When the potential of the cathode (WE) is more negative than the equilibrium potential, a cathodic or negative current will flow. On the other hand, if the potential is more positive than the equilibrium potential, then an anodic or positive current will flow. The net electrical current measured in the external circuit is due to both oxidation and reduction processes taking part in the whole electrochemical system. The factors that play a prominent role in determining ECD process are discussed below.

3.1.2.1 The electrode and electrolyte interface

The electrode/electrolyte interface is the place where electrode reactions take place and is highly important as it determines the structure and electrical properties of the deposit. At the electrode/electrolyte interface there exists a separation of positive and negative charges as shown in figure 3.3 (a), which generates an electrical double layer of thickness of 10-100 Å.

This *double layer* formation has significant contribution for the charge and potential distribution across the interface. Next to the double layer, more into the solution side, the *diffusion layer* exists in which the charge distribution is unequal, caused by the transfer of electrons at the electrode. The last region is the bulk of the solution which is far from the electrode surface where the charge neutrality is valid.

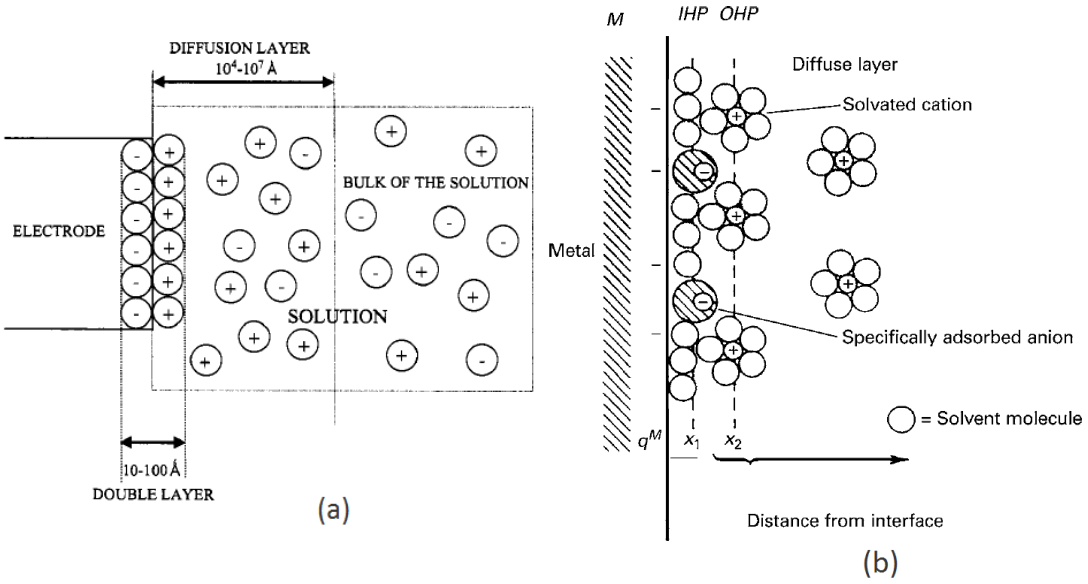

Figure 3.3: (a) illustrates the formation of three different layers according to the electrical charge distribution across the electrode and electrolyte interface [130], (b) the structure of the interfacial region as explained by Grahame [131]

The first simple structural model of the interface was envisaged by *Helmholtz*. According to him, the excess charge on the electrode is neutralized by a thin layer of ions of opposite charge. Subsequently, *Gouy and Chapman* perceived that the charges are free to move in an electrolyte solution, due to thermal motion. They suggested a diffuse layer of charges whose concentration is highest near to the electrode and decreases progressively towards a homogeneous distribution of ions within the bulk electrolyte. Later, *Stern* explained the electrode and electrolyte interface as the combination of both *Helmholtz* and *Gouy-Chapman* approaches. The currently accepted model for the structure of the interfacial region is given by *Grahame* as shown in figure 3.3 (b). The interface is split into three regions: *the inner Helmholtz plane (IHP)*, *outer Helmholtz plane (OHP)*, and *diffuse layer*. The region which is closest to the electrode is called *IHP* up to distance x_1, consists of solvent molecules or ions which form strong chemical bonds with the electrode surface (i.e. specifically adsorbed ions) and their centers define the position of the *IHP*. The next region, the *OHP,* consists of ions which interact only weakly with the electrode via electrostatic forces (i.e. non-specifically adsorbed ions) and extend up to distance x_2. The rest of the region is called the *diffuse layer* extending to the bulk electrolyte phase. The electronic properties of the electrode as well as electrolyte used are the governing factors for the interfacial structure [131],[132].

3.1.2.2 The deposition rate

The chemical reaction rate during deposition is proportional to the concentration of the reactants in the solution, as well as on the gradient of the electrical potential at the interface. The constant of proportionality between the reaction rate and reactant concentration is referred to as 'rate constant', *k,* given by:

$$k = \frac{k_B T}{h} \ln\left[-\frac{\Delta G_e}{RT}\right] \qquad (9)$$

where k_B is the Boltzman constant, *R* the gas constant, *T* the temperature, *h* the Planck constant, ΔG_e the electrochemical activation energy, which is a function of the electrode potential. The electron transfer reactions at the electrode/electrolyte interface are activated through the applied potential, as this helps to reduce the height of the activation barrier. For this, the applied potential must be greater than the equilibrium potential of the electrode (E_e). The over-potential, η, is defined as $\eta = E - E_e$. Large over-potentials increase the rate at which the electron reactions occur and therefore the current.

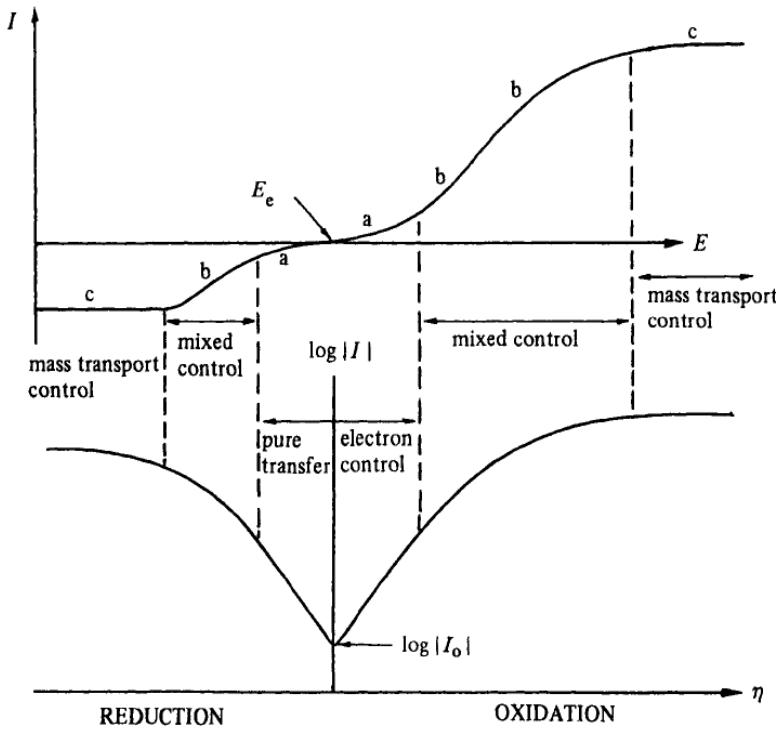

Figure 3.4: I-E and corresponding log (I-E) characteristics curves for an electrochemical cell over a wide range of over-potentials with three different regions, where a denotes: pure electron transfer control region, b denotes: mixed control region and c denotes: mass transfer control region

Figure 3.4 shows the current-potential (I-E) curve in a semi-logarithmic scale for an electrochemical cell. In the regime of low over-potential (region a) the current is determined by the rate of electron transfer to the electrode (*kinetic control*) and mass transport to the electrode has negligible effect. The chemical change at the electrode surface in this regime is small due to the low rate of deposition. The region labelled as *c*, corresponds to high over-potential values, where the electron transfer is very fast and mass transport becomes the rate-determining step (*diffusion control*). The region *b* corresponds to the intermediate situation, where there is *mixed control* of the current by the mass and electron transfer mechanisms. A large deposition rate is essential for the ECD, but at the same time, high quality, defect-poor deposits must be ensured. In order to obtain growth that is controlled by charge transfer and not by the mass-transport (which leads to defect-rich deposits) and on the other hand to obtain a high deposition rate, the potential for the deposition is usually set at the beginning of the mixed control region.

The current density-potential relationship in the kinetic regime is described by the Butler-Volmer (B-V) equation:

$$j = j_0 \left[exp\left(\frac{\alpha_A nF}{RT}\eta\right) - exp\left(-\frac{\alpha_C nF}{RT}\eta\right)\right], \qquad (10)$$

where j_0 is the *exchange current density* and α_A and α_C are known as the transfer coefficients for the anodic and cathodic reactions, respectively, *n* is the number of electrons transferred and *F* is faraday constant.

3.1.2.3 The nucleation and growth mechanism

A number of steps are involved in making a new phase on the surface of the electrode, as illustrated in figure 3.5. The ions to be reduced at the electrode surface are transported from the bulk of the solution to the diffusion layer then to the double layer region. From there, they are adsorbed on the cathode after electron transfer. The individual ad-atoms are not stable but they increase their stability by the formation of clusters through surface diffusion and then they grow as growth centers.

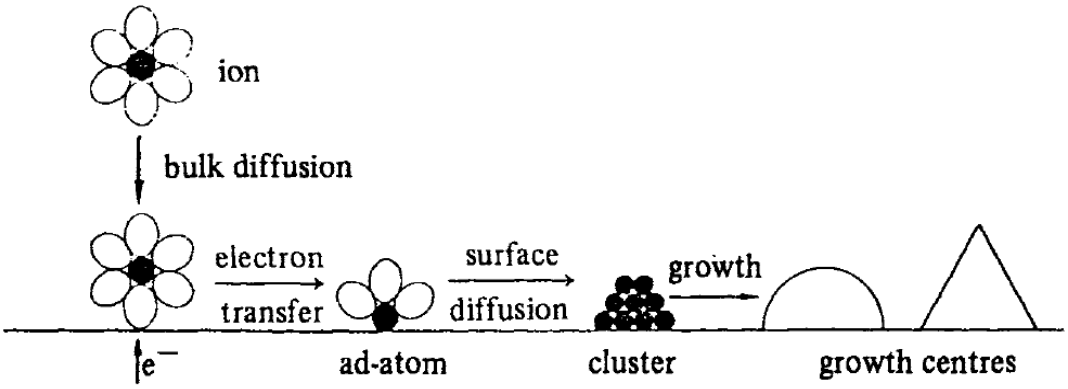

Figure 3.5: The steps involved in making a new material phase on the electrode [132]

The formation of a new material phase on the electrode requires nucleation, which occurs at the cost of over-potential i.e. we need to consider the change in free energy. We can assume that the contact between the nuclei and the electrode is small i.e. small spherical droplets are formed on an electrode. The total free energy, ΔG_{net}, as shown in figure 3.6, for a spherical nucleus on an electrode surface is given by:

$$\Delta G_{net} = \Delta G_{bulk} + \Delta G_{surf}$$

$$\Delta G_{net} = \frac{4\pi r^3 \rho nF\eta}{3M} + 4\pi r^2 \gamma$$

The first term is related to the free energy of bulk and the second term describes the free surface energy. *M* is the molecular weight of the deposit, *ρ* its density and γ the molar surface free energy. The differentiation of above equation with respect to *r* gives the expressions for the maximum in the free energy curve.

$$\Delta G_C = \frac{16\pi M^2\gamma^3}{3\rho^2 n^2 F^2 \eta^2},\ r_C = -\frac{2M\gamma}{nF\rho\eta}$$

ΔG_C is the critical free energy and r_C is the critical radius at which $(\partial \Delta G/\partial r) = 0$. Both the critical free energy and critical radius depend inversely on the over-potential, which has a great influence on the *nucleation density,* as well as on the *grain size* of the films.

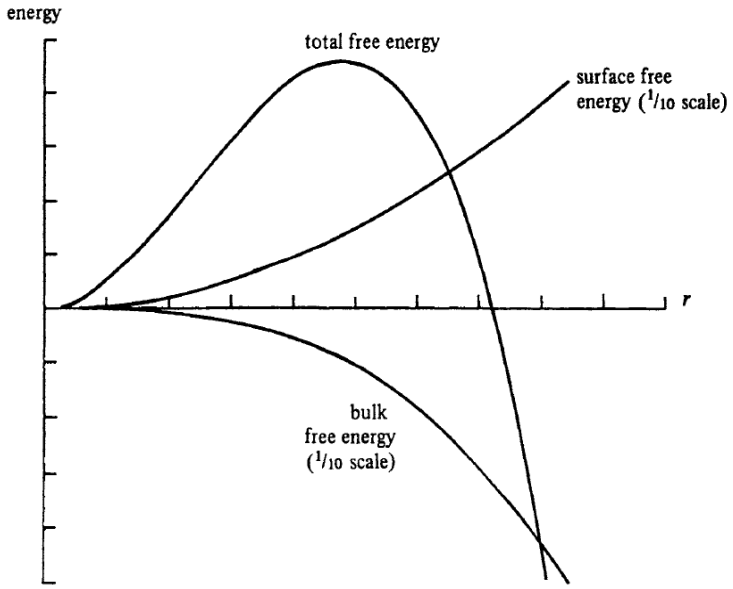

Figure 3.6: The schematic free energy curves for the homogeneous nucleation and growth of a spherical droplet [132]

This demonstrates that for a nucleus to become a stable entity, its radius must exceed r_C . Therefore, the rate constant for nucleation, A, is related to the energy barrier ΔG_C by this expression:

$$A = F\exp\left[-\frac{\Delta G_C}{k_B T}\right]$$

where *F* is a pre-exponential factor. Scharifker and Hills [133] developed models that describe the time transients of the current during electrodeposition, based on two different nucleation models, as we are going to see in the next section.

3.1.2.4 Scharifker and Hills model

Scharifker and Hills (S-H) developed a model for the potentiostatic current transients that describe the three-dimensional (3D) nucleation with diffusion controlled growth (i.e. nucleation-coalescence growth) of hemispherical islands [133]. The mathematical model is used to determine kinetic parameters, like the density of active sites on the substrate surface and the diffusion coefficient, from the experimental transient current response.

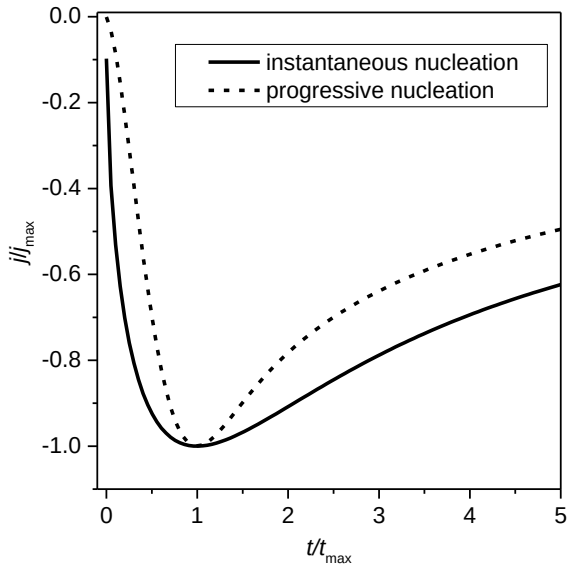

Figure 3.7: The theoretical current transients of instantaneous and progressive nucleation

According to this model [133], there are two nucleation mechanisms: instantaneous and progressive nucleation. In instantaneous nucleation the number of nuclei formed in the beginning of the deposition process does not change with the deposition time. On the contrary, in progressive nucleation the number of nuclei increases gradually with the deposition time [134]. According to the model, the current-time relationship for instantaneous nucleation is given by:

$$(j/j_{max})^2 = [1.9542\ (t/t_{max})^{-1}]\{1 - exp[-1.2564(t/t_{max})]\}^2$$

For progressive nucleation the equation reads:

$$(j/j_{max})^2 = [1.2254\ (t/t_{max})^{-1}]\{1 - exp[-2.3367(t/t_{max})^2]\}^2$$

In the above, j_{max} and t_{max} represent the current-density maximum and the corresponding time instant at which the maximum is attained, respectively. Figure 3.7 shows the theoretical current transients of instantaneous and progressive nucleation according to the S-H model.

In this work, the Cu_2O absorber was electrodeposited using an AUTOLAB potentiostat/ galvanostat. The solution was heated on a hot plate to the temperature of 50°C prior to the deposition. The temperature remained constant at this value during the deposition. For the ECD of Cu_2O, the glass substrate, coated with the conductive film, was immersed vertically in the reservoir and connected to the working electrode (WE) of the potentiostat. The Cu_2O deposition was performed without stirring under potentiostatic mode (potential fixed during deposition). A platinized titanium mesh was used as the counter electrode (CE). The applied deposition potentials were referenced to an Ag/AgCl reference electrode (RE).

3.1.3 Atomic layer deposition (ALD)

ALD, originally called atomic layer epitaxy [135], is a chemical vapor phase fabrication method for thin films, invented by Tuomo Suntola in the 1970s [136]. The very first commercial application of ALD was the growth of polycrystalline ZnS thin films for electroluminescent (EL) display panels in 1980s [137]. In ALD, the growth mechanism is based on self-limiting, surface-controlled chemical reactions.

The main advantages of ALD are: self-limiting surface reactions, possibility of thickness control down to monolayer level, excellent uniformity, low temperature deposition, easy scale-up. It is one of the best-suited deposition techniques for homogenous pin-hole-free thin-films. The ALD method is most popular for growing composites, especially oxide and nitride films. The films grown by ALD are popular for microelectronic applications where extremely thin films are required, with their composition and uniformity controlled at an atomic level.

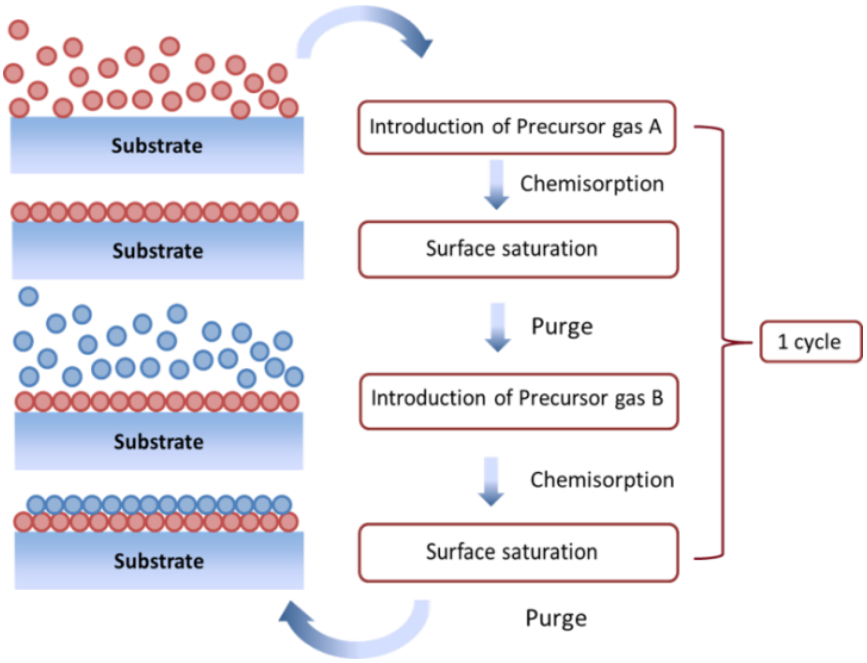

Figure 3.8: Schematic of the ALD deposition procedure for two precursor gases

The operation principle relies on the chemical reaction between the precursors (in vapor phase) and the heated-substrate surface, while the reaction byproducts are pumped out of the reaction chamber regularly. When the precursor pulses are introduced into the reaction chamber, after every pulse the reaction chamber is purged with an inert gas. Through this process, the precursors can only react with the substrate's surface but not with one another in the gas phase.

Figure 3.8 illustrates the ALD procedure for two precursor gases namely A and B. The first step involves the introduction of precursor gas A into the reaction chamber where it reacts with the heated substrate surface. It chemisorbs on the substrate surface and soon the surface saturation occurs, i.e. all available surface sites are used for reaction with the precursor. When this is achieved, the reaction chamber is purged with inert gas. Then, the second precursor gas B is introduced in the reaction chamber, which reacts with the first layer and the surface saturates forming a monolayer of material. The reaction by-products are pumped out of the chamber during the following purging step with nitrogen. This alternating pulsing of precursors to form a monolayer of material on the surface constitutes one ALD cycle. The sequence can be repeated for as many ALD cycles are necessary to obtain the required film thickness.

3.1.3.1 Growth rate

After one cycle, certain amount of material is deposited on the substrate surface, defining the "growth per cycle" (GPC). GPC values increase with increasing number of reactive surface sites. The growth rate of the deposition strongly depends on the deposition temperature as it affects the number of reactive sites present on the surface [138]. Each ALD process has a temperature window, which depends on the reactivity and stability of the precursors. The temperature range where the growth is self-limiting defines the "ALD temperature window". Outside this temperature window the growth rate can change dramatically. For instance, at very low temperatures, condensation of the precursors can result in a rapid increase of GPC, or, it can also result in low GPC values if the surface reactions are incomplete. On the other hand, at very high temperature, precursor can either decompose, which leads to an increase in the growth rate or desorb, which thereby reduces the growth rate. Hence, it is desirable to deposit within the ALD temperature window.

3.1.3.2 Precursors

The main types of precursors used in ALD are organometallic complexes -the metal alkyls. There are various factors to take into account when selecting these precursors: they should be volatile at the deposition temperature, highly reactive, and thermally stable at the substrate temperature in order to avoid self-decomposition. This means a strong and complete reaction between them and the substrate surface must be achieved. Also, the by-products of the surface reaction must be non-reactive so that they can easily be swept out of the reaction chamber.

In this work, ZnO and Mg-doped ZnO layers were deposited using a Cambridge Nanotech, Savannah 100 ALD reactor. Diethylzinc (DEZn), bis-(ethylcyclopenta-dienyl)- magnesium ($(CpEt)_2Mg$), deionized water (H_2O) and nitrogen (N_2) were used as Zn metal precursor, Mg precursor, oxidant and purging gas, respectively. The base pressure of the ALD chamber during growth was kept at 1 mbar by using an Alcatel Adixen Pascal 2005 l rotary pump. The precursors were alternately pulsed at substrate temperature of 150°C. The H_2O and DEZn precursors were at room temperature, while $(CpEt)_2Mg$ was heated to 85°C. The purging time of 30 s was used for all deposition cycles.

3.2 Characterization techniques

3.2.1 Spectroscopic Ellipsometry (SE)

Spectroscopic ellipsometry (SE) works on the principle that the polarized incident light on a sample undergoes some change in polarization state as it reflects from the sample's surface. The reflected light is used to extract film properties such as the complex refractive index, surface roughness, and layer thickness.

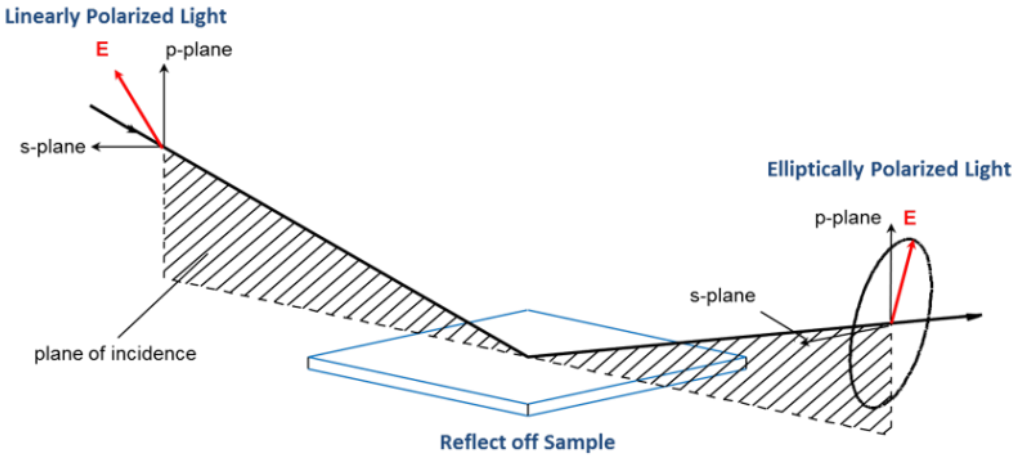

Figure 3.9: Schematic of interaction of polarized light with a sample [139]

Let incident light obliquely reflected from the sample as shown in Figure 3.9. The light with its electric field vector oscillating in the plane of incidence is called *p*-polarized, whereas when oscillating perpendicular to the plane of incidence *s*-polarized. The reflection for the *p* and *s* polarized light from the sample is described by the complex Fresnel reflection coefficients r_p and r_s respectively. As shown in figure 3.9, the incident light is *linearly* polarized with polarization states *s* and *p.* After reflection it becomes *elliptically* polarized. The change in polarization state is characterized by the two ellipsometric parameters ψ and Δ and is given by the complex ratio ρ of the two reflection coefficients as:

$$\rho = \frac{r^p}{r^s} = \tan\psi e^{i\Delta} \qquad (11)$$

In ellipsometry, ψ and Δ values are acquired as a function of wavelength. However, in order to extract sample parameters such as film thickness and optical constants from the measured data set, an optical model is used to fit the data. In the optical model, the complex index of refraction is calculated as a function of wavelength, which is used to estimate the film

thickness. For a three phase optical system (i.e. an ambient-film-substrate structure), if $r_{12}^{p}$and r_{12}^{s} are the parallel and perpendicular reflection coefficients for light incident at medium (air) and film boundary and r_{23}^{p} and $r_{23}^{s}$are the reflection coefficients at the boundary between the film and substrate then the total reflection coefficients $R^{p}$and R^{s} are given by:

$$R^{p} = \frac{r_{12}^{p} + r_{23}^{p} \exp X}{1 + r_{12}^{p} r_{23}^{p} \exp X} \qquad (12)$$

$$R^{s} = \frac{r_{12}^{s} + r_{23}^{s} \exp X}{1 + r_{12}^{s} r_{23}^{s} \exp X} \qquad (13)$$

X is the quantity related to thickness of the film as $X=-4\pi j n_2 \cos\Theta_2 d_2/\lambda$, where d_2 and n_2 are the thickness and refractive index of the film, $\cos\Theta_2$ is given by Snell's law and $j=\sqrt{-1}$. The ratio of the parallel and normal total reflection coefficients is defined as ρ i.e.

$$\rho = R^{p}/R^{s} \qquad (14)$$

Substituting eqs (12), (13), and (14) in eq (11) and rearranging gives a quadratic equation of the form:

$$Y_1(\exp X)^2 + Y_2(\exp X) + Y_3 = 0 \qquad (15)$$

where Y_1, Y_2 , and Y_3 are complex functions of the refractive indexes, angles of incidence, ψ and Δ. For the transparent films, the Cauchy dispersion function is usually used for modeling the optical constants and estimating the film thicknesses. The refractive index of the transparent film in the visible spectral range is given by the Cauchy dispersion relation as:

$$n(\lambda) = A + \frac{B}{\lambda^2} + \frac{C}{\lambda^4} \qquad (16)$$

where A is the amplitude of the material index and B and C are parameters providing the shape and curvature of the index as a function of wavelength. The best fit of the model with the experimental data gives the optical constants of the film, which are then used to calculate the film thickness by solving equation (15). In this work, we have used the spectroscopic ellipsometer alpha-SE (J.A.WollamCo.) to calculate the thickness of the ALD grown ZnMgO layer, implementing the Cauchy dispersion relation described above.

3.2.2 X-ray diffraction (XRD)

XRD is a non-destructive analytical technique for determining the structural properties of the materials. In 1912, *Von Laue* discovered [140] the phenomenon called *diffraction* of X-rays by crystals and *William Lawrence Bragg* who analyzed the first crystal structure using X-rays. The use of X-rays for the analysis of atomic structural arrangements relies on the fact that X-rays undergo *diffraction* when interacting with periodic systems with periods of the same order as the X-ray wavelength. The interatomic spacing of atoms in a crystal lattice is of the same order as the X-ray wavelength (Å), which makes crystals to act as diffraction grating for X-rays. The diffraction pattern reveals the crystal structure.

Figure 3.10 (a) illustrates the geometrical conditions for X-ray diffraction. *Bragg* determined the rule governing the diffraction pattern relating the spacing d_{hkl} between atomic planes in a crystal to the angle at which x-rays are scattered when they strike the crystal.

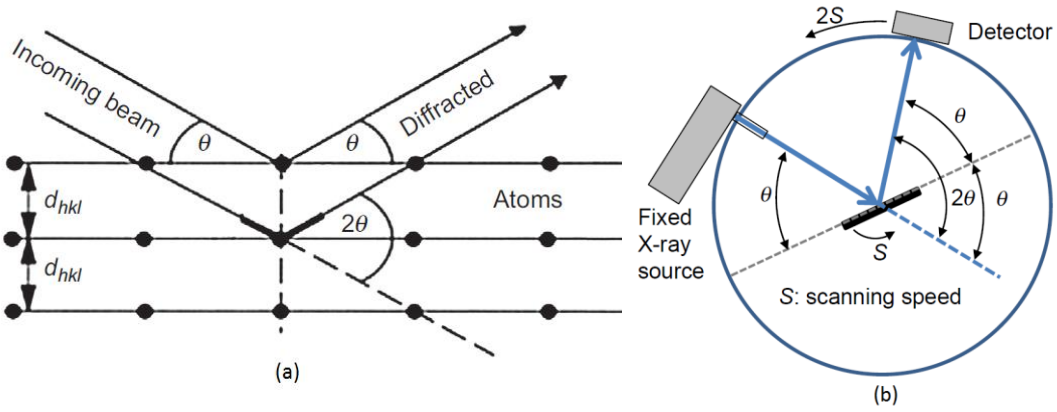

Figure 3.10: (a) Geometrical condition for diffraction from lattice planes [138], (b) Bragg-Brentano (θ-2θ) geometry [138]

Constructive X-ray interference is observed when Bragg's Law is satisfied:

$$n\lambda = 2d_{hkl}sin\theta$$

where *n* is the order of diffraction, d_{hkl} is the spacing between crystal planes, θ the angle of incidence and λ the wavelength of the X-ray beam. By changing the angle, Bragg's Law conditions are satisfied for different *d*-spacing (i.e different atomic planes) in the crystal. Plotting the angle versus the intensity of the resulting diffraction peaks of radiation produces a pattern, which is characteristic of the sample crystal structure. Information regarding the unit cell dimensions can be obtained from the diffraction peak positions which further used

to evaluate if there is any distortion within the crystal lattice. This is because any change in the crystal lattice due to substitutional doping or stress will change the *d*-spacing. In the case of homogeneous strained material, the change in d_{hkl} shifts the diffraction peaks. By measuring this shift, the strain in the crystal lattice can be evaluated. For instance, if a peak position shifts to higher angle (i.e. smaller *d*-spacing values than equilibrium) this indicates that the lattice parameter is compressed in this direction. Furthermore, the crystallite size can be evaluated from the full width at half maximum (FWHM) of the peak, B, by assuming that the crystal has uniform size and instrumental peak broadening is larger than the crystal size broadening. For this, we use the Scherrer equation:

$$B = K\lambda/L\ cos\theta$$

where L is the crystal size, K is the Scherrer constant (mostly K=0.94). As the crystallite size gets smaller, the peak broadens. In XRD, the diffractometer is equipped with a goniometer, which allows moving the X-ray source, the sample and the detector relative to each other in a very precise manner. Bragg-Brentano geometry is widely used for the XRD, in which the distance between the sample and the detector is constant for all angles. In this work the XRD investigation of the materials was done using an X'PERT (PRO) POWDER diffractometer in the Bragg-Brentano (θ-2θ) geometry (see Figure 3.10 (b)), equipped with Cu Kα X-Ray source. The diffractograms were analysed by the software X'Pert Highscore Plus.

3.2.3 Scanning electron microscopy (SEM)

Scanning electron microscope (SEM) is a tool for surface imaging at the nanoscale. This method utilizes a focused beam of electrons to scan the specimen. The high-resolution images provide topographical, morphological and compositional information of the specimen scanned. The schematic diagram of a SEM is shown in figure 3.11 (a). An electron gun is used to produce high energy electron beam, which passes through a system of magnetic lenses (condenser lens and objective lens), enabling the adjustment of the beam diameter that falls on the specimen. The interactions between the incident electrons and the specimen's surface cause the electrons to be emitted from the specimen either by elastic or by inelastic scattering. Figure 3.11 (b) shows the most important interaction processes and the range of interaction. A number of signals are produced, including backscattered electrons (BSEs), secondary electrons (SEs), the emission of characteristic X-rays, Auger electrons. The two main signals utilized in the SEM are SEs and BSEs, which predominantly provide information about surface topography and sample composition, respectively.

The electrons which are scattered by an elastic collision of an incident electron, such as reflected electrons or the electrons deep from the specimen are referred to as BSEs. The BSEs are high energy electrons (> 50 eV) due to the negligible energy loss during the collision. On the other hand, the emitted electrons resulting from inelastic scattering are called SEs. These are the emitted valence electrons from the specimen atoms, from a relatively small escape depth close to the sample surface. This means that the secondary electrons are very sensitive to the surface and provide information about surface topography.

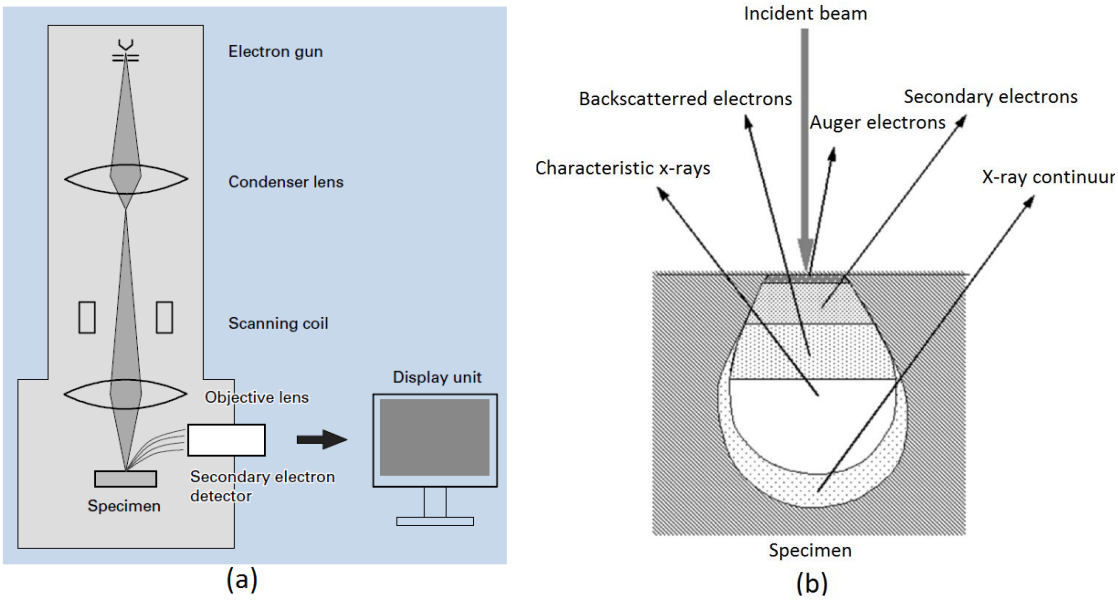

Figure 3.11: (a) Schematic diagram of a scanning electron microscope (SEM), (b) shows the signals generated by the electron-specimen interactions and the regions from which the signals can be detected [141].

The low energy secondary electrons (less than 50 eV) can be collected by a positively charged detector. For this, in a standard SE detector a high voltage (+10 kV) is applied to attract and accelerate these electrons to sufficiently high energies to create a light pulse after hitting a scintillator (fluorescent material). The light pulse is then amplified by a photomultiplier. This SE detector provides efficient surface images but requires large working distance for effective collection of the SEs. In addition, the topographical contrast in the SEM is dependent on how many of the secondary electrons reach the detector. The electrons which cannot reach the detector generate shadows or darker contrast than those regions where there is no obstacle for the electron path to the detector. To overcome this problem, another SE detector is used, called the in-lens detector, in which the positively biased detector is placed above the objective lens where secondary electrons are accelerated towards this

detector by utilizing the lens magnetic fields. Moreover, the SE image from the in-lens detector shows no shadowing effects, which results in high contrast, high signal-to noise images that are optimum for high-resolution imaging even at low voltages and small working distances. In this work, surface and cross section images of the layers are obtained by scanning electron Microscopy (SEM, Zeiss SUPRA 40) using an in-lens detector and 5 kV beam acceleration voltage.

3.2.4 Fourier transform infrared (FTIR) spectrometer

The Fourier transform infrared spectrometer is an instrument used for optical analysis of the sample, i.e measuring transmittance and reflectance spectra. The main components of spectrometer are the light source, beam splitter, mirrors and a detector. The beam splitter and the mirrors are arranged in the form of a Michelson interferometer as shown in figure 3.12 (a), which is the core of FTIR spectrometer. In this method, the source generates radiation which passes the sample through the *interferometer* and reaches the detector. The detector then measures the intensity of light as a function of the optical path difference (also called retardation). The signal obtained from the detector is an interferogram, which yields the spectrum by Fourier transform.

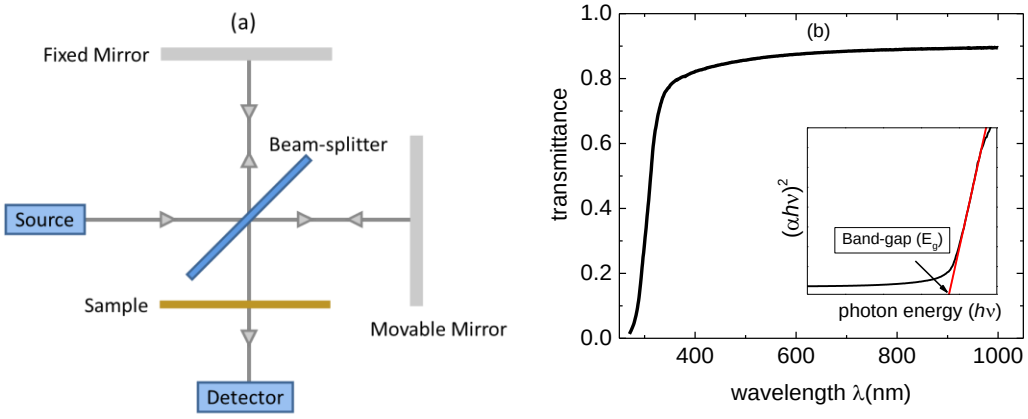

Figure 3.12: (a) Schematic diagram of FTIR, (b) shows the extraction of optical bandgap of the direct band gap material by using Tauc plot

The most common method for determination of band gap of a material is by optical absorption analysis. As already discussed in chapter 2, experimentally, the absorption coefficient, α, can be obtained by using the Lambert-Beer absorption formula i.e. $I(t) = I(0)exp^{-\alpha t}$ where I is the transmitted light, I(0) is the incident light intensity, t is the thickness of as-deposited film and α is the absorption coefficient. From this equation α can

be obtained as: $\alpha = \frac{1}{t} ln\left(\frac{1}{T}\right)$ where $T = I/I_0$. The absorption edge can be extracted from the transmittance data by using Tauc relation [142], which is given as follows:

$$(\alpha hv)^n = A\,(hv - E_g) \qquad (17)$$

where *h* and *v* are the Planck's constant and photon frequency, respectively. *A* is a constant and *n* depends on the nature of the band-gap (*n* = 1/3 for indirect forbidden transition, *n* = 1/2 for indirect allowed transition, *n* = 2/3 for direct forbidden transition and *n* = 2 for direct allowed transition). Figure 3.12 (b) shows an example of optical band gap determination for the direct band gap semiconductor (n = 2). The optical transmittance, T (λ), of the film is obtained by FTIR in the range of 250-1000 nm as shown in Figure 3.12 (b). Then, by plotting Tauc plots i.e. $(\alpha hv)^2$ versus photon energy (*hv*) plot, the band gap is evaluated by extrapolating the linear part of the curve with the photon energy axis i.e. $(\alpha hv)^2 = 0$ according to the eq. 17.

In this work, the samples are optically characterized using a Bruker Vertex 70 FTIR system, additionally equipped with a visible light source. The direct transmittance is measured for normal incident light and referenced to the sample holder without sample. The specular reflection is measured with the A513QA accessory of the spectrometer, at 13° angle of incidence. The measured signal is referenced to a calibrated mirror (aluminum, coated with dielectric) in the range from 330 nm to 550 nm and to a thick, 150 nm Au-coated substrate, in the range from 550 nm to 1100 nm. The total (direct plus diffuse) reflectance is measured with a teflon (PTFE) integration sphere accessory for the Vertex 70. A GaP and a Si detector are used to record spectra in the range of 330–550 nm and 550–1100 nm, respectively.

3.2.5 X-ray photon spectroscopy (XPS)

XPS is a widely used surface analysis technique, capable of providing chemical and electronic characteristics information of the material. In the mid-1960s, a high resolution spectrometer was developed by Swedish physicist *Kai Siegbahn* and co-workers at Uppsala University [143] which can determine precisely the binding energy (BE) of core electrons. The binding energy is the energy required to remove an electron from the electronic shell, and is the basis of XPS analysis. In XPS, ejected electrons via electromagnetic radiation are measured and used to investigate quantitatively the elemental composition and chemical environment of the studied sample. In addition, XPS is very useful technique to study interfacial properties such as band offset values at a heterojunction, since it is a powerful tool for measuring the valence band energy.

Photo-ionization process: XPS is based on the photoelectric effect to investigate the binding energy (E_B) of the electrons in the sample. X-rays are used to excite the sample with photon energies *hv* ranging from 100 eV to 10,000 eV, as shown in figure 3.13 (a). If the energy is high enough, some of the core level electrons absorb this energy, overcome their binding energy E_B and are emitted out of the surface with a certain kinetic energy E_{Kin}. This process is described by the Einstein equation:

$$hv = E_B + E_{Kin} + \varphi \qquad (18)$$

where ϕ is the work function of spectrometer. This is included in the measurement by assuming that the sample is in electrical contact with the spectrometer so that the sample and spectrometer both have common reference for measuring the electron energy [144] [145]. The ejected electrons are collected and their kinetic energy E_{Kin} analyzed. Then, the binding energy E_B of the core level electron can be determined from the above equation.

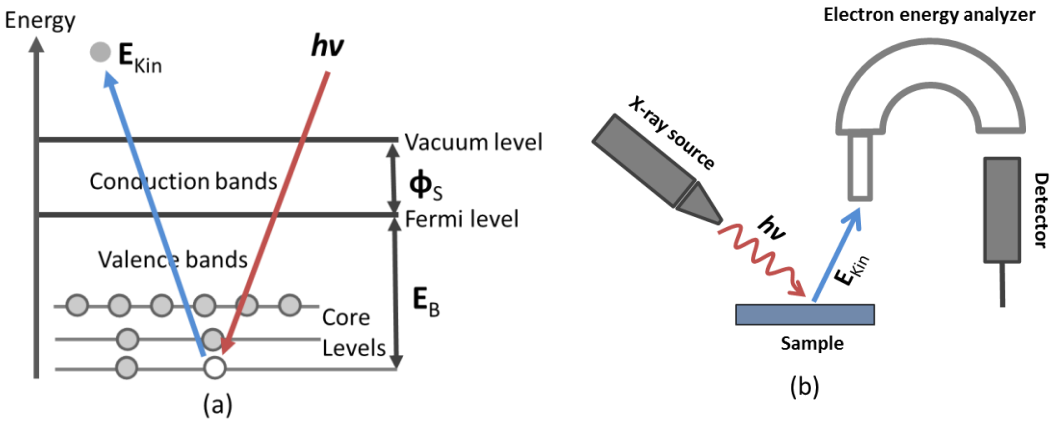

Figure 3.13: (a) Schematic diagram of a core-level-photoelectron emission process, (b) schematic diagram of the experimental setup for XPS experiments

The number of emitted photoelectrons is measured as a function of the kinetic energy and the energy spectrum is obtained. This energy spectrum of the photo-excited electrons yields the profile of electronic density of states of the element from which they are ejected. The spectrum contains photoelectron peaks corresponding to the atomic core levels of the element. Based on the analysis of a peak at a particular energy in the XPS spectrum, quantitative and qualitative information on the elements present in the sample can be obtained.

The main components of an XPS tool are the X-ray source, a hemispherical electron energy analyzer to record the spectra of the photo-emitted electrons and detector as shown in

figure 3.13 (b). Mg Kα (*hv* = 1253.6 eV, fwhm = 0.70 eV) and Al Kα (*hv* = 1486.6 eV, fwhm = 0.85 eV) are widely used X-ray sources in XPS because of their high photon energy, which helps to excite a wide range of elements and allows narrow natural line widths that allows to differentiate between multiple oxidation states. Furthermore, to identify various elements, the energy resolution of electron analyzer must be sufficiently high so that the peaks from different chemical oxidation states can be de-convoluted. In order to measure the electron energy, electrons should reach the detector. However, not all the photo-excited electrons reach the detector because a photoelectron can only travel a certain distance inside the solid before escaping to the vacuum. Inelastically scattered electrons will form a spectrum background or will not escape from the solid. Only the electrons near to the top surface of the specimen can escape without kinetic energy loss. The probability that the photoelectrons escape from the solid without loss of energy is determined by the inelastic mean free path (IMFP). IMFP is the average distance that a photoelectron can travel between inelastic collisions. The larger the kinetic energy, the longer will be the IMFP.

3.2.5.1 XPS measurements and data analysis

In this work, XPS measurements were performed in an ultra-high vacuum chamber, using a Phoibos 150 MCD-9 detector Specs with Al Kα as X-ray source. All the XPS measurements were performed by first taking a survey scan spectrum covering a range of 1000 eV, and then high resolution scans were performed on the selected individual peaks. These high resolution scans were used for quantitative data analysis. The binding energy scale of the spectrum is calibrated by the carbon C1s peak to insure accurate binding energy measurements.

3.2.5.2 Chemical Composition

The XPS spectrum contains peaks originating from various elements present on the surface of the specimen. The area under these peaks is related to the amount of each element. The quantitative concentrations of elements are calculated using the *relative sensitivity factors* and the *peak areas intensities*. The measured intensity of a photoelectron of a given element, I, is expressed as: $I = n.R$, where *n* is the atomic concentration of the element and *R* is the relative intensity factor used for the composition determination. R includes the following terms: the photo-ionization cross-section for the atomic orbital of interest (function of photoelectron transition) σ, the IMFP of the photoelectrons in the sample λ, the angular efficiency factor for the instrumental arrangement θ, x-ray flux f, the area of the sample from which photoelectrons are detected A, the analyzer transmission function T and the detection efficiency for electrons emitted from the sample D, i.e. $R = f\sigma\theta\lambda ADT$. The

concentration *C* of an element *x* is given by dividing the element intensity *I* with *R* and normalized all over the elements detected (I_{all}):

$$C_x = n_x/n_{all} = \frac{I_x/R_x}{I_{all}/R_{all}} \qquad (19)$$

Band offset values: The *band offset* values (conduction band offset and valence band offset values) at the Cu_2O and $Zn_{1-x}Mg_xO$ heterojunction are also evaluated by XPS. For this the method proposed by *Kraut et al.*[146] is followed: the electronic densities of states vanish at the valence band edge but the electron spectrometer produces a tail, which extends to some eV, obscuring the exact position of valence band edge. The VBM position is evaluated by linear extrapolation of the leading edges of the XPS valence band spectra. In Chapter 6 we will use this method in detail when evaluating the Cu_2O/ZnMgO heterojunction band offset.

All the measured peaks are calibrated to the peak position the C1s peaks and consistency of the XPS setup was controlled by using Au reference samples. The quantitative evaluation of the XPS spectra require a precise peak area determination, therefore it is essential to use the correct line shape to fit the peak. The positions of atomic core levels peaks are determined by using Gaussian-Lorentzian line shape fittings of the analyzing tool CasaXPS from Neal Fairly (VAMAS Processing Software)[147].

3.2.6 Current density-voltage (j-V) characterization

j-V curves are used to determine the basic PV performance parameters. The photovoltaic cell can be represented by the equivalent circuit model described in Chapter 2 (Figure 2.7 (a)), consisting of a current source, a diode, series resistance (R_s), and a shunt resistance (R_p). From the curve, the parameters such as open circuit voltage (V_{OC}) and short circuit current density (j_{SC}) can be directly determined from the curve. The other parameters such as I_{mp}, V_{mp}, P_{mp}, *FF*, and η can be obtained from the solar cell where I_{mp} and V_{mp} is the current and voltage corresponding to the maximum output power ($P_{mp} = V_{mp}I_{mp}$). These parameters are briefly explained in Chapter 2. In this work, the current density-voltage (j-V) characteristics are obtained in dark and under AM1.5G illumination using an Agilent 4156 C semiconductor parameter analyzer to apply voltage between two terminals and measuring the current. All measurements were performed in ambient temperature and atmosphere.

3.2.7 Capacitance-voltage (C-V) characterization

In addition to determining the *j-V* characteristics of a PV cell, capacitance-voltage measurements are also useful in deriving particular parameters about the device. Since the depletion width of a p-n junction is bias dependent, it behaves like a parallel-plate capacitor with plate spacing equal to the depletion width. The capacitance (*C*) associated with the charge (*Q*) variation in the depletion layer with applied bias voltage (*V*) is called the junction capacitance and can be written as $C = dQ/dV$. The width of the depletion layer and the change in capacitance with applied bias voltage depend on the doping concentration. The Mott-Schottky plot ($1/C^2$ vs. V) gives information related to electrical properties, such conduction type, flat band potential and doping concentration of the semiconductor. The doping density (N) of the absorber can be derived from the slope of the Mott-Schottky curve, as *N* is related to the capacitance (*C*) by:

$$N = 2/qA^2\varepsilon_s[d(1/C^2)/dV] \qquad (20)$$

where *N* is the doping density, *q* is the electron charge, ε_s is semiconductor permittivity, *A* is area, *C* is measured capacitance, *V* is applied DC voltage. The positive slope refers to an n-type semiconductor, while negative slope refers to a p-type semiconductor. The built-in voltage of the junction can be derived from the intersection of the $1/C^2$ curve and the horizontal axis. CV measurements can also be used to determine the deep trap states as a function of frequency.

Chapter 4

Electrochemical deposition of the Cu_2O absorber

In this chapter we will present our investigations on the electrochemical deposition of the Cu_2O absorber on the conductive electrodes. First, we will elaborate the chosen solar cell architecture and the deposition of the conductive coating on the glass substrate by sputtering. Then we will proceed with the description of the electrodeposition process in terms of growth, morphology, structural and optical properties of the layers, in our efforts to develop an appropriate solar cell absorber for the subsequent heterojunction formation.

4.1 Solar cell architecture

The solar cells investigated in the thesis are of the substrate type architecture, which means that the light enters the solar cell structure from the side opposite to the substrate, as shown in Figure 4.1. The structure is therefore: glass/BE (back-side electrode)/Cu_2O/n-layer/TCO. In the course of this thesis different BEs were used, namely Ti/Au, Ti/Ag and Cr/ITO (ITO: indium tin oxide). Electrodes based on Au and Ag [96], [126], [148] were used in the literature for Cu_2O solar cells, achieving state-of-the-art photovoltaic performance. On the other hand, the Cr/ITO electrode is firstly being used in the present work.

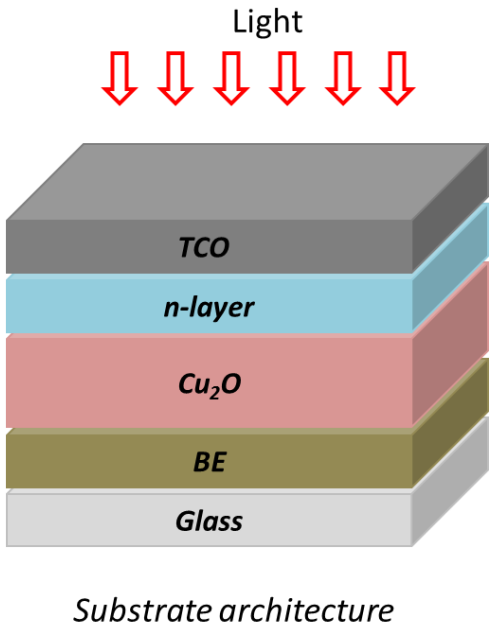

Figure 4.1: Schematic of the solar cell in Substrate architecture

Various factors were taken into account for selecting the back-side electrode: (i) The BE should be sufficiently conductive, as ECD can be performed only on conductive substrates. The BE's conductivity greatly influences the properties of the Cu_2O absorber, as we will see in the following sections. (ii) The BE has to have a high work function, in order to collect the photo-generated holes more efficiently and selectively (serves as an anode). (iii) It should be highly reflecting so it can direct the non-absorbed light back into the Cu_2O film, thus increasing the light path inside the absorber. (iv) It should adhere well on the glass and it should be chemically stable to avoid problems, such as contact delamination during the ECD process. (iv) Finally, the electrode should be ideally composed of low-cost materials. Since the electrodeposition of the Cu_2O absorber depends so strongly on the BE used, we will describe more analytically in the following sections the types and properties of the employed BEs.

4.1.1 Sputter deposition of the BEs

1 mm-thick, soda lime glass slides (Menzel-Gläser) with dimensions 2.5×2.5 cm^2 were used as substrate. Before the deposition, the glass slides were cleaned in ultrasonic bath for 5 min at 60°C in a Hellmanex III-solution, then 5 min in ultrapure water and finally dried with air. Sputter deposition was then used to deposit the BEs. Table 4.1 illustrates the deposition parameters employed for all materials, along with their measured thickness, sheet resistance and their work function (obtained from the literature). We note here that ITO was deposited from a ceramic target with composition 90 wt.% In_2O_3: 10 wt.% SnO_2. All layers were deposited in pure Ar atmosphere and without substrate heating.

Table 4.1: Deposition parameters and properties of back-side electrodes

Electrodes	**Cr/ITO**		**Ti/Au**		**Ti/Ag**	
Materials	Cr	ITO	Ti	Au	Ti	Ag
Ar gas pressure (μbar)	5	2	2	2	2	2
Power density (W/cm^2)	0.49	0.49	0.49	0.25	0.49	0.25
Thickness (nm)	20	160	5	100	5	100
Sheet resistance (Ω/□)	17		0.9		1	
Work function (eV)	(ITO) 4.7 [149]		(Au) 5.1 [150]		(Ag) 4.26 [150]	

To optimize the deposition of the Cu_2O absorber we have focused on the Cr/ITO electrode, as it provided the best combination of properties and cost, especially compared to Au.

Therefore, in the following sections we will first elaborate on the fabrication and characterization of Cu_2O films employing the Cr/ITO electrode, before extending our discussion to the Ti/Au and Ti/Ag electrodes.

4.2 Solar cells on the Cr/ITO BE

4.2.1 Properties of the Cr/ITO electrode

The Cr (20 nm)/ITO (160 nm) electrode is free of precious metals, which are used in high-efficiency Cu_2O solar cells in the literature [96], [126], [148]. Indium is indeed a rare metal, but its cost is lower compared to that of Au or Ag. Further, ITO has a high work function of ~4.7 eV, which is suitable to collect holes. The abundant Cr was used as a buffer as it supports the conductivity of the ITO layer and it has a relatively high work function of 4.5 eV [151]. Moreover, Cr is highly reflecting in the visible range, thus enhancing the light path in the absorber layer, especially for the longer wavelengths. The mean specular reflectance of the Cr/ITO electrode in the window 350-650 nm is 0.41 (see Figure 4.2). Also, Cr has a very good adhesion on the glass substrate, which results in dense and compact films [152]. It also binds strongly to the ITO. Cr has been shown to make stable interfaces with oxides [153] and has been used as interfacial layer to promote adhesion between ITO and Al in optoelectronic devices [154].

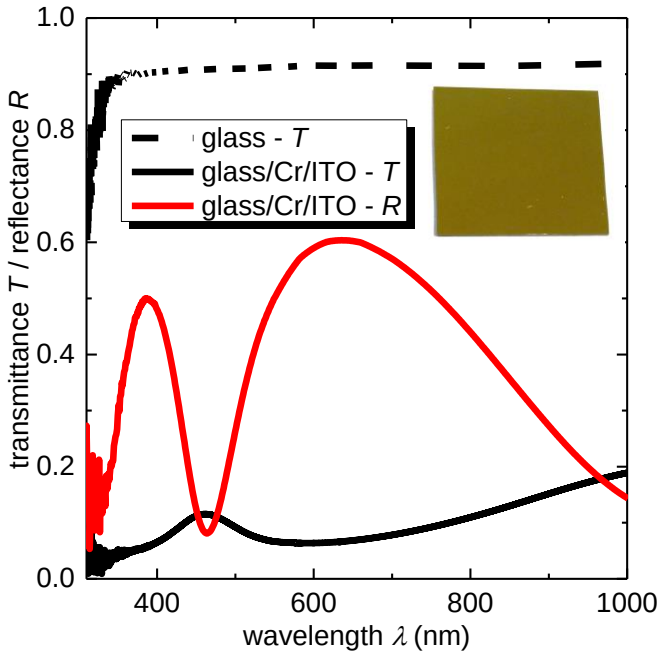

Figure 4.2: The transmittance and mean specular reflectance of Cr/ITO electrode together with the transmittance of glass, (inset) image of sputtered deposited Cr/ITO electrode

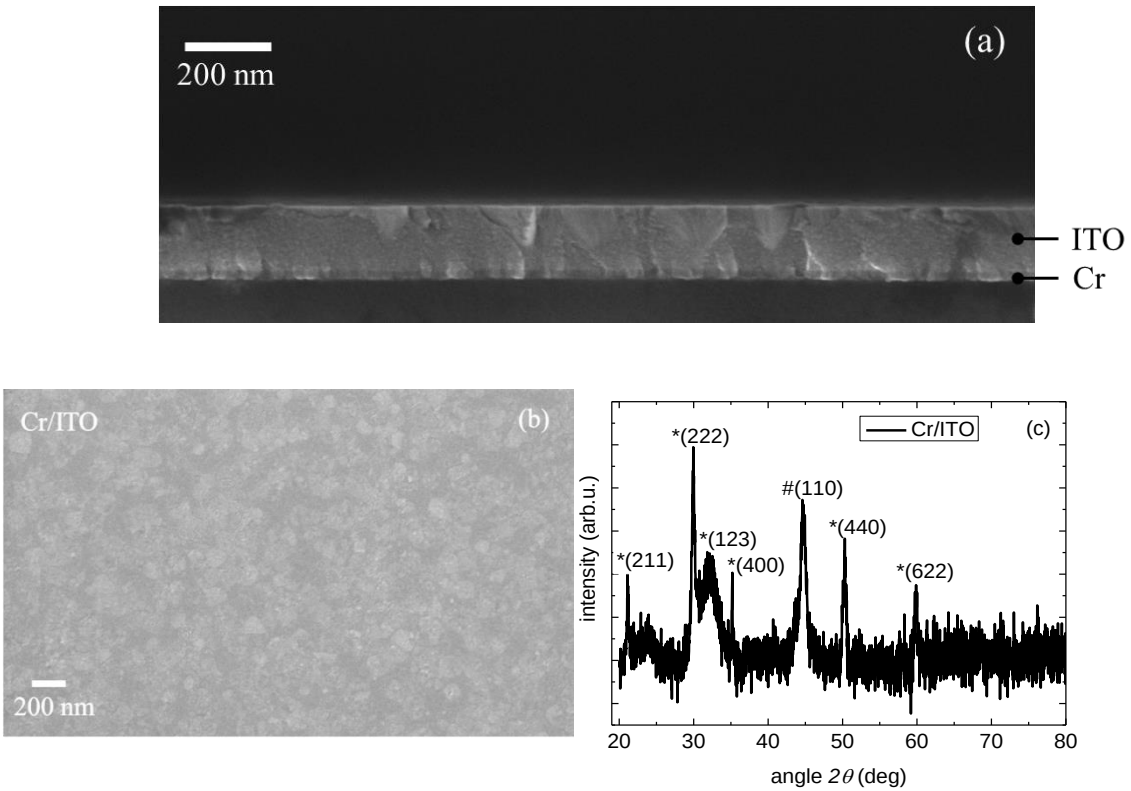

Figure 4.3: SEM images of (a) Cross-section, (b) plane view of the Cr/ITO electrode, (c) XRD of Cr/ITO electrode, the XRD peaks assigned to the ITO are marked with an asterisk (*) whereas the peak assigned to the Cr is marked with the hash key (#)

The cross section and surface SEM images of the electrode (Figure 4.3(a, b)) illustrate the compactness and low roughness of the Cr/ITO electrode. The XRD measurement (Figure 4.3(c)) shows a dominant peak from the (222) planes' reflection of ITO's cubic structure (symmetry group Ia-3) and secondary peaks from the (211), (123), (400), (440) and (622) planes (JCPDS 01-089-4598). The lack of specific texture for the ITO layer is expected, since the sputter deposition takes place without substrate heating, which induces layer crystallization. The XRD peaks of ITO and the (110) peak of the Cr layer (JCPDS 01-085-1336) are marked in Figure 4.3(c). In the following section we will describe the electrochemical deposition of the Cu_2O absorber on the Cr/ITO electrode.

4.2.2 ECD of Cu_2O on Cr/ITO electrode

4.2.2.1 ECD solution preparation and ECD set up

In the literature, a large variety of electrolytic solutions have been used for the electrodeposition of Cu_2O, e.g. copper (II) sulfate and amino acid [155], cupric acetate and sodium acetate [156], copper (II) sulfate and sodium potassium tartrate [157]. In the present

work, an electrolytic solution of copper (II) sulfate and lactic acid is used to deposit Cu_2O films. This solution chemistry is widely used to obtain p-Cu_2O films [158]–[160]. More specifically, an aqueous solution with copper (II) sulfate pentahydrate, lactic acid and de-ionized water was prepared. Table 4.2 shows the precursors and their concentration used for the solution. The solution was stirred for several hours until all grains of copper sulfate were fully dissolved. The solution pH was adjusted to 12.5 by gradually adding sodium hydroxide. Lactic acid was used to stabilize the Cu (II) ions at bath pH > 7, through the formation of copper lactate (Cu-(CH_3 CH (OH) $COO)_2$). A violet bluish color solution was finally obtained at pH 12.5.

Table 4.2: All reagents used to prepare ECD solution

Precursors		
Name	**Formula**	**Concentration**
Copper (II) sulfate pentahydrate	$CuSO_4$.$5H_2O$	0.2 M
Lactic acid	($CH_3CH(OH)COOH$)	3 M
Sodium hydroxide	NaOH	to obtain pH of 12.5

A schematic of the experimental set up used for the deposition is displayed in figure 4.4. In this three-electrode cell set up, current flows between the Cr/ITO (WE) and Ti/Pt (CE), where an Ag/AgCl (RE) electrode is used to control the potential of the WE. The redox reactions that can occur at the WE during ECD are as follows:

$$2Cu^{2+} + 2OH^- + 2e^- \rightarrow Cu_2O + H_2 \quad (21)$$

$$Cu_2O + 2H^+ + 2e^- \rightarrow 2Cu + H_2O \quad (22)$$

$$Cu^{2+} + 2e^- \rightarrow Cu \quad (23)$$

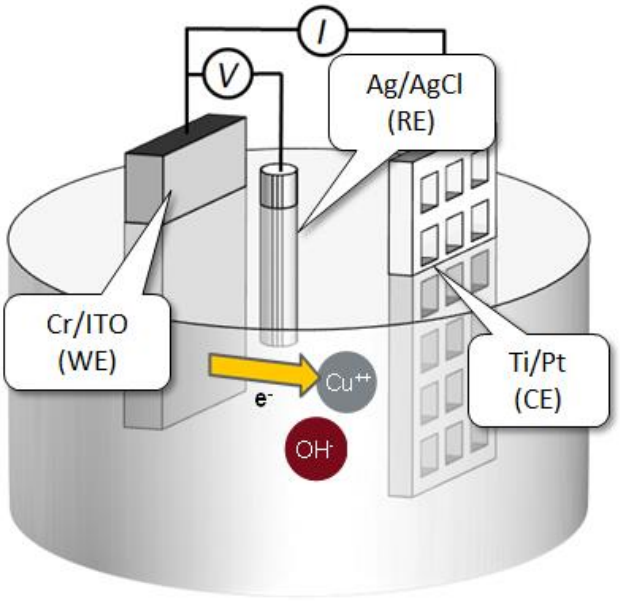

Figure 4.4: Schematic of the experimental setup for ECD

The reactions 21 and 22 are pH-dependent. To favor reaction 21 against 22 the deposition must take place at highly basic pH. To stabilize the Cu^{2+} ions at these conditions, a chelating agent is used, i.e. lactic acid. Reaction 23 is controlled by the applied potential (explained in the next section). The deposition of the Cu_2O is interrupted when a certain charge, Q, has been recorded by AUTOLAB's analog charge integrator. The charge is related to the targeted film thickness, d, through the Faraday's law: $d = MQ/nFA\rho$, where M is the molecular weight of Cu_2O $(143.09\ gr/mol)$, $n = 2$ is the number of electrons involved per electrochemical reaction, $F = 96485.33289\ C/mol$ is the Faraday constant, A is the electrodeposited area in cm^2 and $\rho = 6\ gr/cm^3$ is the density of Cu_2O. After the deposition, the sample is removed from the solution and thoroughly rinsed in flowing deionized water to wash residual salts and unreacted products from the surface.

4.2.2.2 Cyclic voltammetry & determination of potential

Cyclic voltammetry (CV) method was used to determine the reduction potential that would lead to Cu_2O deposition on the Cr/ITO electrode. It is a potential sweep technique to study the electron transfer kinetics. In CV, the potential is scanned at a specific rate and the current flowing through the electrochemical cell is measured. Figure 4.5 shows a representative CV measurement with the Cr/ITO as the cathode, taken with a ramp rate of 10 mV/sec.

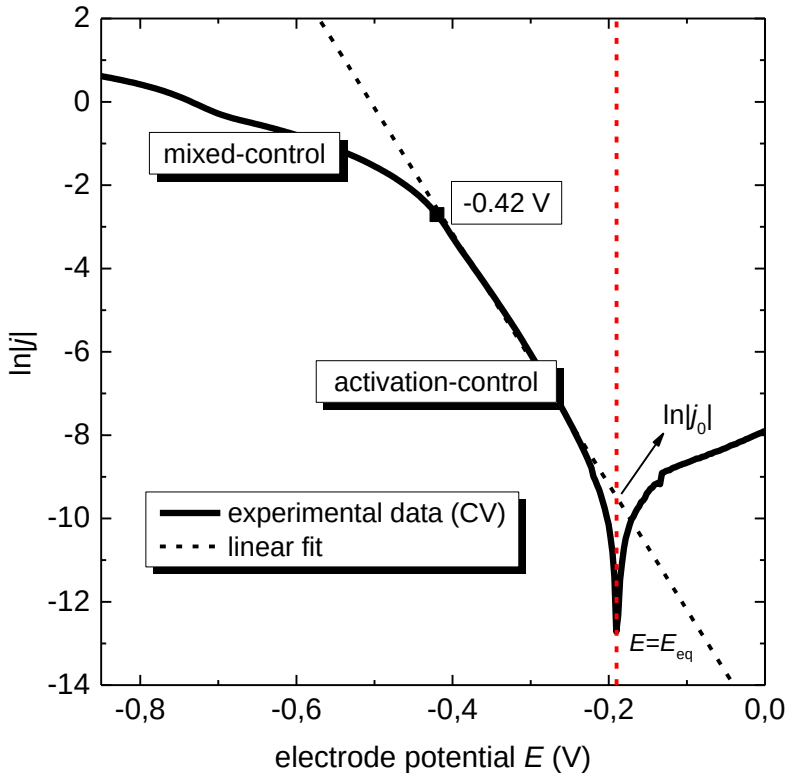

Figure 4.5: Semi-logarithmic current density *j* versus electrode potential *E* (V) curve of Cr/ITO substrate used to determine the deposition potential for the Cu_2O

The measured current density *j* is plotted in semi-logarithmic scale as a function of the applied potential. The E_{eq} is the equilibrium potential (shown in figure 4.5), for which the reduction and oxidation reactions at the electrode take place at equal rates (η = 0). As the potential departures from the equilibrium, the current density increases exponentially with E as given by the Butler-Vollmer equation (10):

$$ln|j| = ln|j_0|exp\left[-\left(\frac{\alpha nF}{RT}\right)\eta\right]$$

where, j_0 is the exchange current density (the reaction rate at the equilibrium potential), *n* is number of electrons transferred, α is the dimensionless cathodic charge transfer coefficient for a single rate-determining step [161], *R* is the universal gas constant (8.3144598 J/(mol·K)) and *T* is bath temperature (50°C) during deposition. The kinetic parameters of B-V equation i.e. α and j_0 can be extracted from the CV measurement. The linear fit yields a slope (-αF/RT) of -30.12, i.e. α = 0.84. This value represents the fraction of the electrode-electrolyte

interfacial potential that assists in lowering the free energy barrier for the electrochemical reaction to take place.

The choice of the optimum (negative) over-potential is very important for the well-defined growth of Cu_2O films (as already discussed in chapter 3). The activation-controlled electrode reaction promotes well-defined islands of the deposit, as dictated by differences in the energy between the different facets [162] whereas the mixed-control electrode reaction leads to irregular island growth due to the mass-transport limitation. So, in order to have high quality deposits as well as high deposition rates, the optimum deposition potential for the Cu_2O would be the one corresponding to the transition between the activation and the mixed-control region i.e. -0.42V (see figure 4.5).

4.2.2.3 Nucleation and growth procedure

In order to study the effect of deposition potential on the Cu_2O films, it is necessary to understand the deposition procedure during ECD. Figure 4.6 shows the current transient during the Cu_2O deposition obtained for the Cr/ITO electrode at potentiostatic mode. For a particular (fixed) deposition potential to the WE, the current density first increases, reaches a maximum in its absolute value (denoted as j_{max}) and then decreases.

The crucial step in the electrochemical deposition is the early stage of nuclei formation on the substrate surface, as it determines the final characteristics of the deposit (e.g. morphology). The electrodeposition curve (figure 4.6) can be divided into two stages. Initially, the current density increases (stage 1) due to the increase of active surface area as the nuclei grow on the substrate surface. The growth of each nucleus depends on the mass transfer from the bulk to the nucleation centers, which is defined by their diffusion zones. As the growth continuous, the coalescence of the diffusion zones of the neighboring nuclei gives rise to the maximum in the current density (j_{max}). The current density declines (Stage 2) after the j_{max} due to the decrease in the surface area, as the mass transfer towards the nucleation centers changes from hemi-spherical to linear diffusion [134].

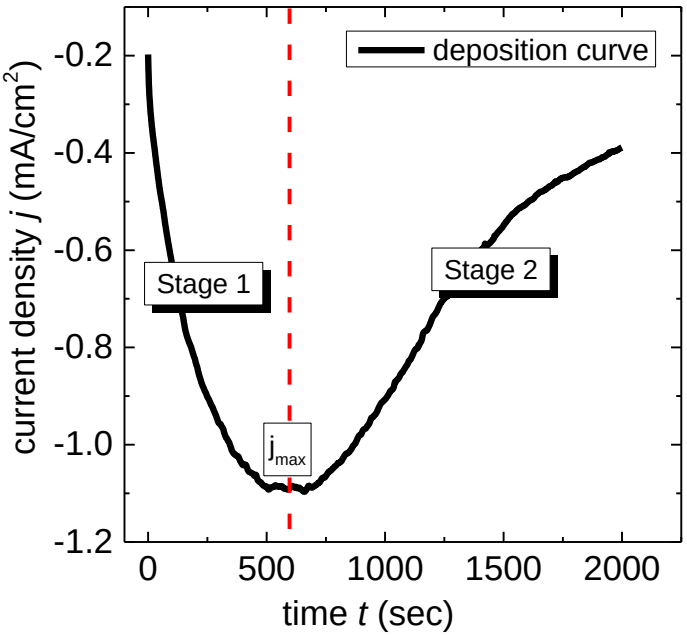

Figure 4.6: The current transient plot of Cr/ITO electrode

ECD of Cu_2O was performed at different negative potentials i.e. at -0.42 V, -0.5 V and -0.6 V to investigate the influence of the potential on the growth evolution and morphology of the Cu_2O as a function of the deposition time.

Figure 4.7 shows the current transient plots at different over-potential i.e. -0.42 V, -0.5 V and -0.6V. The current densities for the applied potentials first increased, reached the maximum and then decreased, as described previously. Clearly, for higher (absolute) values of over-potential, the maximum current density (j_{max}) position shifts to shorter time instances, i.e. at 179s, 569s and 903s for -0.6V, -0.5V and -0.42V, respectively. Indeed, for higher over-potentials, the surface diffusion of atoms to the growing islands becomes increasingly pronounced, and along with it the nucleation density. For an island aspect ratio of 1, the minimum thickness (d_{crit}) required for island coalescence is $d_{crit} = (2\sqrt{N})^{-1}$ [163]. This means that the denser the nucleation is, the faster will be the island coalescence, which shifts the current density maximum position to shorter time instances. The nucleation density also affects the grain size of the film, as the average grain size at island coalescence varies with $N^{-1/2}$ [163]. Therefore, for high over-potential, due to high nucleation density, the critical thickness for island coalescence is reduced and smaller grain size is obtained.

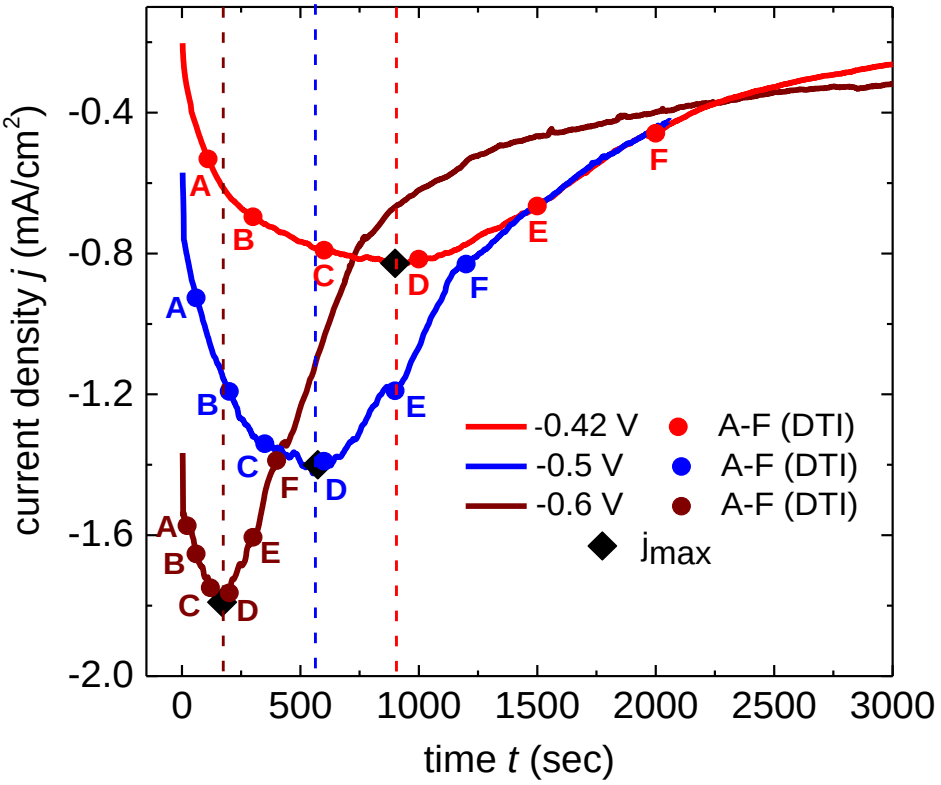

Figure 4.7: Potentiostatic current-time transients for -0.42 V, -0.5 V and -0.6V and for the growth evolution the deposits were taken at different time instances (DTI) of the deposition process of the Cu_2O film as marked A-F points for different potentials

For low over-potential, the deposition rate is low, the nucleation becomes sparser on the electrode surface, whereas the diffusion of the atoms at the already formed islands is favored. As a consequence, the critical thickness for island coalescence increases, which makes the maximum current density position shift to later time instances during the deposition process. The grain size, on the other hand, becomes larger for low over-potential, which is desired for improved electrical properties of the absorber.

For the nucleation process, the theoretical current transients representing the S-H models for instantaneous and progressive nucleation are plotted along with the experimental (j/j_{max}) vs. (t/t_{max}) curves for the potentials -0.42 V, -0.5 V and -0.6 V (figure 4.8). j_{max} is the maximum current density for each curve, corresponding to the time instance t_{max}. For the -0.42 V and -0.5 V applied potentials, the experimental data follow closely the instantaneous nucleation curve for $t/t_{max} < 1$. However, for $t/t_{max} > 1$ the experimental curves present a significantly faster current decrease compared with either of the models. This is attributed to the fast overlapping of the diffusion zones of the growing Cu_2O particles. For the highest applied potential of -0.6 V, the form of the experimental curve is in line with the

instantaneous nucleation model, but the experimental data differ considerably from the model for t/t_{max} < 1.

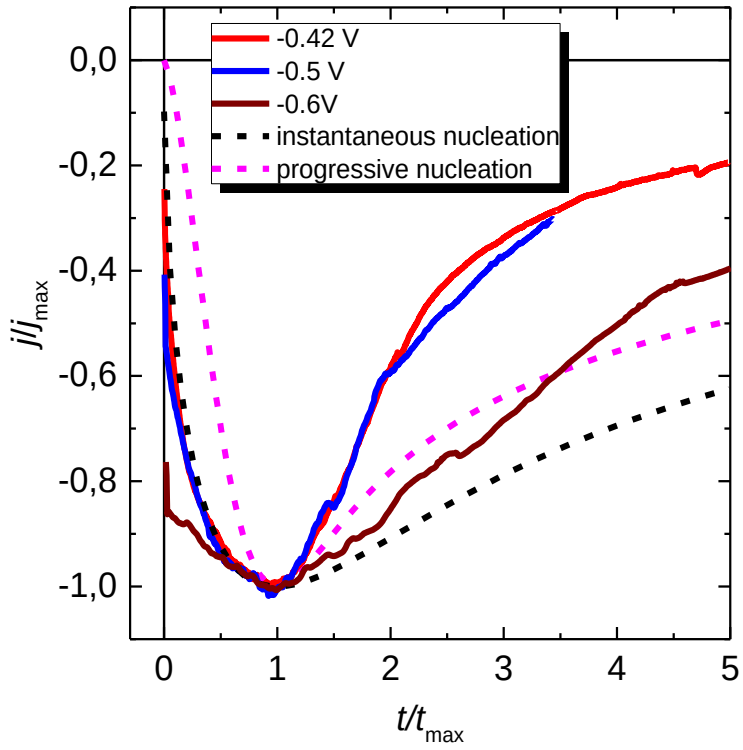

Figure 4.8: The dimensionless quantity (j/j_{max}) versus (t/t_{max}) for the experimental and theoretical curve

We have further investigated the growth evolution of the Cu_2O film over time for different deposition potentials. For this, SEM images and X-Ray diffractograms were acquired at different time instances of the deposition process, marked as points A-F in figure 4.7.

The SEM images for -0.42 V are shown in figure 4.9, for -0.5 V in figure 4.10, and for -0.6 V in figure 4.11. From these images, indeed, it is shown that the growth of the Cu_2O absorber takes place through instantaneous nucleation with the formation of 3D islands. The nuclei do not grow independently, i.e. clusters of nuclei at close proximity merge to form single islands and as the deposition continuous the island density decreases from its initial value. The average lateral dimension of an ensemble of grains for -0.42V was measured and plotted as a function of time in Figure 4.9 (bottom).

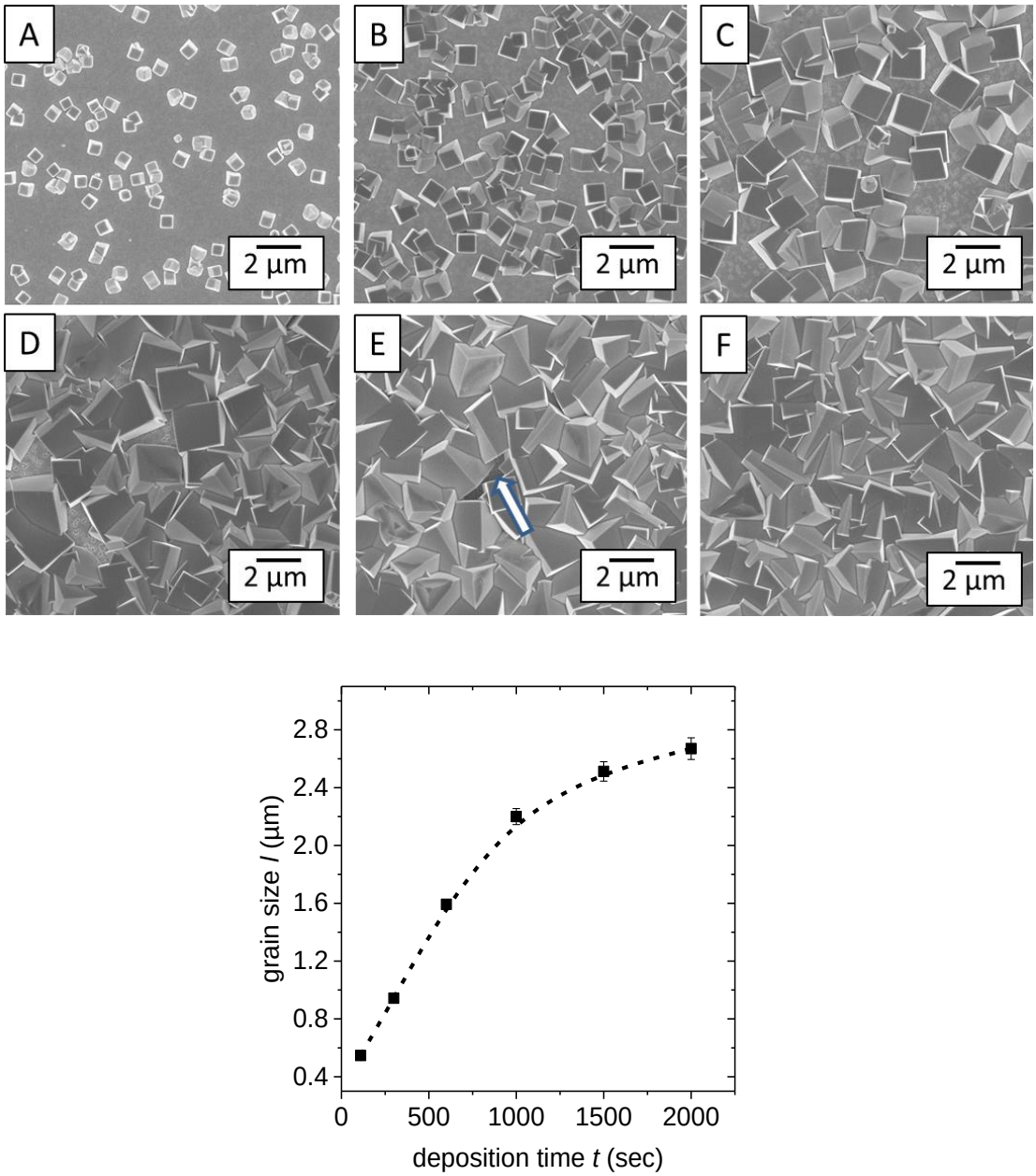

Figure 4.9: Plane view SEM images of the absorber obtained for the deposition times marked by points A-F for -0.42 V, (bottom) temporal evolution of the Cu_2O grain size for -0.42 V, as extracted from the SEM images

In the beginning of the growth, until t~600 s, the grain size increases almost linearly with time. Subsequently, the lateral grain growth slows down due to steric hindrance and as the deposition continuous the size of the grain saturates. Islands with dimensions up to ~2700 nm are measured after 2000s deposition. In the SEM image corresponding to point E (1500s) voids can still be observed, as the one marked with the arrow. These voids eventually disappear for longer deposition times.

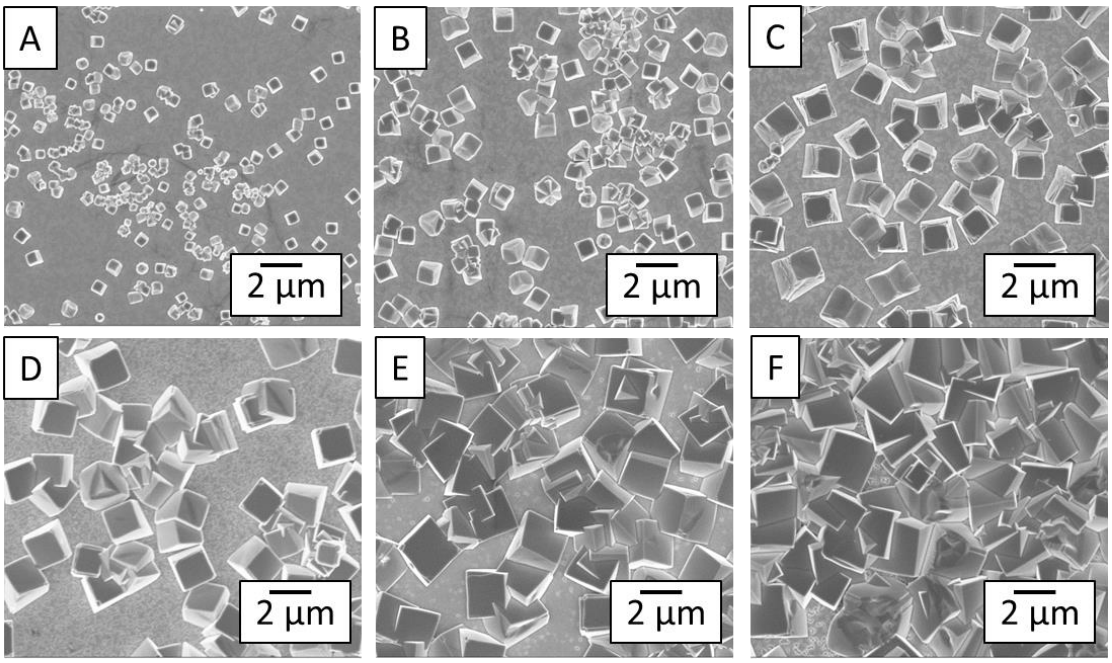

Figure 4.10: Plane view SEM images of the absorber obtained for the deposition times marked by points A-F for -0.5V

For 2000s deposition (image F), no voids are observed in the film. Most importantly, the islands of the deposited film are well-faceted, with low density of structural defects. On the other hand, for higher applied potentials (i.e. for -0.5V and -0.6V) the deposited films become less well faceted, with larger amount of structural defects (figure 4.10 and 4.11).

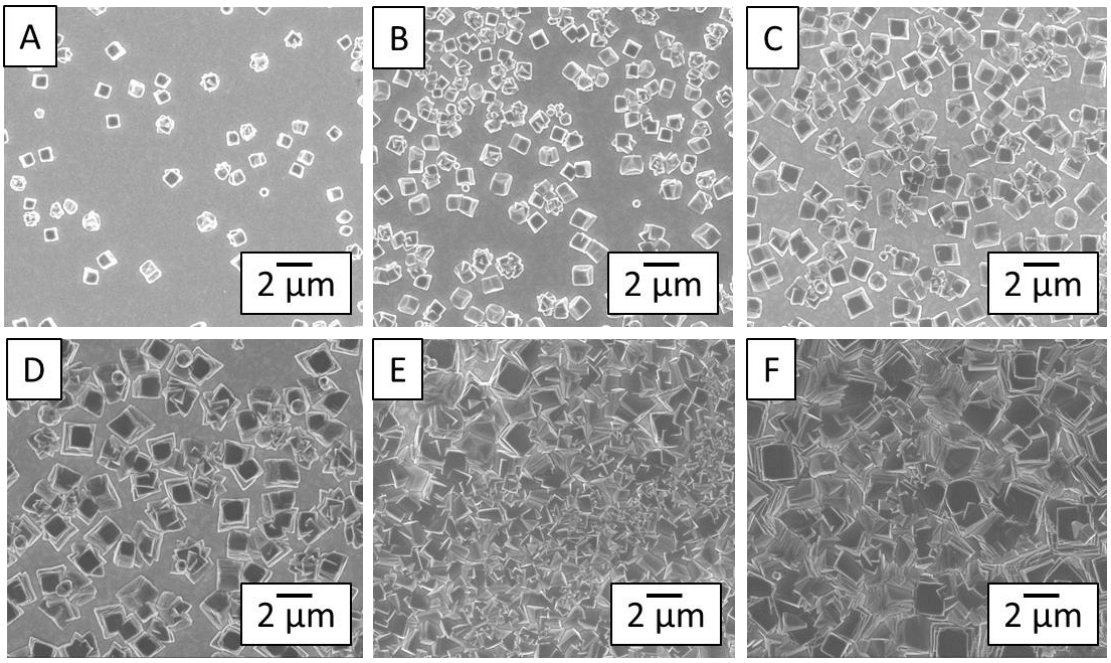

Figure 4.11: Plane view SEM images of the absorber obtained for the deposition times marked by points A-F for -0.6V

The crystal structure of the Cu_2O deposits at -0.42 V, -0.5 V and -0.6 V was investigated by XRD. The obtained diffractograms for different deposition times are shown in figure 4.12 (a), (b) and (c). For -0.42 V, the strongest peaks stem from the (111) and (200) plane reflections from the early deposition stage. In the course of the deposition, the two main peaks become alternatively dominant, until the (111) peak is finally dominating over the (200) for large deposition times. Apart from these two peaks, the one stemming from the (220) planes is also significant. For the deposition potential of -0.5 V, the strongest peaks remain the ones from the (111) and (200) planes.

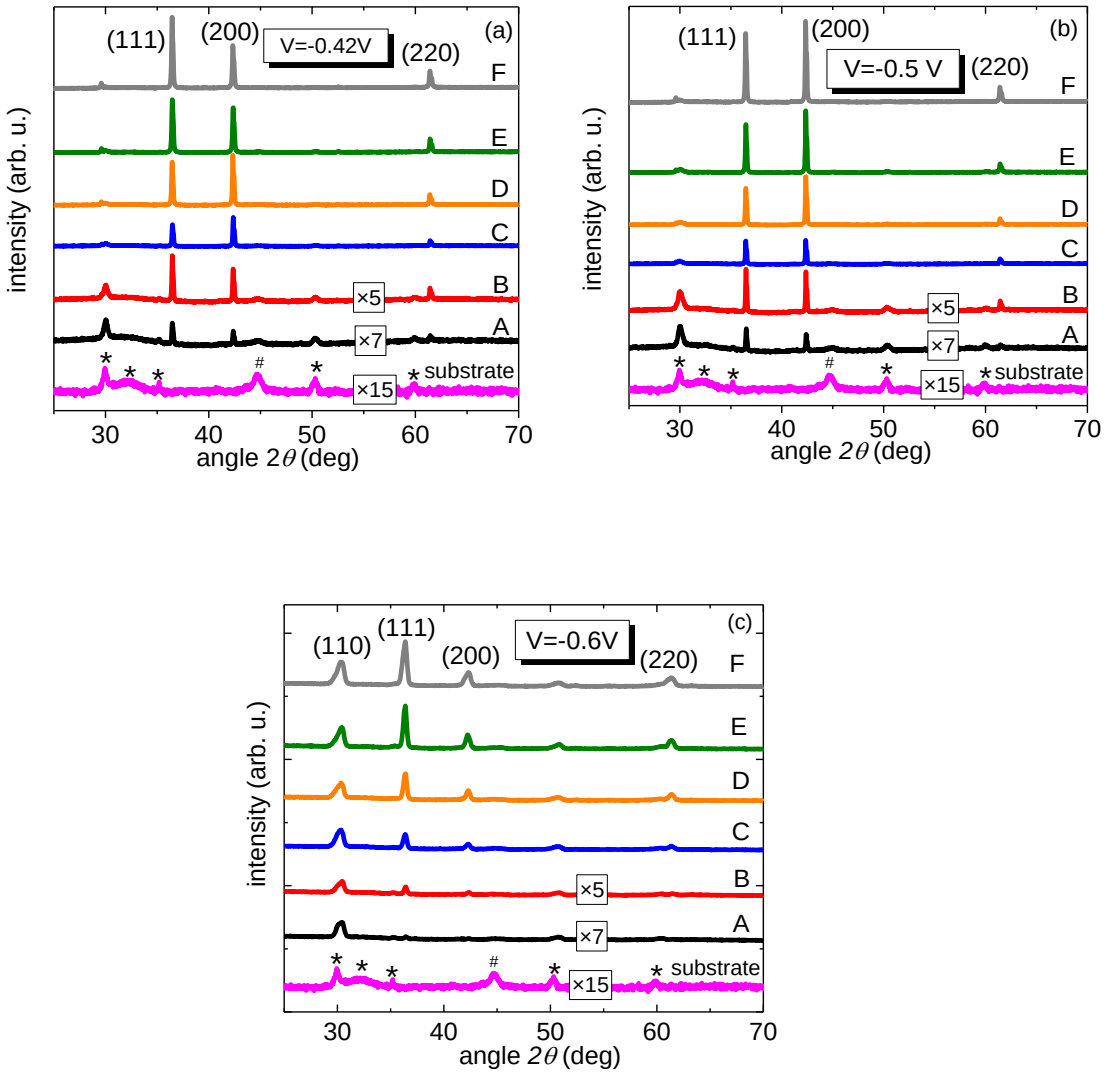

Figure 4.12: X-ray diffractograms obtained for different times of Cu_2O electrodeposition at: (a) E = -0.42 V, showing the alternation between the (111) and (200) as prominent textures, (b) E = -0.5 V, showing the (111) and (200) as prominent textures, whereas (200) planes prevails for thicker films and (c) E = -0.6 V, showing the (111) and (200) as prominent textures, however (110) planes are also significant

For large deposition times the (200) peak dominates over the (111). For the -0.6V the diffractogram peaks are the same but their intensity significantly lessens with respect to the previous cases, showing that the obtained film is far less textured. In conclusion, among the different potentials applied for the deposition, the Cu_2O films deposited at -0.42 V present the most pronounced texture and the fewer structural defects.

Moreover, the texture of the Cu_2O film is finally determined by the combined effect of the solution pH, as well as the substrate used for the deposition. Due to the high pH value of the solution, there is large supply of oxygen (through the OH^-) that favors the growth of planes with largest oxygen density, i.e. the (111) planes of the cubic Cu_2O [164]. On the other hand, the Cr/ITO electrode is poly-textured with certain crystal orientations favoring the (111) growth of Cu_2O whereas others favoring the (200) or (220) growth.

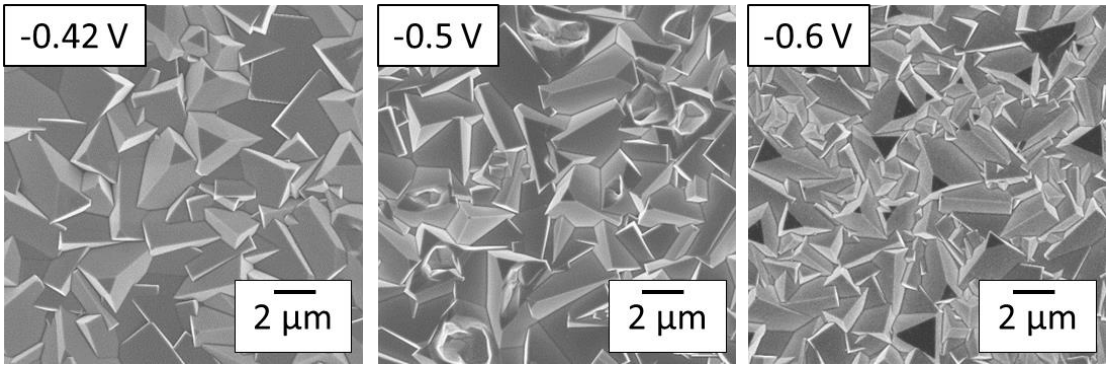

Figure 4.13: SEM images of 2.5 µm thick Cu_2O absorber at -0.42 V, -0.5V and -0.6V deposition potentials

The SEM images of 2.5 µm thick Cu_2O films deposited at -0.42 V, -0.5 V and -0.6V are shown in figure 4.13. With increasing applied potential, the grain size of the Cu_2O film becomes smaller and the films become more defect-rich which is not desirable for the solar cell absorber. An efficient absorber should have large grains, should be textured and void-free. This is obtained by using low potential during deposition. To meet these requirements the potential -0.42 V was selected for the deposition of Cu_2O films on the Cr/ITO electrode and the development of solar cells.

Figure 4.14 shows a cross-section SEM image of the electrodeposited Cu_2O film on Cr/ITO substrate with a 20 nm-thick ZnO layer deposited atop. The film features a rough surface due to the large and well-faceted grains of Cu_2O. Optical measurements were performed for the Cu_2O film on the Cr/ITO substrate. The specular and integrated reflectance spectra for the glass/Cr (20 nm)/ITO (160 nm)/Cu_2O (2.5 µm) sample are shown in figure 4.15.

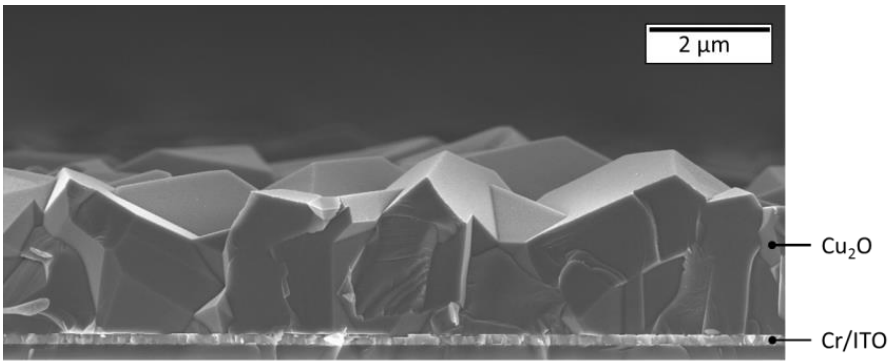

Figure 4.14: Cross-section SEM image of Cu_2O film deposited on Cr/ITO substrate

The specular reflectance is much lower than the integrated because of the pronounced absorber roughness, which increases the diffuse component of the reflectance. The optical band gap of Cu_2O film was extracted from the integrated reflectance measurement. The most direct way of extracting the optical band gap, is to simply determine the wavelength at which the extrapolations of the "base line" (2) and the absorption edge (1) cross [165], as shown in figure 4.15. This method yields a value of E_G=1.93 eV, in good agreement with the value extracted earlier for a similarly prepared Cu_2O film [166].

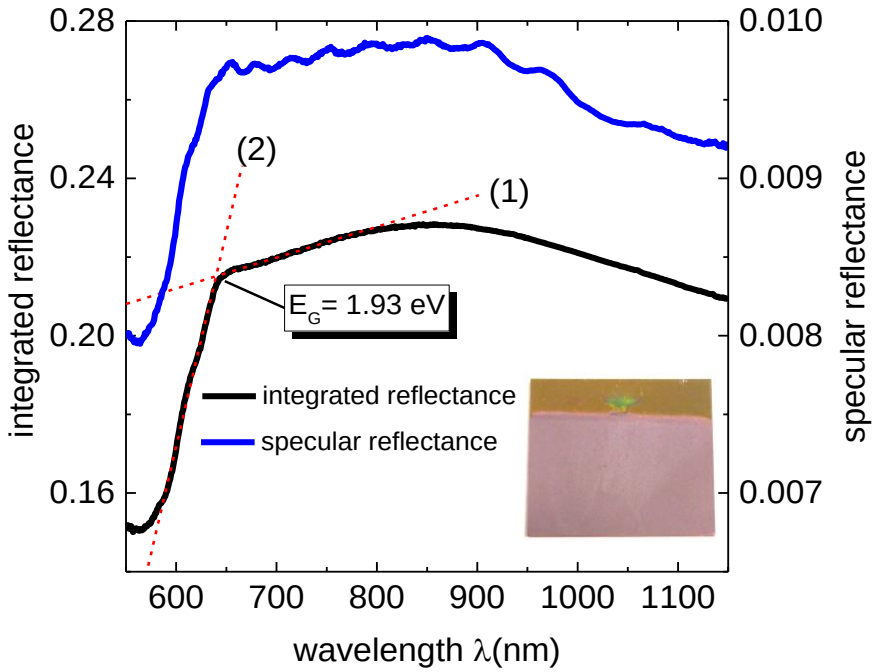

Figure 4.15: Integrated reflectance spectra of the glass/Cr/ITO/Cu_2O sample with the extraction of the optical bandgap of the absorber, (inset) the electrodeposited Cu_2O film on the Cr/ITO substrate

4.2.2.4 Post-deposition annealing

Post-deposition annealing of the Cu_2O films was performed in different atmospheres and temperatures, in order to investigate whether the texture and/or the conductivity of the absorber could be improved.

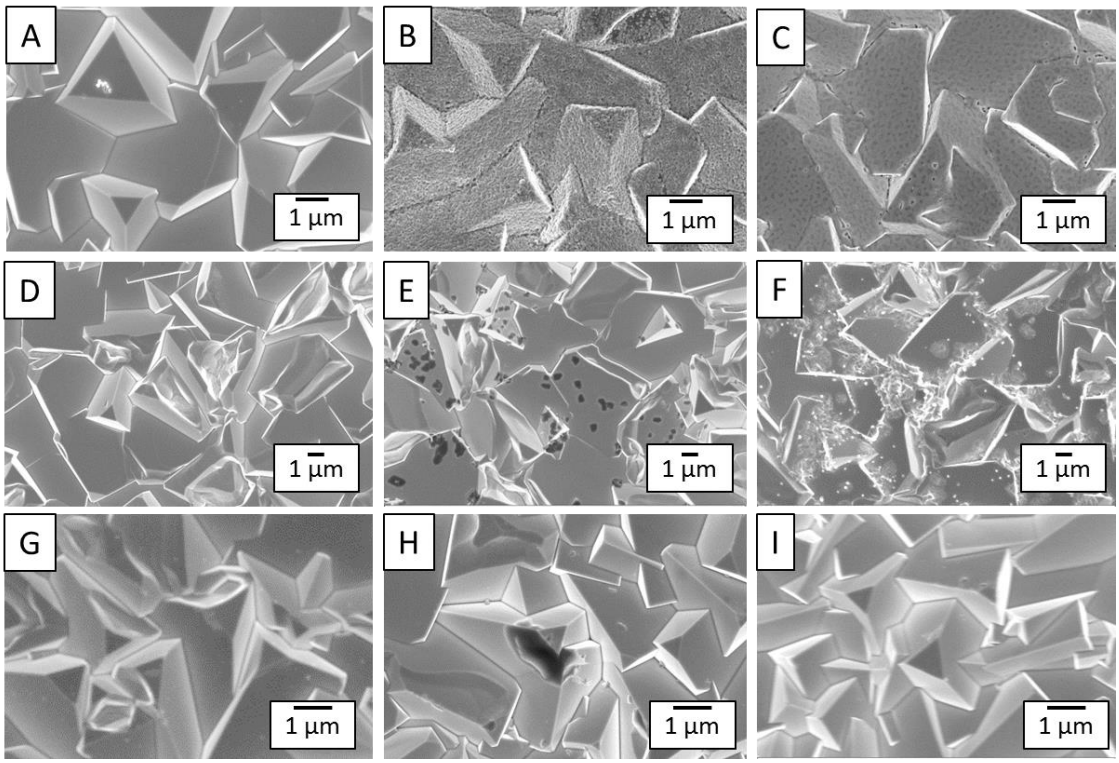

Figure 4.16: SEM images of the Cu_2O morphology annealed at different atmospheres and temperatures: Annealed in H_2/N_2 atmosphere: (A) as-deposited, (B) at 150°C, 15 min (C) at 250°C, 15 min. Annealed in Ar atmosphere: (D) as-deposited, (E) at 150°C, 15 min (F) at 250°C, 15 min. Annealed in vacuum: (G) as-deposited, (H) at 150°C, 15 min (I) at 250°C, 15 min

The films were annealed in forming gas (H_2N_2), Argon (Ar) and vacuum atmospheres at 150°C and 250°C (figure 4.16). Annealing in H_2N_2 atmosphere reduces the Cu_2O films (figure 16 (b and c)). The XRD analysis reveals the presence of Cu peaks (at 150°C and 250°C) as shown in figure 4.17 (a). The Cu peak is marked with the hash key (#) whereas Cu_2O peaks are marked with the asterisk (*). The Cu content increased with increasing annealing temperature. The reduction of the Cu_2O film was accompanied by a drastic decrease of its sheet resistance from 4×10^4 Ω cm to ~1-3 Ω cm. On the other hand, annealing in Ar and vacuum atmosphere increased the resistivity of Cu_2O film. Vacuum annealed Cu_2O films at 250°C (figure 4.16 (I)) showed the highest increase in resistance from 4×10^4 Ω cm to 2×10^5 Ω cm. The XRD analysis was performed and the results are illustrated in figure 4.17 (b and c). No impurity peaks from

Cu or CuO are detected for the Ar and vacuum annealed samples. At the same time the (111) texture in the annealed samples becomes more pronounced as opposed to the as-deposited ones. This is easily seen by comparing the intensity of the (111) to the (200) peaks.

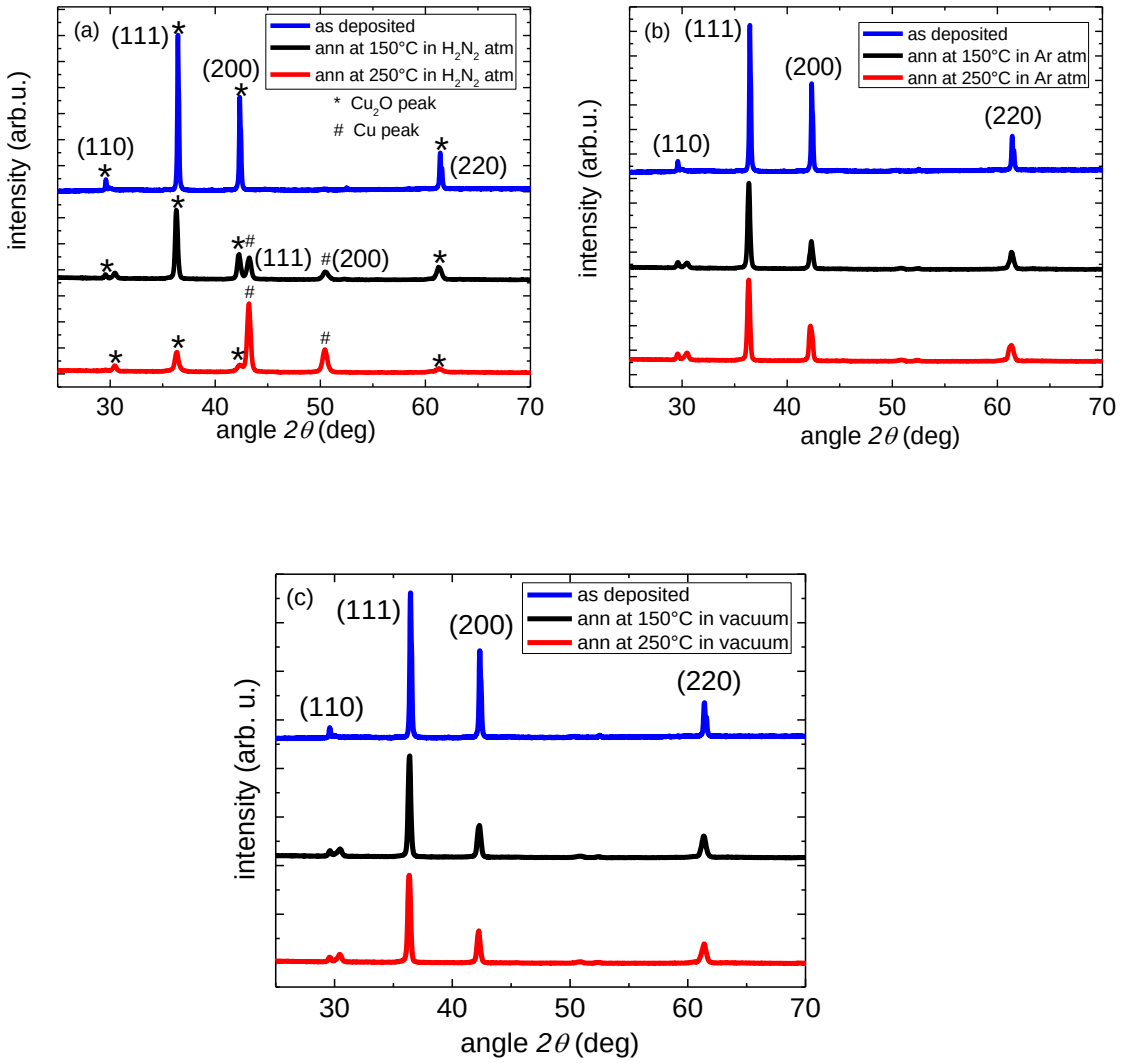

Figure 4.17: X-ray diffractograms obtained for the samples annealed at different atmospheres and temperatures, a: Annealed in H_2/N_2 atmosphere, b: Annealed in Ar atmosphere, c: Annealed in vacuum

4.2.2.5 Effect of bath temperature

We have investigated the effect of the bath temperature on the Cu_2O morphology and therefore on the PV performance. While varying the bath temperature, all the other parameters of ECD, such as pH, solution concentration and applied potential were kept constant. Figure 4.18 shows the CVs for the Cr/ITO substrate at two bath temperatures: 50° and 60°C. The kinetic parameters of electrodeposition, such as j_0 and α are influenced by varying the bath temperature.

The rate of an electrochemical reaction is determined by the activation energy barrier, ΔG, i.e. the energy required to promote the charge transfer across the double layer for the reaction at an electrode. The rate constant, k, for an electrochemical reaction is a function of the Gibbs free energy of activation:

$$k = \frac{k_B T}{h} exp\left(-\frac{\Delta G^*}{RT}\right)$$

With increase in temperature, ΔG decreases ($\Delta G = \Delta H - T\Delta S$) i.e. the height of the energy barrier decreases and the rate of the electrochemical reaction increases. Also, the increase in temperature affects the mobility (u) of the ions in the solution, which is related to the diffusion coefficient (D) through the Nernst-Einstein relation as:

$$u = \left|\frac{zF^2 D}{RT}\right|$$

The mobility increases with temperature due to a decrease in the viscosity of the electrolyte, which increases diffusivity. The decrease in activation energy and increase in ionic mobility with temperature enhances the reaction rate at equilibrium (i.e. j_0).

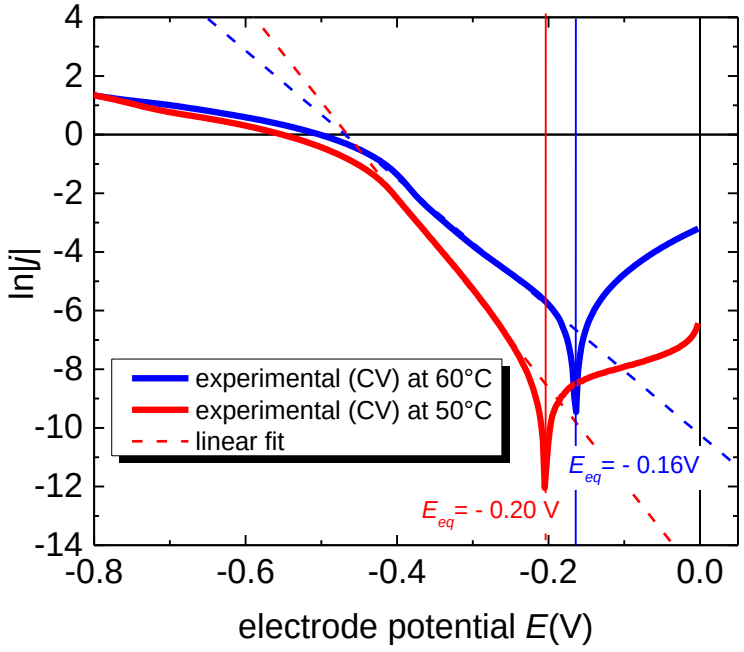

Figure 4.18: Semi-logarithmic current density versus electrode potential curve, used to determine the deposition potential for the Cu_2O layer at different temperatures for fixed pH

The magnitude of the exchange current density in an electrochemical reaction is of paramount importance as it determines the overall activation over-potential needed for the reaction. For instance, if the exchange current density is high, low activation over-potential is required for the reaction and if the exchange current density is low, no significant current will flow unless large activation over-potential is applied. The exchange current density, slope and charge transfer coefficient values extracted from the CV measurements at the two temperatures are illustrated in Table 4.3.

Table 4.3: Kinetic parameters of B-V equation at various temperatures

Temperature (^0C)	*K*	*Slope*	α	lnj_0	$E_{eq}(V)$
50	323	-33.12	0.90	-8.7	-0.20
60	333	-22	0.63	-6.7	-0.16

The slope describes the potential dependent charge transfer coefficient. With temperature, the exchange current density increases and the slope decreases (Table 4.3). This demonstrates that the activation energy required for the electron transfer process decreases. Figure 4.19 shows the potentiostatic current transient curves at 50°C, 60°C, and 70°C as a function of deposition time for E = -0.45 V. It is clear from the curves that at constant over-potential, increased temperature accelerates the electrode kinetics.

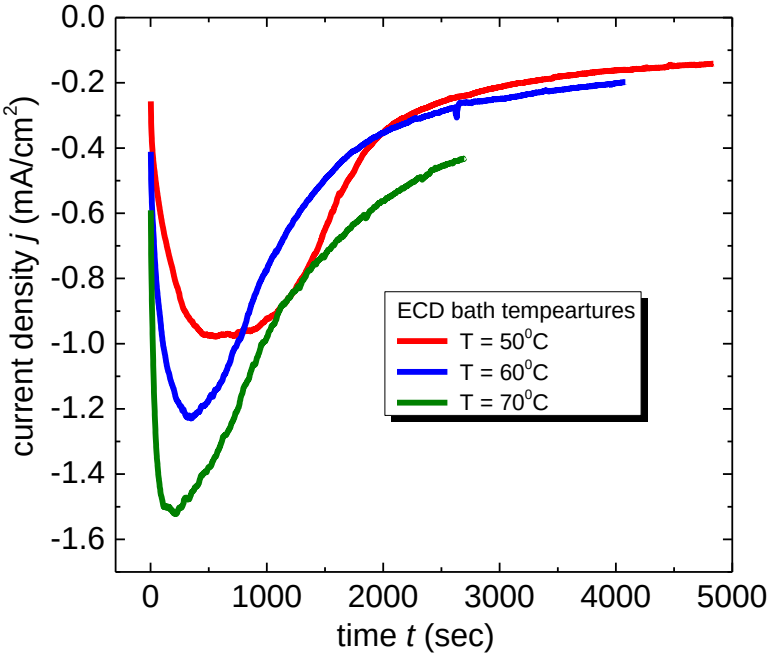

Figure 4.19: The transient curve of the current density during Cu_2O deposition as a function of the deposition time

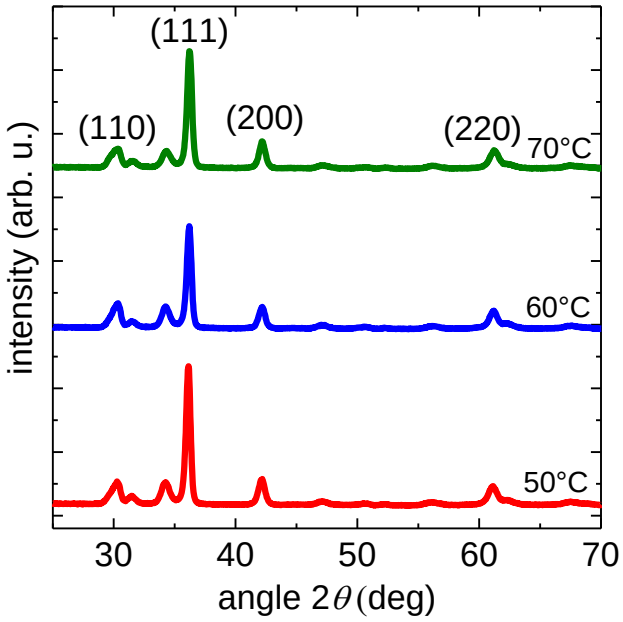

Figure 4.20: X-ray diffractograms of Cu_2O films electrodeposited at different bath temperatures

Figure 4.20 shows the X-ray diffractograms of electrochemically deposited Cu_2O films with increasing bath temperatures. Peaks originating from the (111), (200) and (220) plane reflections are obtained for all deposited films. The (111) is the strongest peak in all cases, illustrating that the preferred crystal orientation for the Cu_2O films remains unchanged with increasing bath temperature. Furthermore, the theoretical current transients of the S-H model are plotted with the experimentally obtained (j/j_{max}) vs. (t/t_{max}) curves for T= 50°C, 60°C and 70°C, in order to determine the type of the nucleation mechanism (figure 4.21).

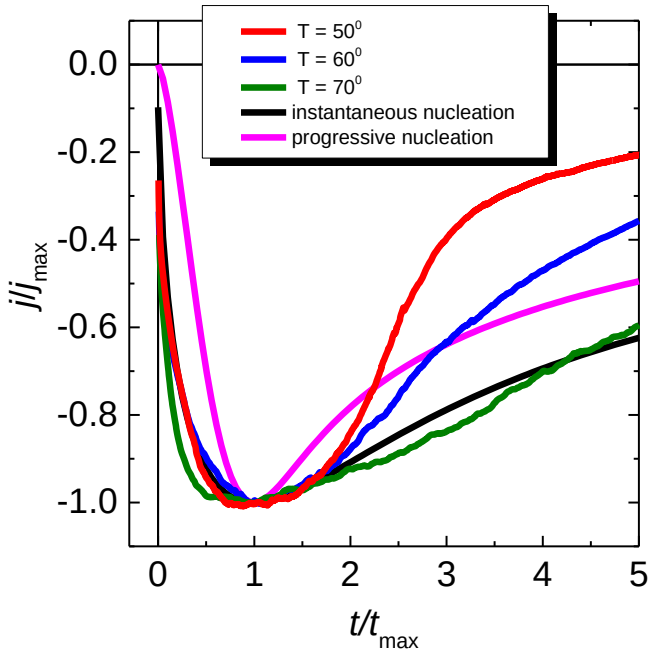

Figure 4.21: The dimensionless quantity (j/j_{max}) versus (t/t_{max}) for the experimental and theoretical curve for different temperatures

For the 50°C and 60°C, the experimental data follow the theoretical instantaneous nucleation curve for t/t_{max} < 1. However, for t/t_{max} > 1 the experimental current decays more rapidly than predicted by both instantaneous and progressive nucleation modes. But in the case of higher temperature i.e. at 70°C the experimental response for has the closest agreement with the instantaneous nucleation model for t/t_{max} > 1. The SEM images of the Cu_2O films at bath temperature of 50°C, 60°C, and 70°C are shown in figure 4.22.

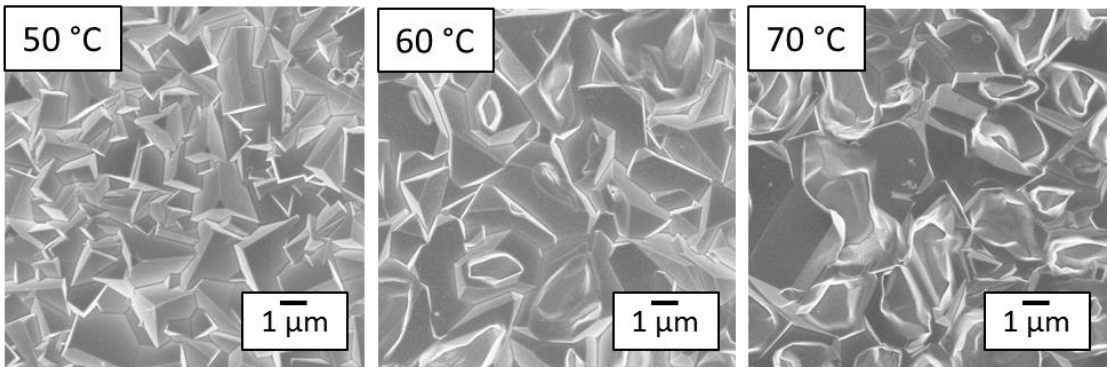

Figure 4.22: SEM images of Cu_2O films at ECD bath temperatures of 50°C, 60°C, and 70°C

4.3 Solar cells on Ti/Au or Ti/Ag BEs

4.3.1 Properties of the electrodes

As we saw before, the Ti/Au (100 nm) and Ti/Ag (100 nm) electrodes are conductive, have high work function (as shown in table 4.1) and they are highly reflective in the visible region, which enhance the light path in the absorber layer, thus promoting absorption. The plane view of a sputtered Ti/Au electrode is shown in figure 4.23, illustrating a surface with very low roughness.

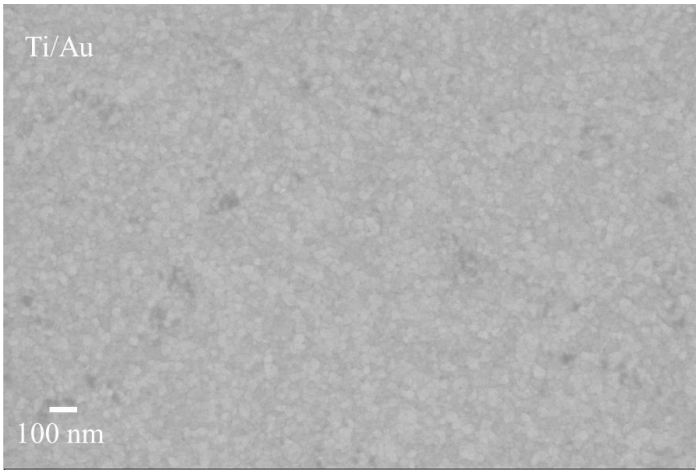

Figure 4.23: SEM image of the sputtered deposited Ti/Au electrode

4.3.2 ECD of Cu_2O on Ti/Au and Ti/Ag electrodes

The Cu_2O deposition on Ti/Au and Ti/Ag substrates was performed by using the same protocol as described above. Due to practically the same electrical conductivity of both electrodes, the ECD of Cu_2O is described in detail only for one electrode i.e. Ti/Au electrode.

The CV was performed to determine the reduction potential which leads to Cu_2O deposition on the Ti/Au electrode. The measured current density *j* is plotted as semi-logarithmic scale as a function of applied potential as shown in figure 4.24. As over-potential departures from equilibrium, the current density increases exponentially with E according to the B-V equation as described above. The slope ($-\alpha F/RT = -33.12$) of the linear fit yields $\alpha = 0.92$. For the well-defined growth of Cu_2O films as well as high deposition rate the optimum deposition potential for the Cu_2O on Ti/Au electrode would be the one corresponding to the transition between the activation to the low mixed-control region i.e. -0.3V.

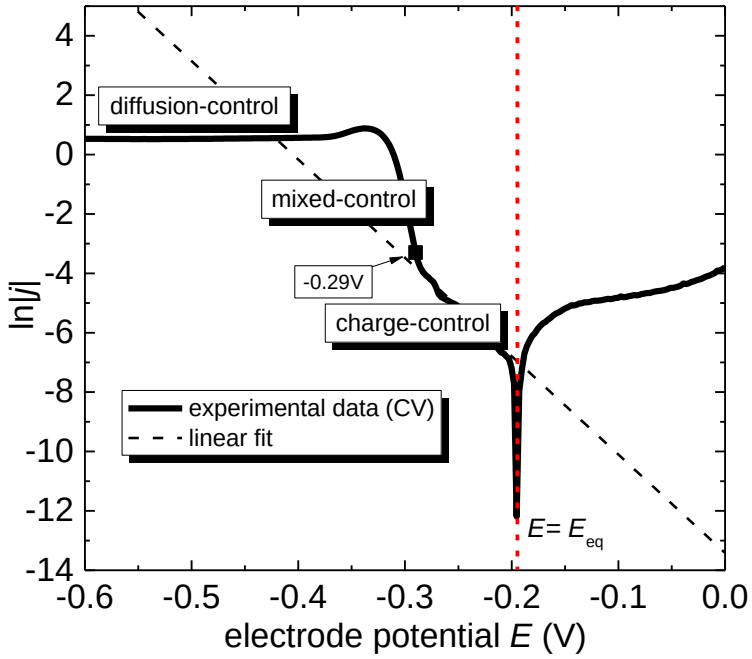

Figure 4.24: Semi-logarithmic current density versus electrode potential for Ti/Au substrate

Figure 4.25 (a) shows the current transient of Cu_2O deposition curve obtained for the Ti/Au substrate for potentiostatic mode. The current density first increases, reaches the maximum (stage 1) position and then decreases (stage 2). The high conductivity of the substrate permits high current densities even for very low over-potential. For the Ti/Au substrate, the nucleation is fast and therefore the maximum position is attained in a very short time interval (~7 secs) during the application of the potential (figure 4.25 (a)).

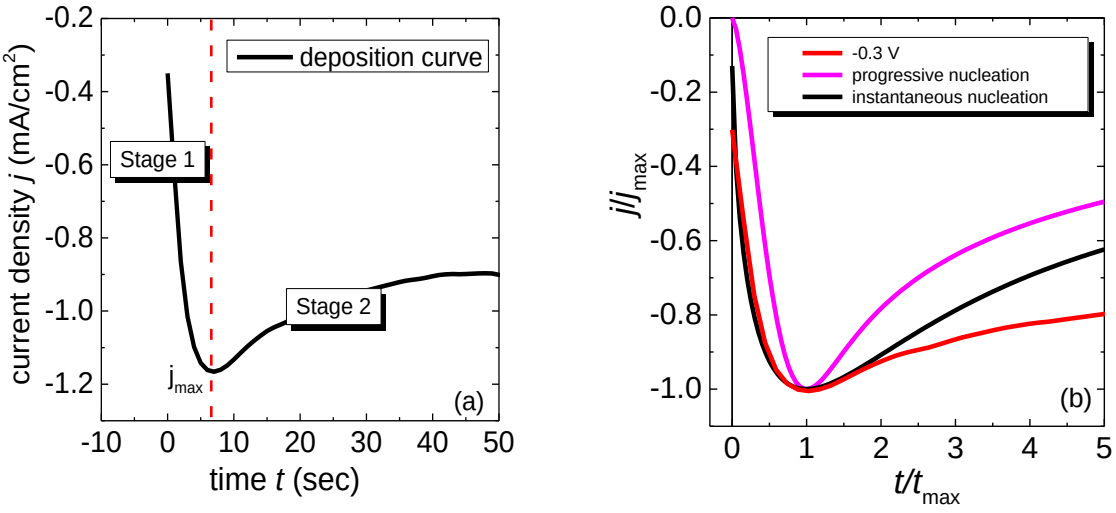

Figure 4.25: (a) The current transient plot of Ti/Au electrode, (b) the dimensionless quantity (j/j_{max}) versus (t/t_{max}) for E= -0.3V

For the Ti/Au electrode, also, the ECD of Cu_2O was performed at -0.3V, -0.4V, -0.5V, and -0.6V to study the over-potential effect on the morphology of the Cu_2O films, as shown in figure 4.26 (a). As the potential increased from -0.3V to more negative values, maximum current was reached almost instantaneously with the application of the potential and then the current decreased sharply.

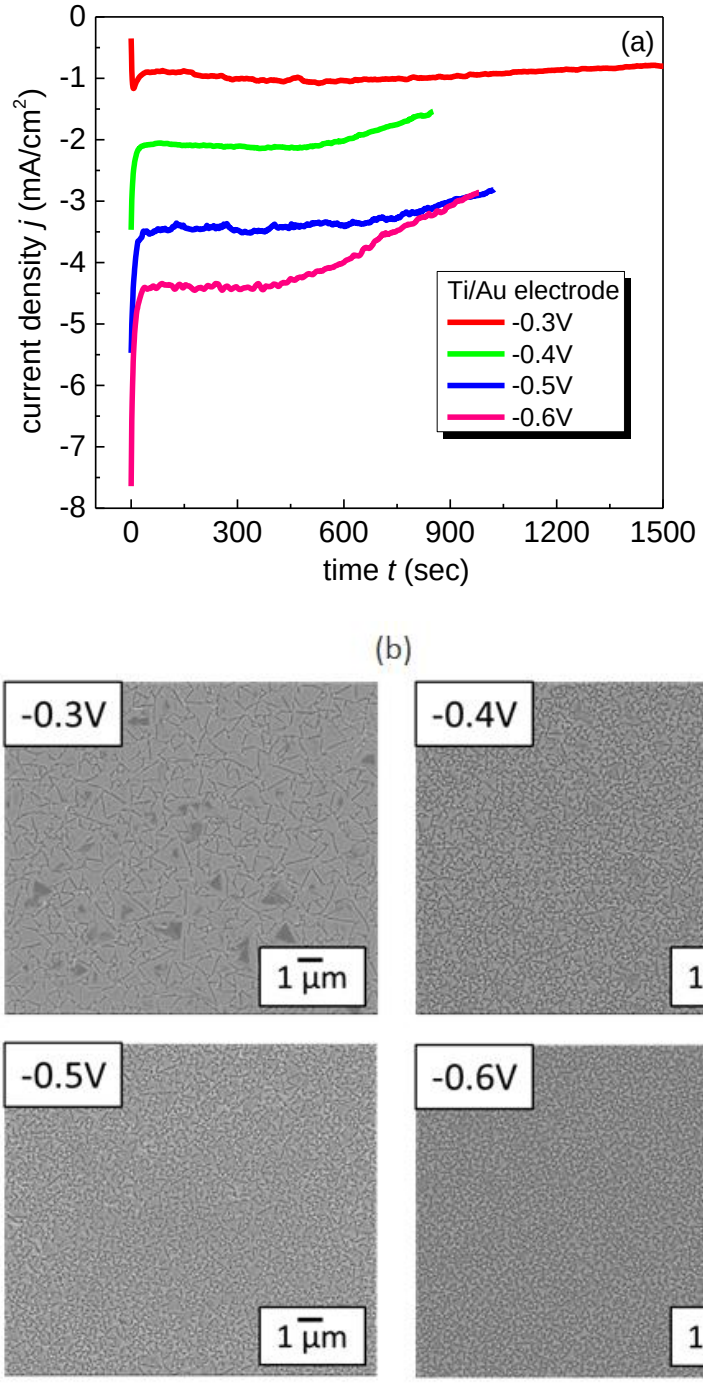

Figure 4.26: (a) The current transient plots for different over-potentials, (b) SEM images at -0.3V, -0.4V,-0.5V and -0.6 V for 2 µm thick Cu_2O film

The nucleation becomes denser for the high over-potential values, as was the case for the Cr/ITO electrode, which leads to smaller grain size with increasing potential. Figure 4.26 (b) shows the SEM images of Ti/Au electrode with the two microns thick Cu_2O deposited film at -0.3, -0.4V, -0.5V and -0.6V. For the solar cell fabrication, large grain size Cu_2O film is required which is obtained by using -0.3V. Hence, this potential was selected for the deposition of Cu_2O deposition on Ti/Au substrate as well as for the Ti/Ag electrode. Figure 4.25 shows the images of Ti/Au and Ti/Ag electrodes after the Cu_2O deposition.

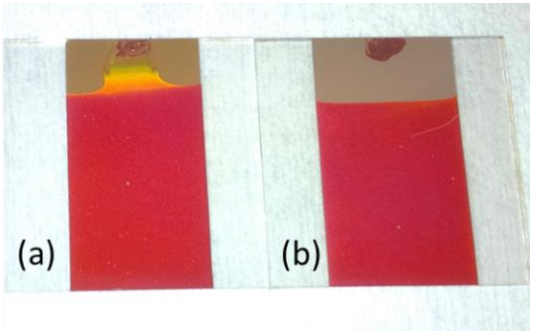

Figure 4.25: Images of conductive electrodes after Cu_2O electrodeposition i.e. (a) Ti/Au/Cu_2O, (b) Ti/Ag/Cu_2O

S-H model was used to determine the nucleation mechanism on the Ti/Au substrate for *E*=-0.3V. The experimentally obtained (j/j_{max}) and (t/t_{max}) for the Ti/Au electrode was plotted in figure 4.25 (b). The experimental current transient data follows the instantaneous nucleation model more closely for t/t_{max}< 2. For t/t_{max}> 2 the experimental current decreases slower as compared to the theoretical instantaneous nucleation curve.

The crystal structure of the Cu_2O deposits at -0.3 V was investigated by XRD. The obtained diffractogram is shown in figure 4.27, where the XRD peaks assigned to Au are marked with an asterisk (*). The electrodeposition of Cu_2O on Au (111) substrate promotes a highly (111) oriented Cu_2O film, whereas the peaks correspond to the (200) and (220) plane reflections are of extremely low intensity in this case. Due to the small lattice mismatch of ~4.2% between the Au (111) and the Cu_2O (111), the Au electrode promotes the growth of a highly (111)-textured absorber.

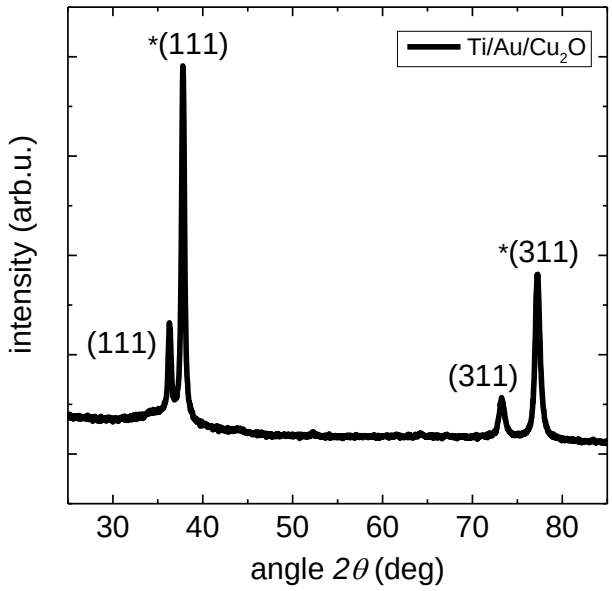

Figure 4.27: X-ray diffractogram of a Cu_2O film electrodeposited on Au electrode, where XRD peaks assigned to the Au are marked with an asterisk (*)

4.4 Choice of Cr/ITO electrode over other conductive electrodes for Cu_2O deposition

For the *substrate type* architecture, different electrodes were used which have shown different current-time transient responses during ECD, yielding different morphologies for the Cu_2O films. The main reason is the underlying electrical conductivities of the electrodes, as well as the texture of the electrode. A conductive electrode is of course required for the solar cell, but very high conductivity allows very high current densities even for a very low applied cathodic potential during the electrodeposition (as this was the case for Ti/Au electrode). This means that, in this case, the film's growth will be finally determined by how fast the mass is transported to the electrode. It is known, however, that mass-transport-controlled growth leads to poorly-defined grain shape and defect-rich deposits. So in order to obtain growth which is controlled by the charge transfer to the electrode but not by the mass-transport, a more substantial electrode resistance is of advantage. The Cr/ITO electrode fulfilled both these requirements as sheet resistance of the electrode is low enough to be used as a solar cell electrode and yet quite substantial to allow control over the current flow during the electrodeposition of Cu_2O. Figure 4.28 shows the SEM images of Cu_2O film morphology deposited on Ti/Au and Cr/ITO electrodes at their optimal Cu_2O deposition potentials. Low conductive Cr/ITO electrode promotes large grains of Cu_2O film as

compared to Ti/Au electrode and shows better solar cell performance, which we will see later when we discuss the characterization of solar cells.

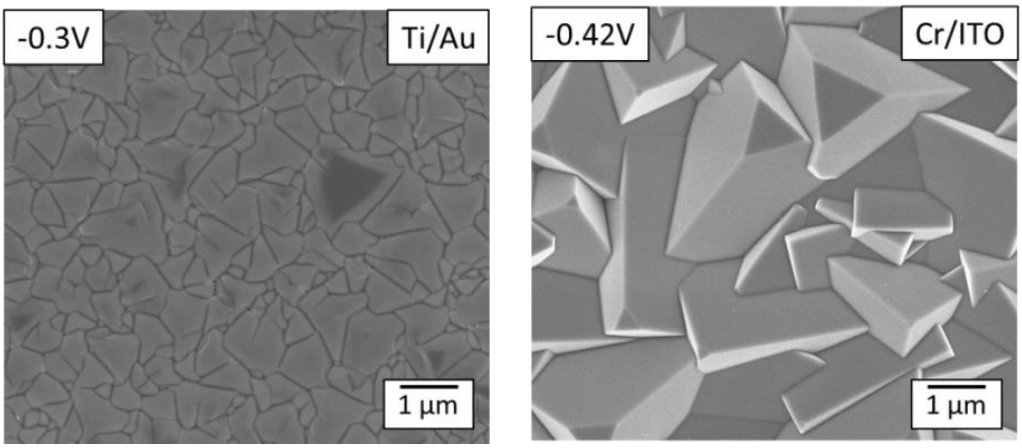

Figure 4.28: Plane view of Cu_2O films deposited at different electrodes during ECD

Chapter 5

Atomic Layer Deposition of $Zn_{1-x}Mg_xO$ layer

This chapter describes the investigation of the ZnMgO buffer layer, fabricated by atomic layer deposition and characterized with a variety of techniques in terms of its structural, optical and electronic properties. Special focus was given on the modification of the energy band structure of the material as a function of the Mg content, which is of critical importance for later implementation in a heterojunction solar cell with Cu_2O absorber.

5.1 ALD of ZnO

For the atomic layer deposition of the ZnO films, first the Zn precursor, i.e. DEZ, was introduced in-to the ALD reaction chamber, where it reacted with the clean substrate and then the chamber was purged with N_2 to remove the byproducts. Then, the second precursor, i.e. H_2O, was introduced, which reacted with the growing film and again the reaction chamber was purged with the N_2 gas. The DEZ-H_2O alteration constitutes one cycle of ALD. The overall chemical reaction between DEZ and H_2O can be expressed as:

$$Zn\ (C_2H_5)_2^* + H_2O(g) \rightarrow ZnO^* + 2C_2H_6(g)$$

where $*$ denotes the surface adhering species. The growth rate per cycle (GPC) was determined through the linear fittings of the ZnO layer thickness as a function of the number of ALD cycles, as shown in figure 5.1. The extracted GPC is 0.140 nm/cycle.

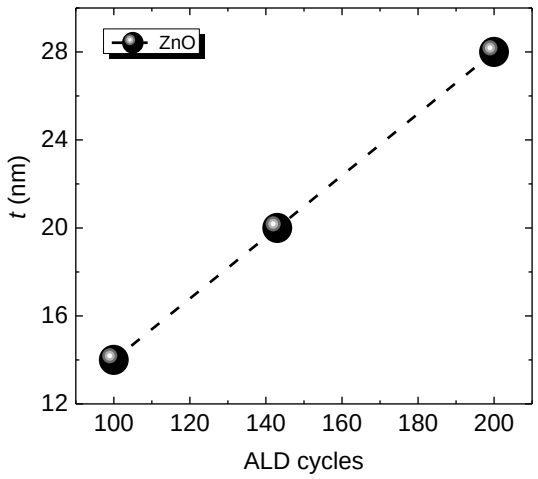

Figure 5.1: Linear dependence of the ZnO thickness (t) as a function of the number of ALD cycles at 150°C deposition temperature

In ALD, the deposition temperature plays an important role in determining the electrical properties of the thin-films, as it affects the precursor's reactivity with the substrate's surface, which further affects the stoichiometry of the deposited films [99] [167], [168]. ZnO layers were fabricated in the temperature range of 100°C-200°C. The deposited layers showed increase in resistivity with decreasing deposition temperature. The layers deposited at 200°C exhibited lower resistivity, in the order of 10^{-2} Ohm cm, as compared to the films deposited at 150°C. This can be attributed to the suppression of the intrinsic donor defects (oxygen vacancies or zinc interstitials) at low temperatures, which reduces the intrinsic n-type carrier concentration of ZnO films [99]. In the literature, also, it was reported that the conductivity of ZnO layers can decrease by up to three orders of magnitude as the deposition temperature is lowered from 200°C to 100 °C [168], [169]. For the solar cell fabrication, 150°C deposition temperature was selected for the ZnO layer (with a reported carrier concentration of ~10^{18}-10^{19}/cm^3 [170]).

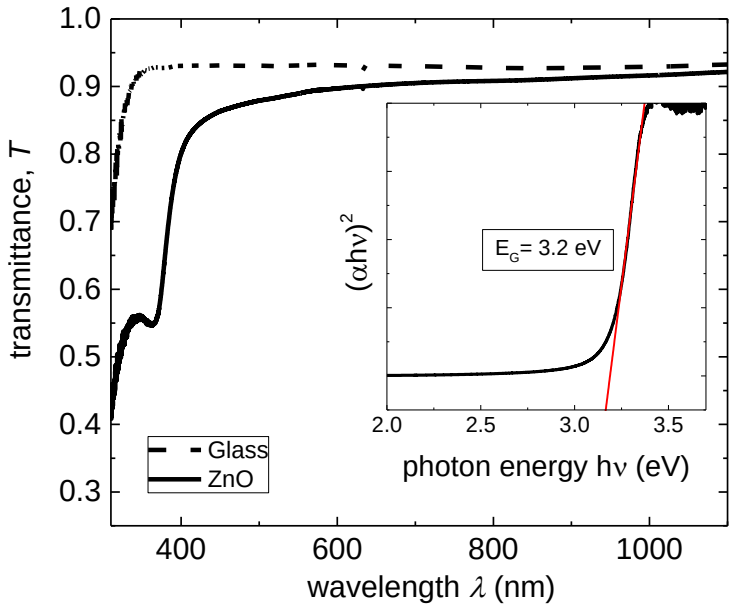

Figure 5.2: Transmittance of glass and ZnO film as measured by FTIR, (inset graph) determination of optical band gap from the tauc plot

The optical transmittance of the ZnO layer was measured with FTIR. The transmittance spectra of plain glass and of the glass coated with ZnO layer are shown in figure 5.2. The 20 nm thick layer is transparent in the visible region. The measured transmittance is >85%. The band gap value, E_G, was extracted by using the Tauc plot method, based on the relation: $(\alpha h\nu)^n = A(h\nu - E_G)$, where the exponent n has the value 2 for direct bandgap semiconductors. The bandgap value was extracted from the *hv*-axis intercept of the data fit

to the Tauc relation for photon energies above the bandgap (inset of figure 5.2). The linear fit yields a band gap of 3.2 eV. For the solar cell fabrication, after the ECD of *p*-Cu_2O films on the Cr/ITO electrode, the samples were transfered to the ALD chamber for the deposition of the ZnO n-layer, with a thickness of 20 nm.

5.2 ALD of $Zn_{1-x}Mg_xO$

In order to dope ZnO films with Mg, first we needed the GPC of MgO. For this, MgO layers were grown by ALD at 150°C. For the MgO thin-films, the deposition procedure was the similar to that of the ZnO layers. First, the Mg precursor, i.e. bis-(ethylcyclopentadienyl)-magnesium ($(CpEt)_2Mg$), was introduced in to the reaction chamber and then the chamber was purged with N_2 gas. Then, H_2O was introduced which reacted with the growing film and again the reaction chamber was purged with the N_2 gas to remove the byproducts of the reaction. During the deposition, the H_2O precursor was at room temperature, whereas the Mg precursor was kept at 85°C. The GPC of MgO was determined to have a value of 0.12 nm/cycle, through the linear thickness dependence on the ALD cycles, as shown in figure 5.3.

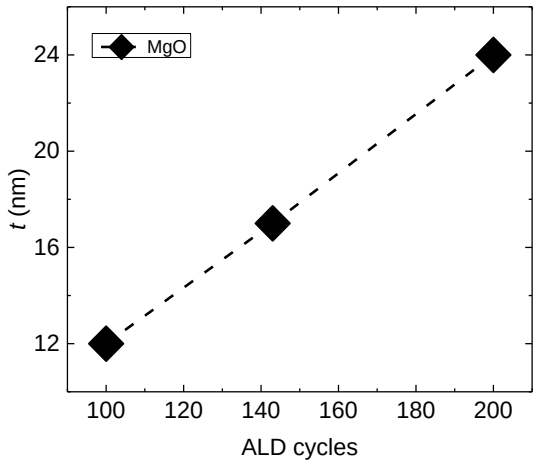

Figure 5.3: Linear dependence of MgO thickness (t) as a function of the number of ALD cycles at 150°C deposition temperature

The Mg concentration, *x*, in the $Zn_{1-x}Mg_xO$ layers was controlled by varying the number of MgO cycles during ALD, according to the expression [92]:

$$x_{GPC} = \frac{GPC_{MgO}}{GPC_{MgO} + (n.GPC_{ZnO})}$$

where x_{GPC} is the Mg concentration, n is the number of ZnO cycles, GPC_{MgO} = 0.120 nm/cycle, GPC_{ZnO} = 0.140 nm/cycle. Films with varying Mg concentrations were prepared. Table 5.1 shows the Mg concentration, i.e. x_{GPC}, in the film, as extracted from the above expression.

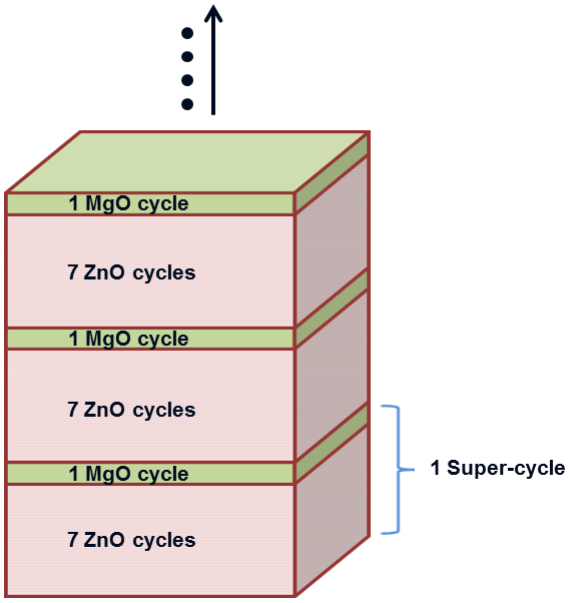

Figure 5.4: Schematic diagram of the Mg doped ZnO film stack used in ALD for the 7:1 ratio. 8 cycles define the so-called "super-cycle"

As an example, the ratio 7:1 stands for seven cycles of ZnO, followed by one cycle of MgO. The total of 8 cycles defines the so-called "super-cycle". The number of super-cycles was repeated n times to obtain the required film thickness as schematized in figure 5.4. In the same way, films with ratios 1:1, 3:1, 5:1, 7:1, 11:1 were prepared. Pure MgO and ZnO films were also prepared as references.

Table 5.1: The ZnO:MgO cycles and their corresponding super-cycles for 20 nm thick films together with the Mg concentration in each film

ZnO:MgO cycles	Super-cycles	x_{GPC}
ZnO : 0	0	0
11 : 1	12	0.072
7 : 1	18	0.109
5 : 1	25	0.146
3 : 1	37	0.222
1 : 1	78	0.461
0 : MgO	0	1

5.2.1 Analysis of Mg incorporation

To analyze the incorporation of Mg in the ZnO lattice and to precisely define the atomic concentration of Mg in the ZnO films, the chemical binding energy of Zn and Mg in $Zn_{1-x}Mg_xO$ films was analyzed by XPS. The measurements were performed in an ultra-high vacuum chamber and Al Kα was used as X-ray source. All the XPS measurements were performed by first taking a survey scan and then by high resolution scans were performed on the desired individual peaks. In addition, the binding energy scale of the spectrum was calibrated by the carbon C1s peak, in order to insure the accuracy of the measurements.

ZnO films with different Mg content were analyzed by XPS. First, the surface scans of all the samples were performed to resolve the peaks of the elements present on the specimens' surfaces. The surface scan data for the ZnO and MgO samples are shown in figure 5.5, featuring the core level peaks along with the ones of oxygen (O1s)and carbon (C1s) main peaks. For the ZnO layer, the Zn 2p core level exhibits two peaks corresponding to the spin-orbit doublet Zn $2p_{1/2}$ (1045.13 eV) and $Zn2p_{3/2}$ (1022.07 eV). The higher resolution scan of the doublet is shown in the inset graph of figure 5.5 (a).

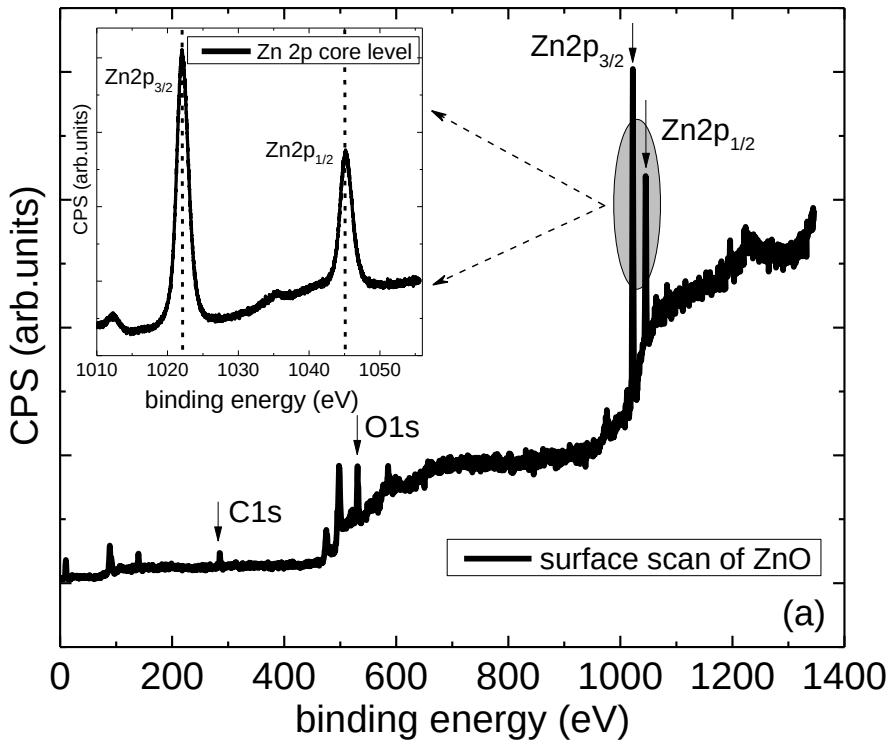

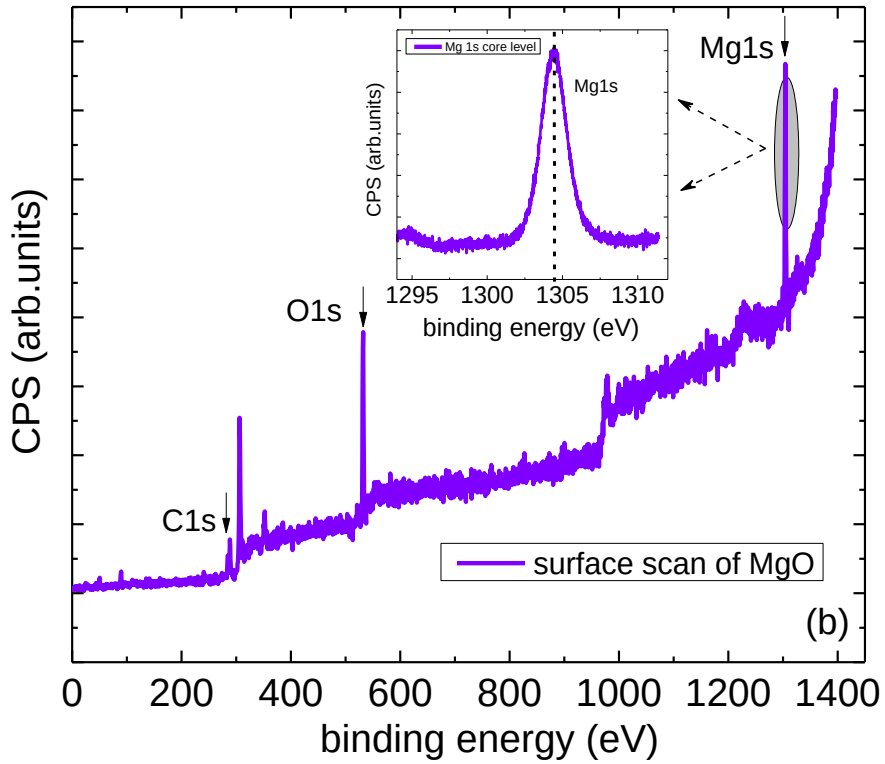

Figure 5.5: The surface scan data of (a) ZnO and (b) MgO together with main peaks O1s, Mg1s and core levels peaks whereas inset graphs show the high resolution scans of Zn2p and Mg 1s peaks

These binding energies correspond to those of XPS core levels of the matrix elements of the ZnO wurtzite structure [171], metallic Zn, with a binding energy of 1021.7 eV [171], was not observed, which confirms that Zn appears only in the Zn^{2+} oxidation state within the XPS detection limit of ~10^{19} atoms/cm^3.

On the other hand, the Mg1s core level, measured for the MgO film, exhibits one intense peak at 1304.40 eV, as shown in figure 5.5 (b) and no metallic Mg peak (1303 eV) [171] was observed. The Zn2p and Mg1s core level peak positions as a function of x in $Zn_{1-x}Mg_xO$ films are shown in figure 5.6.

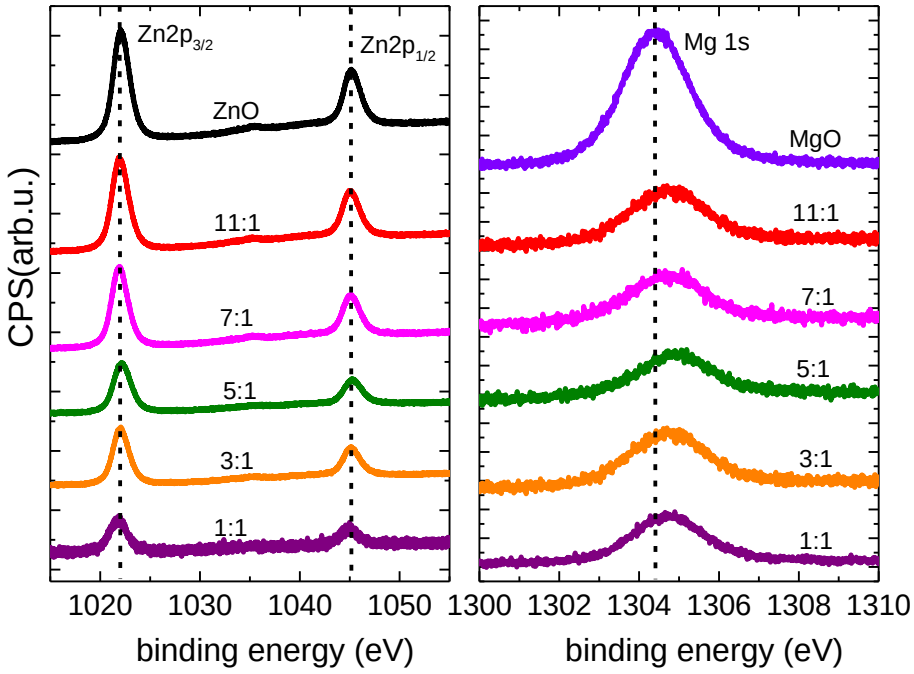

Figure 5.6: The Zn2p and Mg1s core level peaks with varying Mg concentration

ZnO has the wurtzite crystal structure, while MgO has a cubic structure. The incorporation of Mg into the ZnO films modifies the atomic configuration and also tunes the electronic structure. In the case of the hexagonal, wurtzite ZnO unit cell, there are two tetrahedrally-coordinated Zn atoms, whereas there are four octahedrally coordinated Mg atoms in the cubic MgO unit cell. The net charge transfer from the cation to the anion depends on the cation coordination number, with a higher transfer degree for the tetrahedral than for the octahedral coordination [172]. The XPS spectra (figure 5.6) showed a considerable shift of the Mg 1s peak to higher binding energy values (~350–400 meV) for $Zn_{1-x}Mg_xO$ compared to MgO, whereas a much less significant shift was observed to lower binding energies for the Zn doublet peak (~100 meV) for $Zn_{1-x}Mg_xO$ compared to ZnO. This suggests the substitutional incorporation of Mg into the ZnO lattice, with the corresponding change of the Mg coordination number from octahedral to tetrahedral. Further, the low electron negativity of Mg (1.31) as compared to Zn (1.65) alters the potential of core electrons due to screening effects. This also results in a higher binding energy shift of the Mg1s core level peak. As the coordination of Zn does not change, the shift of the Zn 2p core level is due to the nearest neighbor effect only and therefore less significant. These results agree with the findings of Achary et al. [172] for Mg-doped ZnO films.

5.2.2 Determination of Mg concentration

The position of the $Zn2p_{3/2}$ and Mg1s peaks for the investigated samples with varying x, is presented in Table 5.2. The area under these peaks is related to the concentration of each element. The Mg concentration in the ZnO films is therefore extracted from the core level peak areas by using eq. (19). Firstly, the peak areas of the individual peaks Mg1s, $Zn2p_{1/2}$ and $Zn2p_{3/2}$ were divided to the respective relative sensitive factors (RSF), which are 11.16, 9.79, and 18.91 [173]. The ratio of the corrected peak areas Mg/(Mg+Zn) yields the Mg atomic concentration of the films. The Mg concentration values extracted from the XPS (x_{XPS}) and calculated from the GPC (x_{GPC}), are presented in Table 5.2. As the number of MgO cycles increases during ALD, a greater the discrepancy is marked between the calculated and the XPS-extracted Mg concentration values. Particularly, for the 3:1 and 1:1 ratios, the Mg content extracted from the GPC is significantly higher than the one extracted from the XPS spectra. The XPS-derived Mg concentration will be used for the rest of the thesis.

Table 5.2: The Mg concentration as calculated from the GPC (x_{GPC}) and from the XPS measurements (x_{XPS}). The binding energies of the $Zn2p_{3/2}$ ($E_{Zn2p\ 3/2}$) and Mg1s (E_{Mg1s}) peaks for each films are also shown

ZnO:MgO cycles	x_{GPC}	x_{XPS}	$E_{Zn2p_{3/2}}$ (eV)	E_{Mg1s} (eV)
ZnO : 0	0	0	1022.1	-
11 : 1	0.072	0.088	1022.01	1304.84
7 : 1	0.109	0.107	1021.94	1304.69
5 : 1	0.146	0.140	1022.06	1304.73
3 : 1	0.222	0.163	1022.05	1304.70
1 : 1	0.461	0.333	1021.89	1304.80
0 : MgO	1	1	-	1304.40

5.2.3 Valence band position in $Zn_{1-x}Mg_xO$ layers

Further, the valence band maximum positions of the $Zn_{1-x}Mg_xO$ films were extracted from the spectra, such as the one in figure 5.7 (a), which presents peaks at 10.4, 7.4 and 4.5 eV. The peak at 10.4 eV is attributed to the Zn 3d band, the peak at 7.4 eV presents the O-2p orbitals hybridized with Zn 4s and 4p ones, while the peak at 4.5 eV is attributed to the O-2p orbitals [174]. The position of the VBM is extracted by taking a linear extrapolation of the valence band emission, as described by Kraut et al. [146]. The valence band spectrum obtained for x = 0.107 is shown in figure 5.7 (a), whereas figure 5.7 (b) shows the VBM positions for x = 0 to x = 0.163 which is determined by the linear extrapolation of the leading

edges of the spectra to the base line. As the Mg content increases, the VBM position of $Zn_{1-x}Mg_xO$ films shifts down as compared to ZnO.

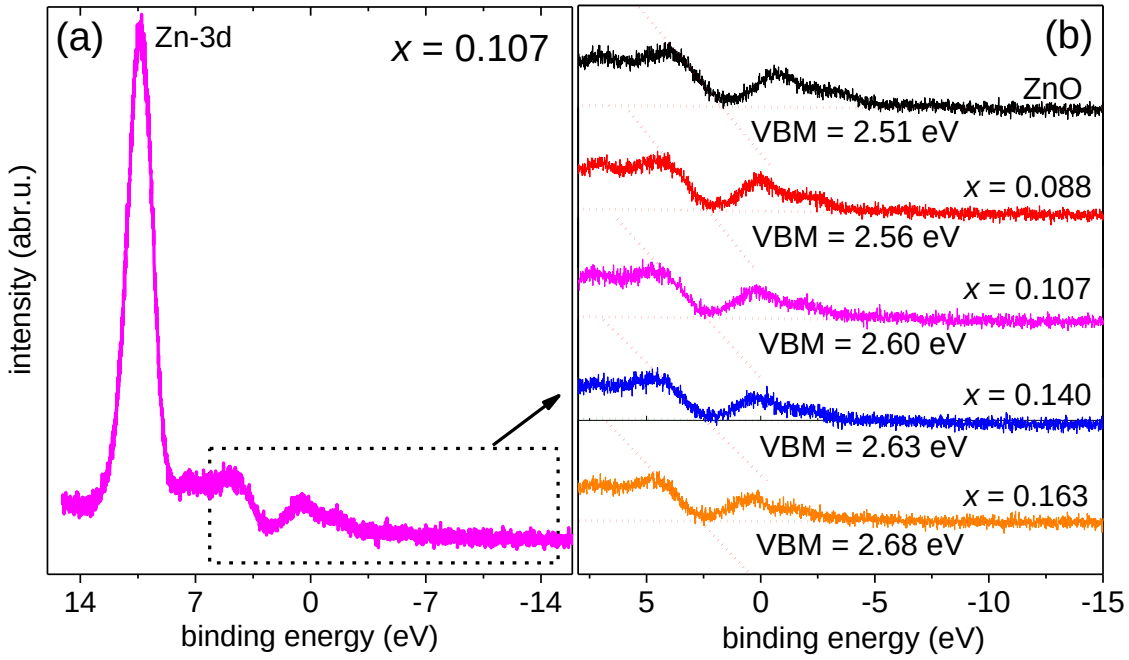

Figure 5.7: (a) XPS spectrum for the determination of the VBM for a film with x = 0.107 (b) Zoom-in the region of the spectra used for the VBM determination, through the linear extrapolation of the leading edges to the base line

5.2.4 Optical and structural properties of $Zn_{1-x}Mg_xO$ layers

The optical transmittance spectra of 20 nm-thick and 100 nm-thick $Zn_{1-x}Mg_xO$ films were measured and analyzed. Figure 5.8 (a) shows the transmittance spectra of 20 nm-thick films for various Mg concentrations. The films are highly transparent and the transmittance increases with x due to the widening of the optical band gap. The E_G values were extracted from Tauc plots as shown in figure 5.8 (b). The transmittance spectra of 100 nm-thick films for various Mg concentrations are shown in figure 5.8 (c) and the E_G values extracted from Tauc plots are shown in figure 5.8 (d).

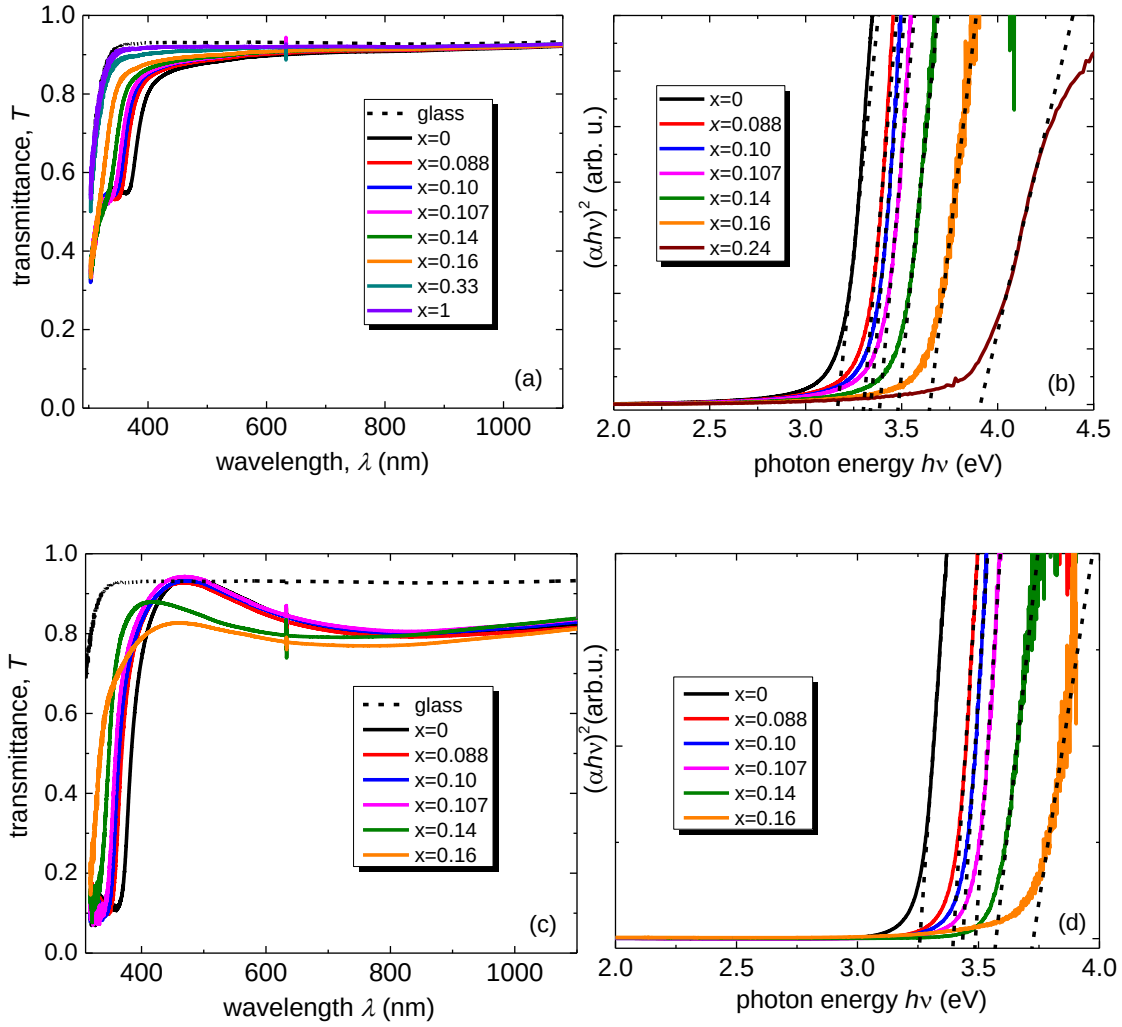

Figure 5.8: (a) Transmittance spectra of 20 nm-thick $Zn_{1-x}Mg_xO$ films with different Mg concentrations, (b) Tauc plots for the extraction of the optical bandgap values of doped films, (c) Transmittance spectra of 100 nm-thick $Zn_{1-x}Mg_xO$ films with different Mg concentrations, (d) Tauc plots for the extraction of the optical bandgap values of doped films

Table 5.3 shows the band gaps obtained for 20 and 100 nm thick $Zn_{1-x}Mg_xO$ with varying x. Furthermore, the E_G values are plotted as a function of x for both 20 and 100 nm-thick films and a linear fit yields: E_G=3.19+2.35*x* eV (figure 5.9).

The observed linear dependence of the bandgap on *x* agrees with the literature reports for films prepared by a variety of techniques [109], [175]–[177]. The bandgap increase in $Zn_{1-x}Mg_xO$ is related to the modification of the valence and conduction band structure. In ZnO, the top of the valence band is dominated by the coupling of anion p with cation p and semicore d orbitals, whereas the bottom of the conduction band mostly forms from cation s states [177]–[179].

Table 5.3: Band gaps for the 20 and 100 nm thick $Zn_{1-x}Mg_xO$

$Zn_{1-x}Mg_xO$	E_G(eV) (20 nm)	E_G(eV) (100 nm)
x = 0	3.17	3.24
x = 0.088	3.3	3.39
x = 0.107	3.35	3.44
x = 0.140	3.47	3.56
x = 0.163	3.63	3.71
x = 0.33	3,9	-

Because of the weak p-d coupling strength resulting from the absence of Mg 3d electrons, the VBM position in $Zn_{1-x}Mg_xO$ is shifted downwards with respect to that of un-doped ZnO (figure 5.7(b)). On the other hand, the Zn 4s state in the conduction band decreases with increasing the Mg content, which shifts the bottom of the conduction band upwards [180].

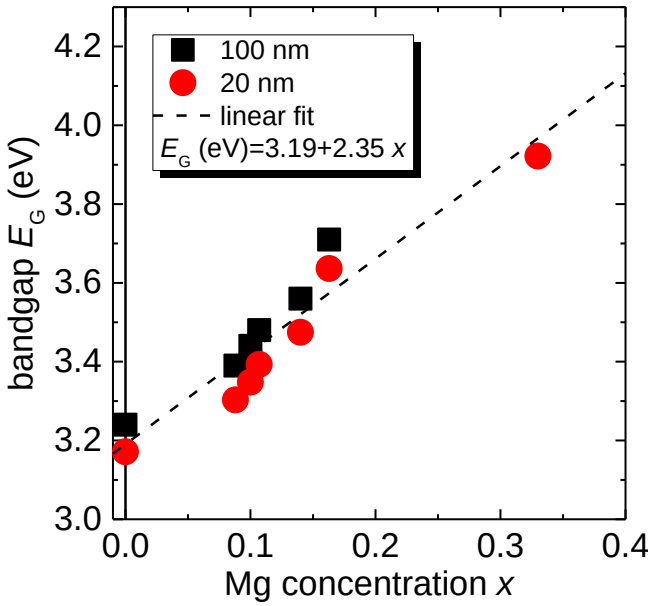

Figure 5.9: The bandgap of ZnO:Mg as a function of the Mg concentration with values extracted for the 20 and 100 nm-thick films

If the amount of Mg incorporated into the ZnO crystal is excessively large, the structure is transformed from the wurtzite to the cubic one [109], [110]. Figure 5.10 shows the band gap dependence on the Mg content from 0% to 100% taken from the literature [111].

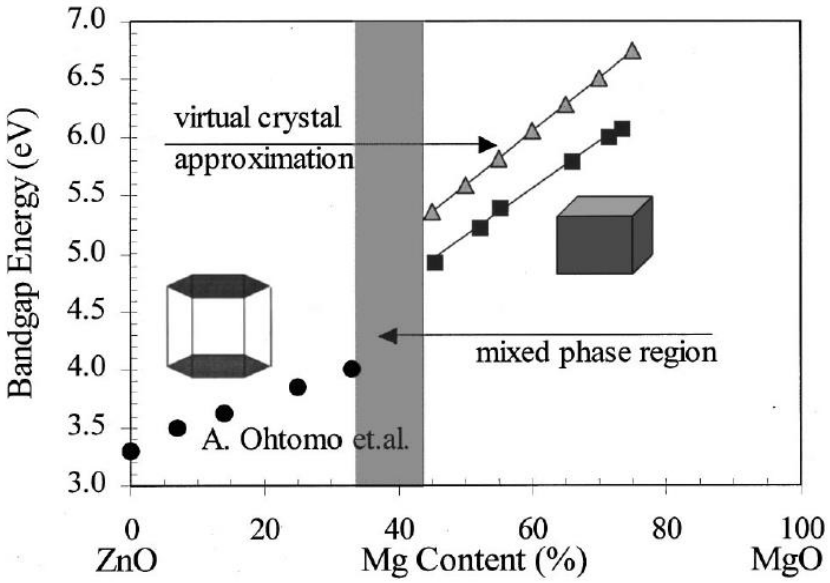

Figure 5.10: Band-gap variation of ZnO:Mg as a function of Mg content [111]

According to the phase diagram, the MgO-ZnO binary system includes less than 4 at% of Mg [111]. However, the experimental solid solubility limit of MgO into ZnO by PLD as reported by Ohtomo et.al. [109], is 0.33. For x < 0.33, single phase wurtzite structure with linear increase of band gap is exhibited and for x > 0.33 to x < 0.43 a mixed state without definite trend in band gap evolution is found. For still higher Mg doping, a cubic phase is dominant in the films (figure 5.10). The solubility limit depends on the type of fabrication method, substrate, and the temperature during deposition. Due to the layer-by-layer growth, the Mg solubility in ALD films is comparable to that of PLD or sputtering.

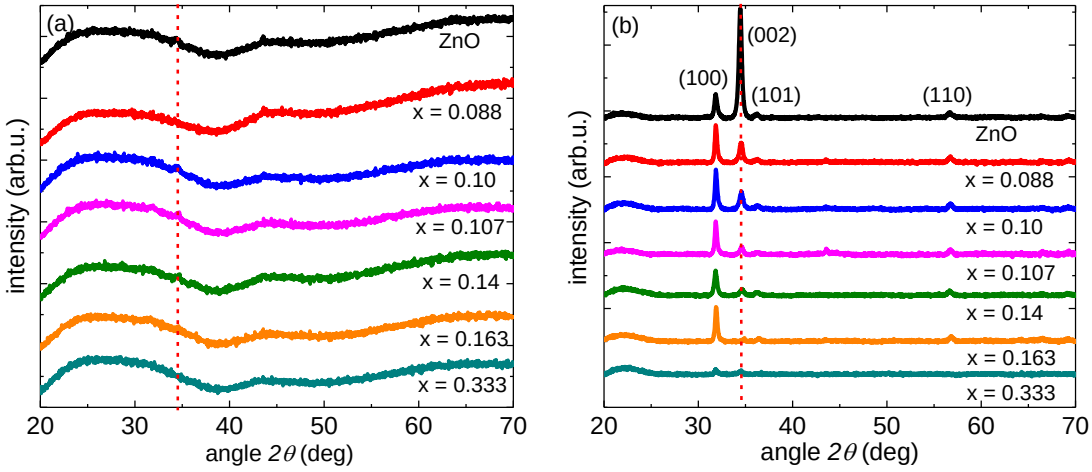

Figure 5.11: XRD measurements of (a) 20nm-thick and (b) 100nm-thick $Zn_{1-x}Mg_xO$ films for varying Mg concentration

The structural properties of the ALD-grown $Zn_{1-x}Mg_xO$ films were investigated by XRD. The XRD spectra of pure ZnO, pure MgO along with varying x doping are displayed in figure 5.11. Figure 5.11 (a) shows that the diffractograms of the 20 nm-thick films. These reveal only an extremely weak ZnO (002) peak for $x \leq 0.107$. The films are therefore amorphous/ nanocrystalline, with the onset of crystallization being visible for low Mg content. On the other hand, the 100 nm-thick films show well-defined ZnO peaks (figure 5.11 (b)). The un-doped ZnO has a strong (002) texture, a weaker peak stems from the (100) plane reflection and finally the (110) and (101) peaks are also visible. For all Mg-containing films, the (100) texture dominates, while the (002) peak becomes gradually weaker, until it almost disappears for $x \geq 0.163$.

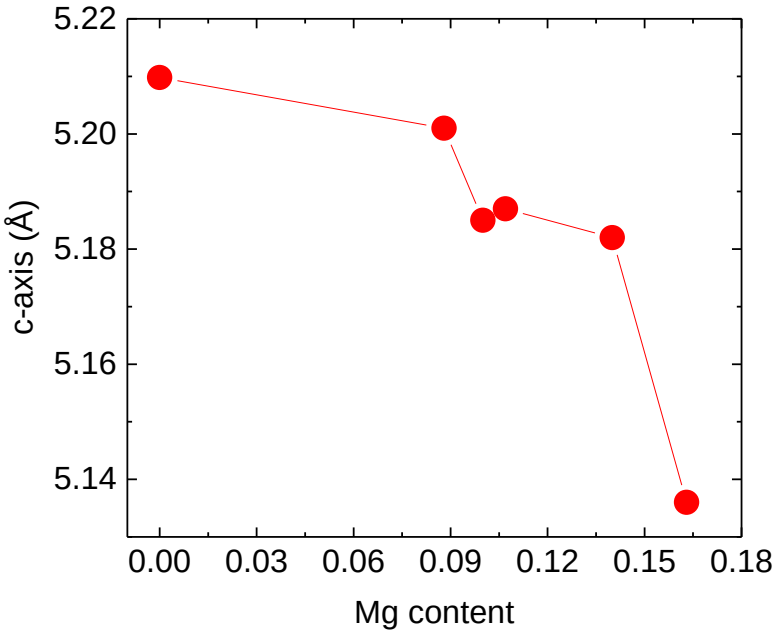

Figure 5.12: c-axis lattice constant of $Zn_{1-x}Mg_xO$ for x = 0 to x = 0.163

The (110) and (101) peaks are not significantly modified for $x \leq 0.163$. Compared to the un-doped ZnO, the Mg-doped films are less crystalline, as demonstrated from the comparison of the intensities of the main peaks. From the inter-planar distance (d-values), the c-axis lattice parameters of the hexagonal $Zn_{1-x}Mg_xO$ were determined for the (002) planes, by using the relation:

$$\frac{1}{d^2} = \frac{4}{3}\left(\frac{h^2 + hk + k^2}{a^2}\right) + \frac{l^2}{c^2}$$

We observe a decrease in the c-axis lattice parameter from 5.210 Å for ZnO to 5.136 Å for x = 0.163 as shown in figure 5.12. This decrease indicates the substitutional incorporation of the smaller ionic radius Mg^{2+} (0.57Å) into Zn^{2+} (0.60Å) sites, which results in the gradual shrinkage of the c-axis lattice constant.

Chapter 6

The $Cu_2O/Zn_{1-x}Mg_xO$ heterojunction & Solar cell characterization

This chapter describes the investigation of the $Cu_2O/Zn_{1-x}Mg_xO$ heterojunction and the evaluation of the photovoltaic performance of the solar cells. The chemical and electronic state of the heterojunction is meticulously analyzed by XPS, in an effort to demonstrate the influence of the Mg doping on the energy band alignment at the p/n interface. Then these results are correlated with the PV performance of the solar cells.

6.1 The ECD-Cu_2O/ALD-$Zn_{1-x}Mg_xO$ interface

6.1.1 Chemical state of Cu_2O surface

The surface of the ECD-Cu_2O film was characterized by XPS measurements before and after the ALD of the n-layer. The latter had a thickness of 3 nm. The obtained XPS spectrum (figure 6.1 (a)) before the ALD shows the presence of a thin CuO layer, which is formed due to the absorber exposure to air. This layer can adversely affect the solar cell device efficiency by promoting interface recombination [43]. In the XPS analysis, the bulk Cu_2O film exhibits two main peaks at 932.53 eV and at 952.4 eV, corresponding to the $2p_{3/2}$ and $2p_{1/2}$ levels of the Cu^{1+} state (Cu_2O). The peak obtained at 934.2 eV is attributed to Cu^{+2} (CuO). The broad satellite peaks near 940 eV to 944 eV originate from the CuO phase, which is a characteristic of materials having a d^9 configuration in the ground state [44]. Hence, the existence of the satellite peaks is an evidence of CuO presence in addition to the peak assigned to the Cu^{2+} state at 934.2 eV.

When a ZnO layer is deposited by ALD on the top of the absorber, the CuO surface layer is reduced, as shown in figure 6.1 (a) (blue color). No satellite peaks or the shoulder peaks at 934.2 eV are observed in this case. The reduction of the CuO layer is attributed to the DEZ ALD precursor that is, used for the ZnO deposition. A similar reduction behavior of CuO to Cu_2O by DEZ has been reported by Lee et al [46] and Hoye et al. [60]. We can therefore conclude that the heterojunction interface is free from foreign phases that could promote interface recombination.

The positions of the core level peaks for the bare Cu_2O absorber do not change when the ZnO layer is deposited atop (Figure 6.1 (a)). In addition to the core level peaks, XPS measurements were also conducted to extract the VBM for the Cu_2O (Figure 6.1(b)). By applying the same linear extrapolation method of the leading edge to the baseline as we did in previous chapter for the $Zn_{1-x}Mg_xO$, a VBM = 0.02eV was obtained.

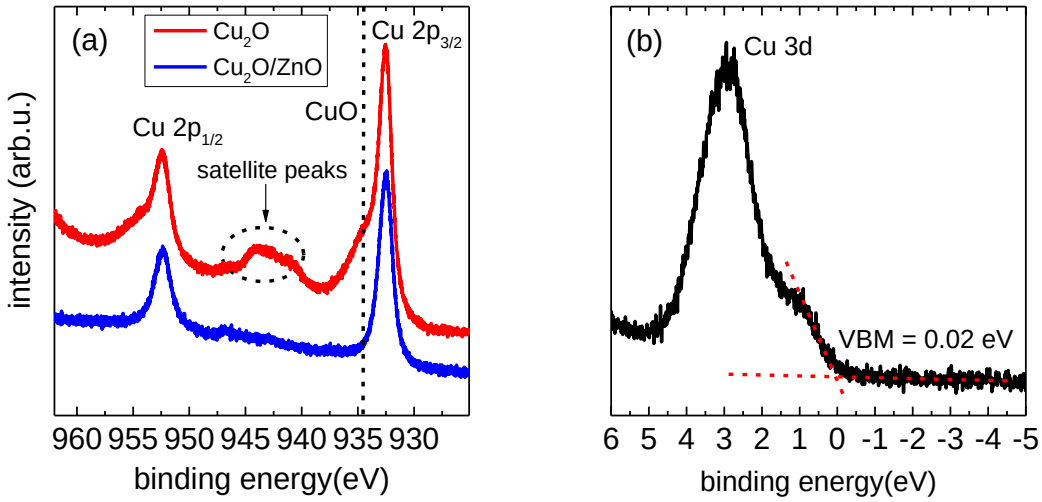

Figure 6.1: (a) XPS spectra of the $Cu2p_{3/2}$ and $Cu2p_{1/2}$ core level for as deposited Cu_2O (red) and Cu_2O capped by 3 nm ALD ZnO (blue), (b) VBM extracted for Cu_2O through the linear extrapolation of the leading edge to the base line

6.1.2 Determination of band offset values at the hetero-junction

The discontinuities of the valence-band and the conduction-band edges at the interface represent "band offsets", which can limit the solar cell performance. These offset values i.e. valence band (ΔE_{VBO}) and conduction band (ΔE_{CBO}) offset can be determined experimentally from the following relations [146]:

$$\Delta E_{VBO} = [\Delta E_{CL}^{HET} + (E_{Zn2p_{3/2}}^{Zn_{1-x}Mg_xO} - E_{VBM}^{Zn_{1-x}Mg_xO}) - (E_{Cu2p_{3/2}}^{Cu_2O} - E_{VBM}^{Cu_2O})]$$

$$\Delta E_{CBO} = \Delta E_{VBO} + (E_G^{Zn_{1-x}Mg_xO} - E_G^{Cu_2O})$$

where $\Delta E_{CL}^{HET} = \left(E_{Zn2p_{3/2}}^{HET} - E_{Cu2p_{3/2}}^{HET}\right)$ is the energy separation between $Zn2p_{3/2}$ and $Cu2p_{3/2}$ core levels for the heterojunction, $\left(E_{Zn2p_{3/2}}^{Zn_{1-x}Mg_xO} - E_{VBM}^{Zn_{1-x}Mg_xO}\right)$ and $(E_{Cu2p_{3/2}}^{Cu_2O} - E_{VBM}^{Cu_2O})$ are the VBM energies with reference to the core level peaks in $Zn_{1-x}Mg_xO$ and Cu_2O, respectively. The core level peaks for the heterojunction are practically at the same positions as for the pure materials (within the accuracy of the XPS measurements). Due to this, the ΔE_{VBO} and

ΔE_{CBO} can be extracted from the VBM values and the bandgaps of the $Zn_{1-x}Mg_xO$ and the Cu_2O. The band gap of Cu_2O is 1.93 eV. The calculated band offsets values for the $Cu_2O/Zn_{1-x}Mg_xO$ hetero-junction for the different Mg concentrations values are shown in Table 6.1.

Table 6.1: The calculated valence and conduction band offsets for the $Cu_2O/Zn_{1-x}Mg_xO$ heterojunction for the different Mg concentrations

$Cu_2O/ Zn_{1-x}Mg_xO$	VBM (eV)	ΔE_{VBO}(eV)	ΔE_{CBO}(eV)
x = 0	2.51	2.49	1.22
x = 0.088	2.56	2.54	1.16
x = 0.107	2.60	2.58	1.10
x = 0.140	2.63	2.61	1.05
x = 0.163	2.68	2.66	0.94

A type II $Cu_2O/ Zn_{1-x}Mg_xO$ hetero-junction (staggered gap) is formed in every case (Figure 6.2). The band offset values of the Cu_2O hetero-junction with un-doped and doped ZnO have been studied in the literature. VBO values from 1.7 eV to 2.8 eV and CBO values from 1.0 eV to 1.47 eV were reported [113], [126], [181], [182]. The calculated band offset values in this work lie within the reported ranges. As the conduction band minimum moves upwards with the Mg concentration, we anticipate a corresponding increase of the open circuit voltage and decrease of the carrier recombination in solar cells.

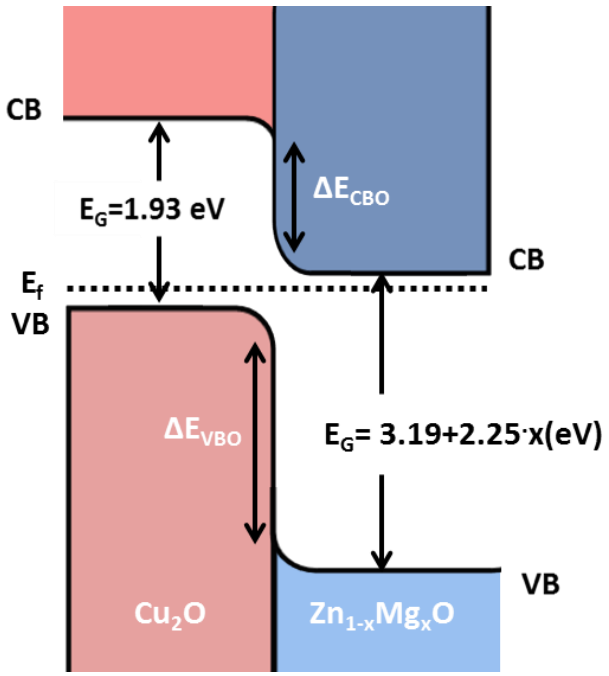

Figure 6.2: Schematic energy band diagram of the $Cu_2O/Zn_{1-x}Mg_xO$ type II hetero-junction

6.2 Electrical characterization of ECD-Cu_2O/ALD-$Zn_{1-x}Mg_xO$ hetero-junction solar cells as function of Mg concentration

The appropriate band alignment and the lattice match at the hetero-junction of absorber and buffer layer is of paramount importance to achieve efficient solar cell performance. The non-ideal band alignment at the hetero-junctions cause additional energy barriers for the charge carriers, thus, reduces the charge collection whereas the lattice mismatch leads to high density of the interface states which act as trapping centers, thereby influence the potential distribution across the interface. These two limiting feature of the hetero-junction promotes high recombination current via interface-traps states which decreases the overall solar cell performance. Therefore, the hetero-interface between absorber and buffer layer should be carefully selected in order to improve the PV performance [20]. The band offset values i.e. ΔE_C and ΔE_V at the hetero-junction of Cu_2O and un-doped ZnO were obtained by XPS as 1.22 eV and 2.49 eV, respectively (see table 6.1). However, the lattice mismatch of 27.1% [183] is reported between the two which leads to high interface defect states.

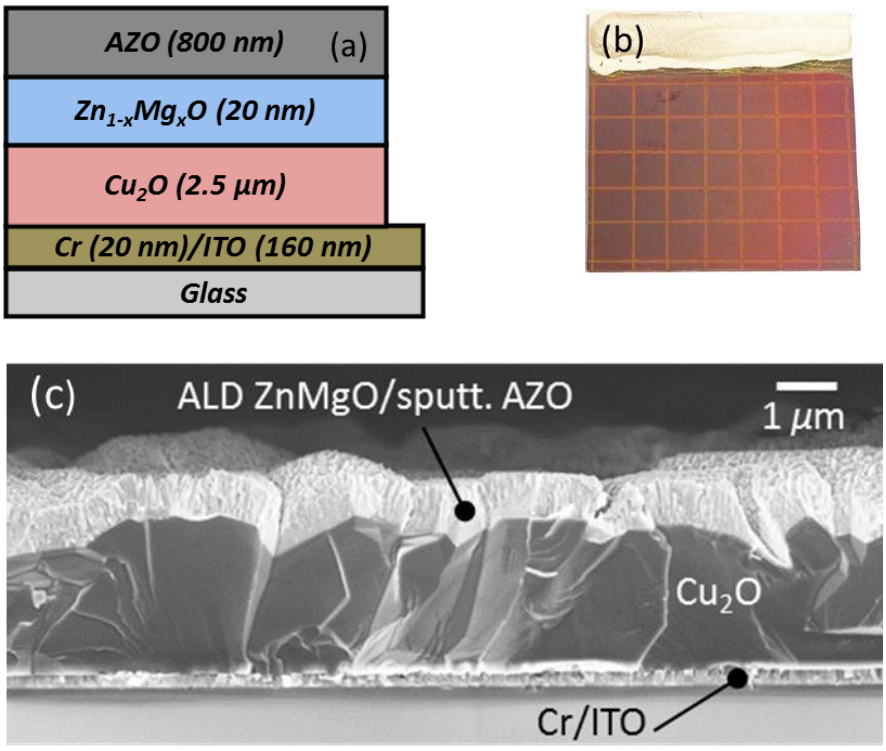

Figure 6.3: (a) Schematic of $Cu_2O/Zn_{1-x}Mg_xO$ solar cell, (b) image of the solar cell and (c) cross section SEM image of the cell

The IV performance of the $Cu_2O/Zn_{1-x}Mg_xO$ hetero-junction solar cells and the charge transport mechanism were investigated using the current-density-voltage (j-V)

characterizations. Figure 6.3 (a, b and c) illustrates the schematic of $Cu_2O/Zn_{1-x}Mg_xO$ hetero-junction solar cell, image of solar cell where the grid lines indicate the solar cell areas and the SEM cross section image, respectively. Several $Cu_2O/Zn_{1-x}Mg_xO$ solar cells with varying x = 0 to x = 0.248 were fabricated and characterized under dark and simulated AM1.5 solar illumination.

6.2.1 Dark j-V characterization

The diode ideality factor (*n*) and dark reverse saturation current density (j_0) was determined by using the diode equation to dark current-voltage measurements. The plot of ln (*j*) vs V curves is fitted (by using equation (24)), the intercept of the plot gives j_0 whereas the slope yields *n*.

$$j = j_0\left(e^{\frac{qV}{nk_BT}} - 1\right) \text{ i.e. } lnj = lnj_0 + \frac{q}{nk_BT}V \qquad (24)$$

The diode ideality factor gives insight information about the phenomena occurring at the p-n junction such as tunneling and recombination whereas the saturation current density denotes the recombination of charge carriers across the pn junction in the reverse bias. The large recombination of the charge carriers increases the saturation current density (low shunt resistance) which decreases the open circuit voltage values.

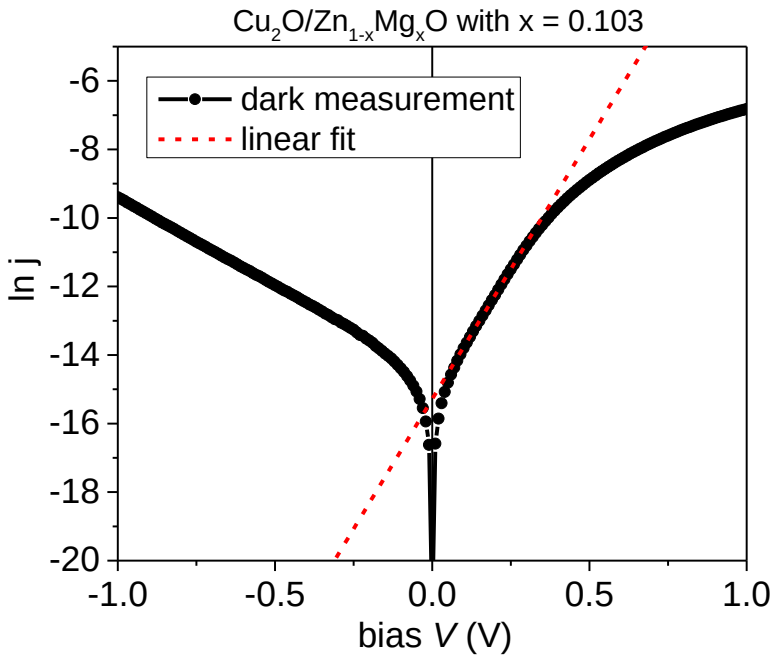

Figure 6.4: Dark lnj vs V characteristics of the $Cu_2O/Zn_{1-x}Mg_xO$ solar cell with x = 0.103

Figure 6.4 shows the dark lnj vs V curve of the $Cu_2O/Zn_{1-x}Mg_xO$ solar cell for x= 0.103 where the linear fit yields the *n* and j_0. The *n* and j_0 for the $Cu_2O/Zn_{1-x}Mg_xO$ solar cells with varying x = 0 to x = 0.248 were determined with the same linear fit procedure and the results are displayed in table 6.2. The ideality factor with values equal to or less than 2 is predicted by Shockley-Read-Hall (SRH) recombination theory by assuming single-level uniformly distributed [12] recombination centers at the center of the band gap in the depletion region which gives saturation-type reverse characteristics. However, large values of n have been associated to various phenomenon such as ohmic reverse characteristic or modified SRH theory which accounts for the non-uniform distribution of recombination centers in the depletion region [12]. In the $Cu_2O/Zn_{1-x}Mg_xO$ solar cells, due to the presence of interface states and deep level defects states in $Zn_{1-x}Mg_xO$ films, multi-level recombination becomes possible i.e. carriers recombine via more than one defect which leads to an increased recombination rate compared to single-levels as approximated by SRH, give rise to the reverse conductivity and large n values [181]. The obtained values of n and j_0 decreased from ZnO (i.e. x = 0) to Mg doped films solar cells. However, for higher Mg content the junction properties get deteriorated. In particular, for Mg doping of x = 0.103, the junction properties at dark conditions are improved as compared to un-doped ZnO which suggests an enhancement of PV performance under illumination.

Table 6.2: Junction properties of the $Cu_2O/Zn_{1-x}Mg_xO$ solar cells

$Cu_2O/ Zn_{1-x}Mg_xO$	***n*** ***(ideality factor)***	***J_0 (mA/cm^2)*** **(saturation current)**
x = 0 (ZnO)	3.0	$2.4 \cdot 10^{-6}$
x = 0.103	2.5	$4.6 \cdot 10^{-7}$
x = 0.107	2.9	$2.3 \cdot 10^{-7}$
x = 0.140	3.7	$5 \cdot 10^{-7}$
x = 0.163	4.4	$2.8 \cdot 10^{-7}$
x = 0.248	5.9	$5 \cdot 10^{-7}$

6.2.2 Illuminated j-V characterization

The PV performance of a solar cell highly depends on the V_{OC} and j_{SC} values obtained from the j-V measurements. The band diagram of a solar cell at open circuit and short-circuit condition is shown in Figure 6.5. The open-circuit voltage depends on the interface quality i.e. influenced by the recombination current due to interfacial and bulk defects, respectively. For an ideal diode, the V_{OC} can be estimated by this equation:

$$V_{oc} = \frac{nk_BT}{q} \ln\left(1 + \frac{j_{sc}}{j_0}\right) \qquad (25)$$

where j_{SC} is the short-circuit current density. This equation shows that increasing j_{SC} and decreasing j_0 improves the V_{OC} values.

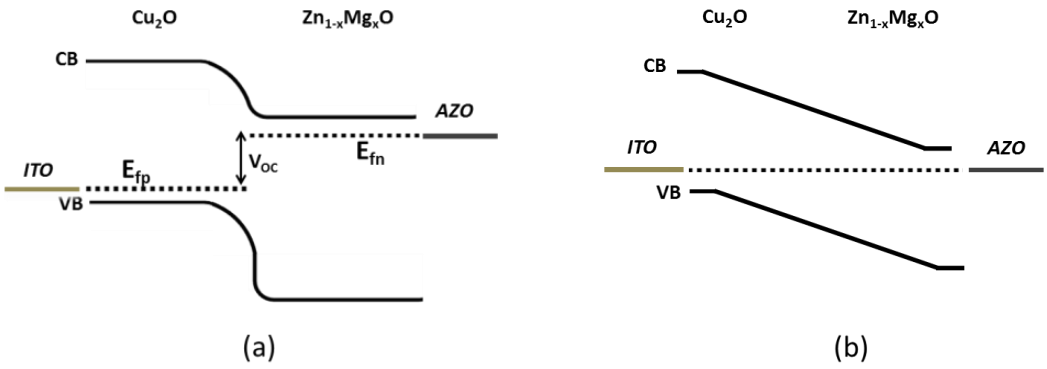

Figure 6.5: Schematic band diagram of $Cu_2O/Zn_{1-x}Mg_xO$ solar cell under (a) open circuit and (b) short circuit condition

The illuminated current density-voltage curves for the $Cu_2O/Zn_{1-x}Mg_xO$ solar cells with varying x = 0 to x = 0.248 are shown in Figure 6.6 (a). The PV performance parameters i.e. j_{SC}, V_{OC}, FF and η as a function of the Mg content of the n-layer is obtained (table 6.3) and plotted in figure 6.7. The V_{OC} has significantly increased from 360 mV(x = 0) to 550 mV (x = 0.103). The increase in V_{OC} can be attributed to the improved conduction band alignment at the $Cu_2O/Zn_{1-x}Mg_xO$ hetero-junction with the resulting reduction of recombination losses. The figure 6.6 (b) shows the schematic mechanism of charge transport and the suppression of charge recombination at the interface by Mg doping. With the shifting of CB minima of $Zn_{1-x}Mg_xO$ more close to vacuum level, the separated electrons has less chances to recombine with the holes at the valence band, thus efficient suppression of the charge recombination at the interface. Also the j_{SC} and the FF are improved, giving rise to an increase in the efficiency from η = 0.9% for x = 0 to η = 1.67% for x = 0.103. The PV performance for x = 0.103 is very similar to x = 0.107 but FF improves for the lower Mg content case.

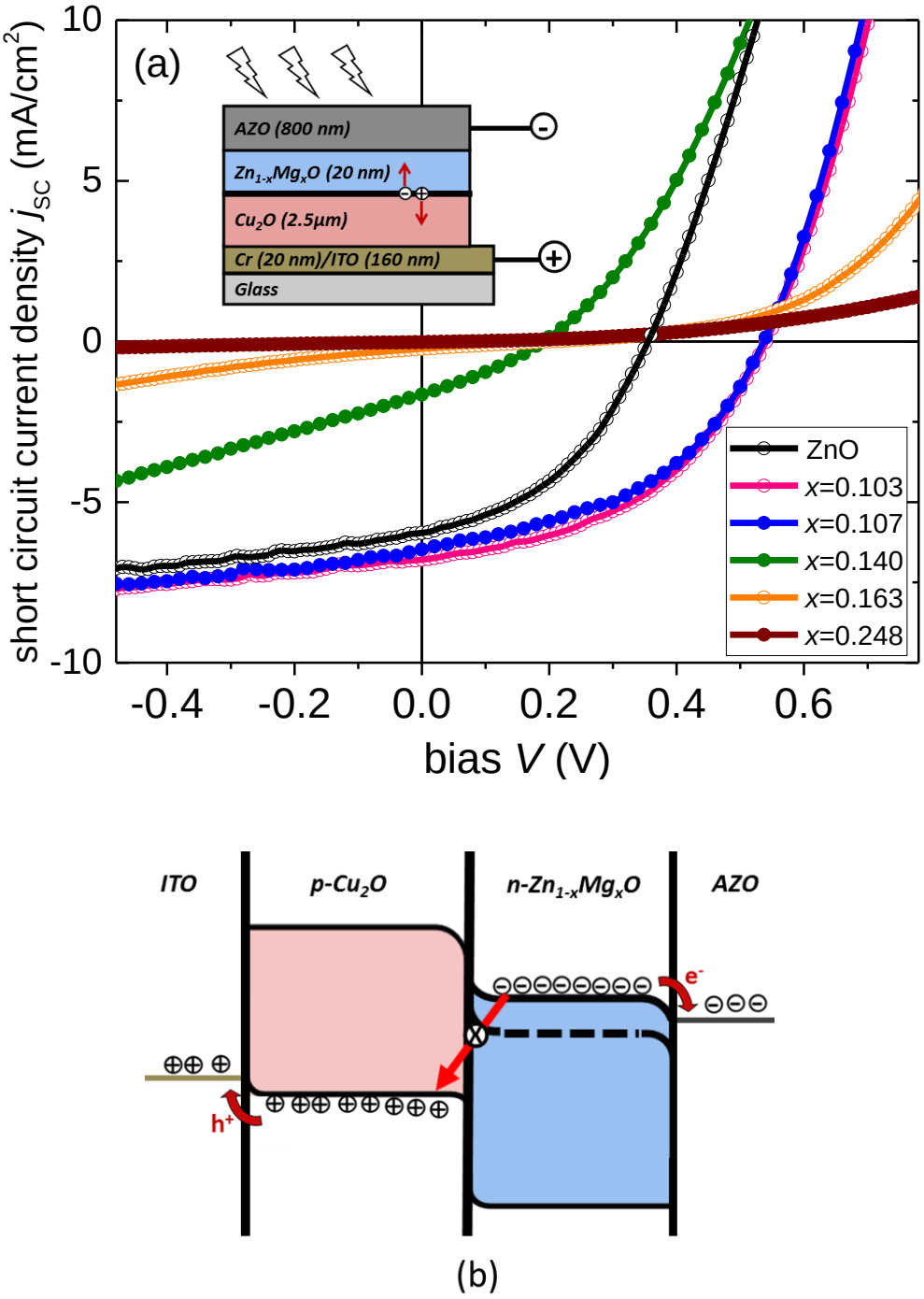

Figure 6.6: (a) illuminated j-V characteristics of the solar cells with varying x, (b) electron and hole transport mechanism and recombination in the $Cu_2O/Zn_{1-x}Mg_xO$ solar cells where the dashed line shows the energy level of un-doped ZnO layer (i.e. x = 0)

With further increase of the Mg content in the n-type film has a dramatically negative influence on the solar cell performance, with the efficiency decreasing to 0.1% for x = 0.140 and to practically null for x = 0.163 and x = 0.248. Such a behavior is not expected from the point of view of energy band structure, since the conduction band alignment should improve

with increasing x. It has been shown that in $Zn_{1-x}Mg_xO$ layers the deep level defect states increase with the Mg content, as demonstrated from pronounced defect-related luminescence, attributed to Mg interstitials or oxygen vacancies [184], [185].

Table 6.3: Photovoltaic parameters of the Cr/ITO/ECD-Cu_2O/ALD- $Zn_{1-x}Mg_xO$/AZO solar cells with different Mg content

Cu_2O/ $Zn_{1-x}Mg_xO$	j_{SC} mA/cm^2	V_{OC} mV	FF %	η %	R_{SH} Ω cm^2	R_S Ω cm^2
x = 0	5.96	360	41.0	0.88	227	25
x = 0.103	6.79	550	44.7	1.67	500	24
x = 0.107	6.47	540	44.9	1.57	215	24
x = 0.140	1.65	200	30.2	0.10	172	78
x = 0.163	0.23	200	21.8	0.01	-	-
x = 0.248	0.02	70	0	0	-	-

These states can provide a tunneling recombination path for the carriers in the solar cell, decreasing the efficiency. Furthermore, the shunt and series resistance were also determined (table 6.3). For the x = 0.103 solar cells, the shunt and series resistance were 500 and 24 Ω cm^2 respectively, while for the cells with x = 0.140 the corresponding values were 172 and 78 Ω cm^2. As the Mg content increases in the ZnO films, the shunt resistance decrease and series resistance increases. The low shunt resistance could be related to the carrier transport through the deep-level defects, whereas the increase of the series resistance could originate from an additional barrier created at the $Zn_{1-x}Mg_xO$/AZO interface.

From the measured PV performance of the cells and the hetero-junction characterization it is evident that the bandgap of the $Zn_{1-x}Mg_xO$ layer can be widely adjusted through the Mg content but the desired effect of improving the hetero-junction band alignment is not as significant as desired. Indeed, the effect of the bandgap widening is shared between the valence and the conduction band of the $Zn_{1-x}Mg_xO$. Besides, the Mg content cannot be considerably increased without detrimental effects on the cell efficiency.

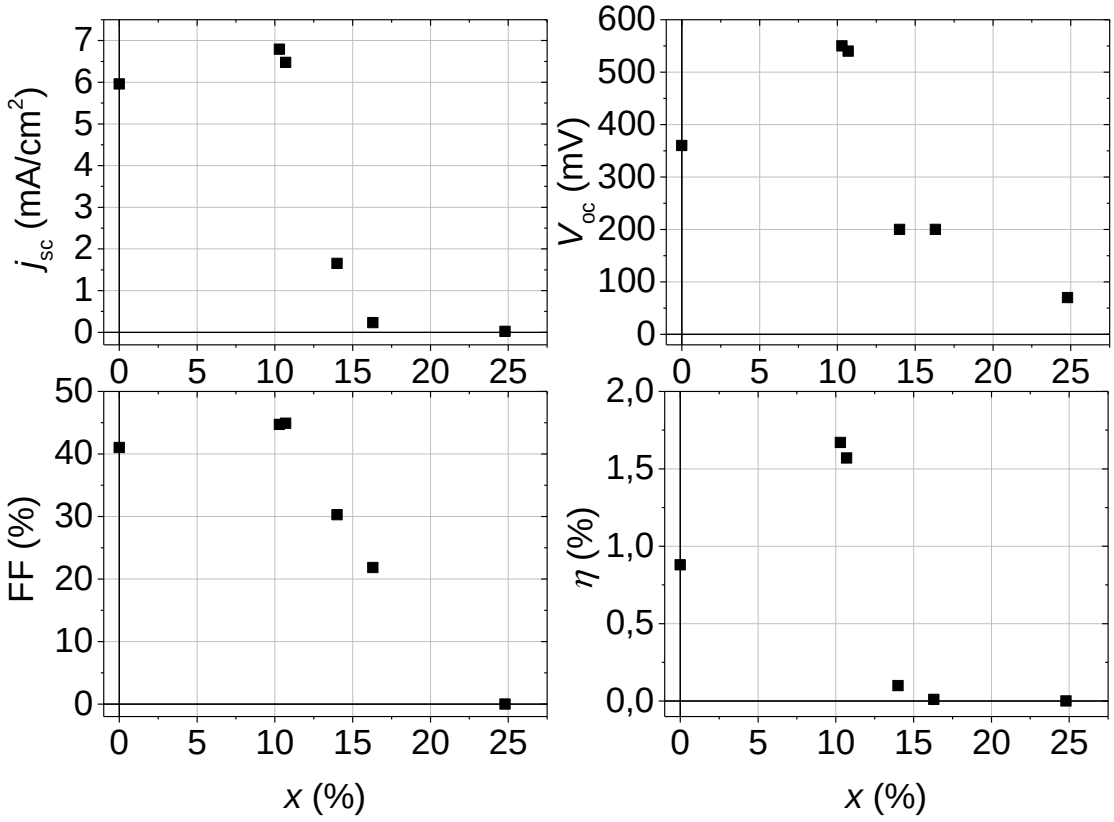

Figure 6.7: Summary of the PV performance of the solar cells with varying x

The short circuit density obtained, here, is high but far lower than the upper limit of the short circuit current density, which is about 12mA/cm^2 [186]. Also, the improved V_{OC} is still lower than the expected limit of 1.7 V [187]. It is, therefore, necessary to improve the hetero-interface as well as lowering the series resistances values in order to achieve higher efficiencies in Cu_2O based solar cells.

6.3 Electrical characterization of Cu_2O (electrodeposited at different bath temperatures)/ALD-$Zn_{0.9}Mg_{0.1}O$ solar cells

The Cu_2O films were also electrodeposited at higher bath temperatures (i.e. 60, 70°C) on Cr/ITO electrode other than 50°C (state-of-the art ECD bath temperature). To investigate their PV performance, solar cells were fabricated with $Zn_{0.9}Mg_{0.1}O$ layers i.e. with Mg content of 0.103 which illustrates the highest efficiency Cu_2O/ZnMgO solar cells. The solar cells were characterized under dark and simulated AM1.5 solar illumination.

6.3.1 Dark j-V characterization

Figure 6.8 illustrates the schematic of $Cu_2O/Zn_{0.9}Mg_{0.1}O$ hetero-junction solar cell electrodeposited at different ECD bath temperatures. From the dark measurements, the *n* and j_0 values for the $Cu_2O/Zn_{0.9}Mg_{0.1}O$ solar cells were determined with the same linear fit procedure as above and the results are displayed in table 6.4.

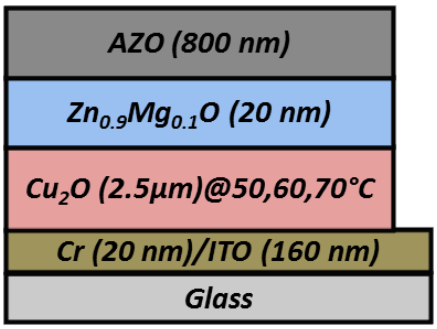

Figure 6.8: Schematic of $Cu_2O/Zn_{0.9}Mg_{0.1}O$ solar cell electrodeposited at different bath temperatures

The solar cells with Cu_2O electrodeposited at higher bath temperatures have shown higher *n* and lower j_0 values as compared to the lower bath temperature deposited solar cells. The lower j_0 values indicate an improvement in the open circuit photo-voltages.

Table 6.4: Junction properties of the $Cu_2O/Zn_{1-x}Mg_xO$ solar cells, electrodeposited at different bath temperatures

Cu_2O-ECD bath Temp.	n (ideality factor)	J_0 (mA/cm^2) (saturation current)
50°C	2.5	$4.6 \cdot 10^{-7}$
60°C	3.0	$7.8 \cdot 10^{-8}$
70°C	3.4	$5.4 \cdot 10^{-8}$

6.3.2 Illuminated j-V characterization

The illuminated j-V curves are shown in Figure 6.9. The obtained PV parameters as a function of the ECD bath temperature are shown in Table 6.5. At both bath temperature i.e. 60 and 70°C, the PV performance is almost similar. With increased ECD bath temperature, indeed, the V_{OC} shows an improvement from 550 mV (T = 50°C) to 650 mV (T = 60°C) mV but current density decreased from 6.8 mA/cm^2 (T = 50°C) to 4.9 mA/cm^2 (T = 60°C) (Table 6.5).

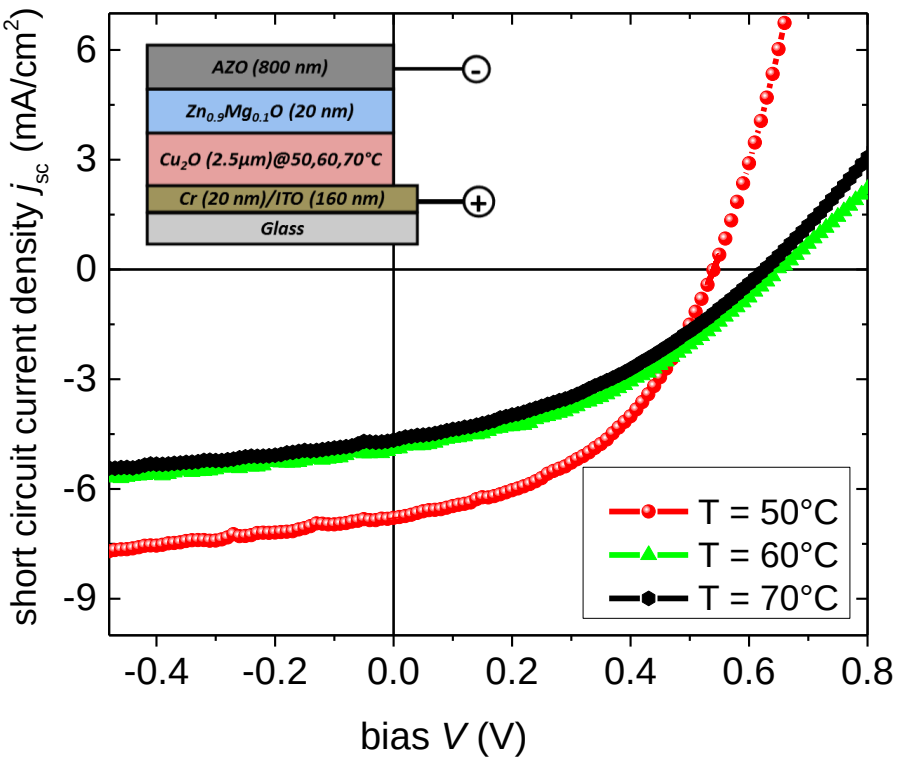

Figure 6.9: Illuminated j-V characteristics of the solar cells for the Cu_2O films deposited at different bath temperatures

The shunt resistance decreased and series resistance increased for the solar cells obtained at higher bath temperatures (table 6.5). The low current density obtained and low FF originates from high series resistance decreased the efficiency of the devices from 1.67% (T = 50°C) to 1.2% (T = 60°C). Indeed, the Cu_2O films electrodeposited at higher bath temperatures shows an impressive V_{oc} values which is higher than the best performing solar cells but lower FF as well as shunt resistance values degrade the PV performance.

Table 6.5: Photovoltaic parameters of the Cr/ITO/ECD-Cu_2O/ALD- $Zn_{1-x}Mg_xO$/AZO solar cells for different ECD bath temperatures

ECD bath temp. (°C)	j_{SC} mA/cm^2	V_{OC} mV	FF %	η %	R_{SH} Ω cm^2	R_S Ω cm^2
T = 50	6.79	550	44.7	1.67	500	24
T = 60	4.9	650	38	1.2	271	73
T = 70	4.6	620	38	1.1	282	66

6.4 Capacitance-voltage (C-V) characterization of $Cu_2O/Zn_{0.9}Mg_{0.1}O$ solar cells

The CV measurements are very useful to determine the junction electrical properties such as built-in voltages (V_{bi}), doping density (N). The measurements were performed on the best performing solar cells i.e. Cu_2O (ECD at 50°C)/$Zn_{0.9}Mg_{0.1}O$. For the comparison, CV measurements were also performed to determine the bath temperature influence on the junction of Cu_2O (ECD at 60, 70°C)/$Zn_{0.9}Mg_{0.1}O$ solar cells.

To solve for the V_{bi}, the *depletion approximation* is assumed i.e. the contribution of free electrons and holes into the space charge region are ignored. Furthermore, the doping levels in the p- and n-regions are assumed to be constant distant from the junction and change abruptly change at the junction interfacial region (abrupt *pn* junction). The charge neutrality valid at the junction i.e. $N_A w_p = N_D w_n$, where N_A and N_D are acceptor and donor doping concentrations in p- and n- region, respectively and w_p and w_n are the depletion layer width in p- and n- region, respectively. The width of the depletion region on either side of the junction varies inversely with doping concentration. In other words, the depletion region extends into the side which has the lowest doping level i.e. into Cu_2O side and hence the band bending i.e. the V_{bi} is mostly in to the Cu_2O side as shown in figure 6.10.

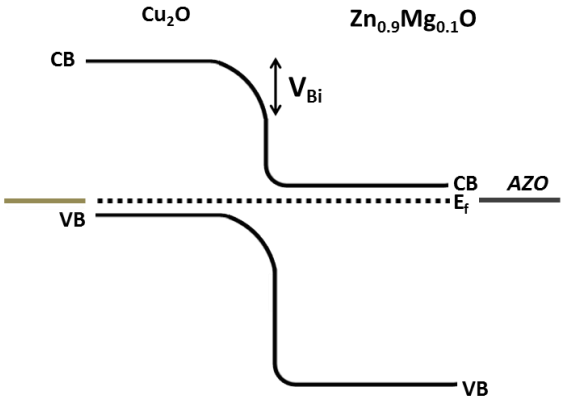

Figure 6.10: Schematic of the band bending at the Cu_2O and $Zn_{0.9}Mg_{0.1}O$ interface where the V_{bi} is mostly into the Cu_2O layer

The total built-in potential across the junction is given by:

$$V_{bi} = \frac{kT}{q} ln\left(\frac{N_D N_A}{n_i^2}\right) \qquad (26)$$

The depletion widths are given as:

$$w_p = \sqrt{\frac{2\varepsilon\varepsilon_0 V_{bi}}{q}\left[\frac{N_D}{N_A(N_A+N_D)}\right]}$$

$$w_n = \sqrt{\frac{2\varepsilon\varepsilon_0 V_{bi}}{q}\left[\frac{N_A}{N_D(N_A+N_D)}\right]}$$

In the depletion approximation, a change in applied voltage will cause a change in stored charge at the edges of the regions i.e. expansion or contraction of majority charge carrier distributions near the edges of the depletion region in response to applied bias. The depletion region capacitance, C, is given by:

$$C = \frac{\varepsilon\varepsilon_0 A}{w_p}$$

where ε is dielectric constant, ε_0 is permittivity of free space ($8.854.10^{-12}$ F/m), A is the area, w_p is the depletion region width. Under reverse bias, the depletion region capacitance dominates the total diode capacitance. For the one-sided abrupt pn junction, the depletion region width (w_p) in to the Cu_2O layer can be obtained by this relation at zero bias:

$$w_p = \sqrt{\frac{2\varepsilon\varepsilon_0(V_{bi}-V)}{qN_A}}$$

Also, $Q = qN_A w_p$, by using above equation we obtain:

$$Q = \sqrt{2q\varepsilon\varepsilon_0 N_A(V_{bi}-V)}$$

where V is the applied bias and then the junction capacitance is given by:

$$C = \left|\frac{dQ}{dV}\right| = qN_A\frac{dw_p}{dV} = A\sqrt{\frac{q\varepsilon\varepsilon_0 N_A}{2(V_{bi}-V)}}$$

or

$$(V_{bi}-V) = \frac{Aq\varepsilon\varepsilon_0 N_A}{2C^2}$$

Hence, the doping concentration is:

$$N_A = -\frac{2}{qA^2\varepsilon\varepsilon_0}[d(1/C^2)/dV]^{-1} \qquad (27)$$

where C represents the capacitance of the space charge region, ε is dielectric constant of the Cu_2O (6.5), ε_0 is permittivity of free space ($8.854.10^{-12}$ F/m), A is the area, N_A is the acceptor doping concentration, V is the applied voltage, and q is the electronic charge ($1.6.10^{-19}$ C). This indicates that a plot of $1/C^2$ versus the applied voltage should be a straight line. The slope can be used to obtain the doping level in the semiconductor and the intercept with the voltage axis should equal to the built-in voltage. The plot of $1/C^2$ vs. V at different bath temperatures is shown in figure 6.11.

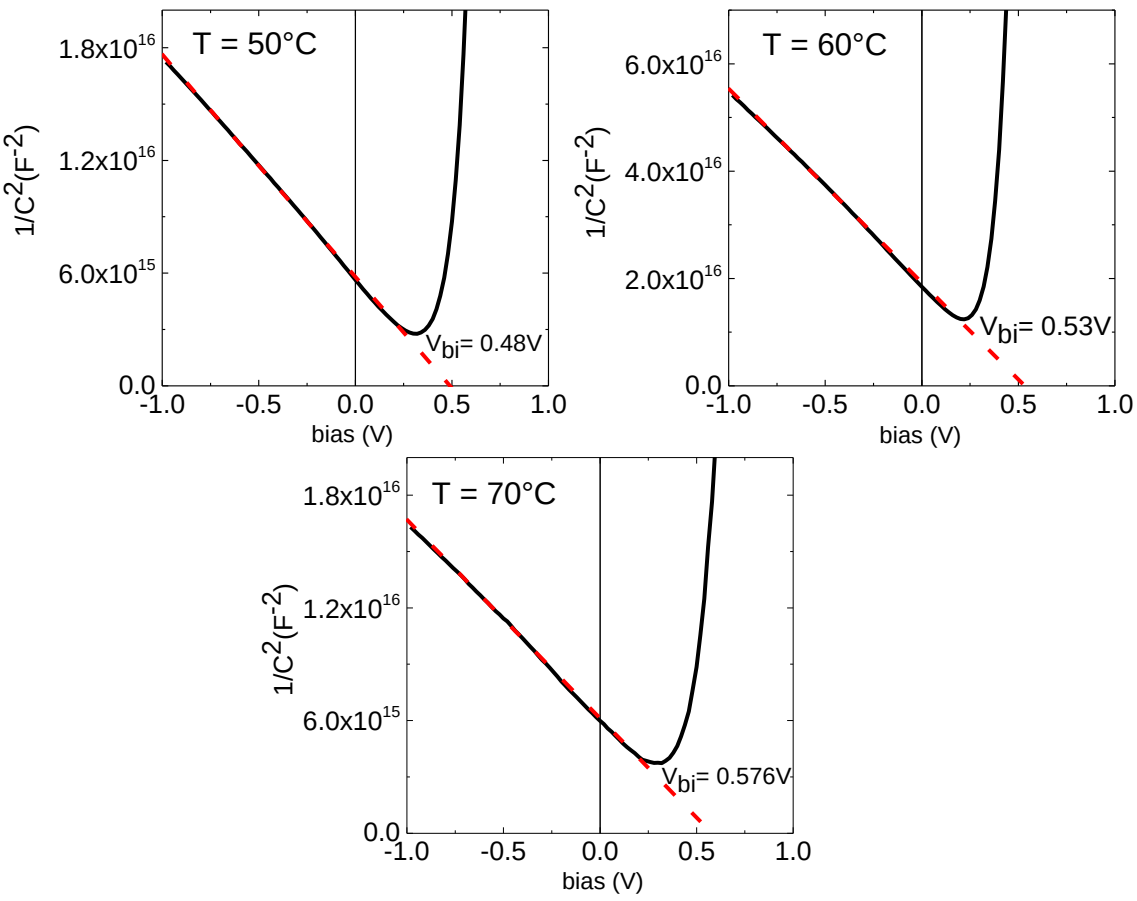

Figure 6.11: Capacitance versus voltage characteristics of the $Cu_2O/Zn_{0.9}Mg_{0.1}O$ solar cells for ECD bath temperature of 50°C, 60°C and 70°C

The carrier concentration in the Cu_2O film is of paramount important as it determines the built-in potential as well as affects the width of depletion region. The obtained doping concentration illustrates that as the bath temperature during ECD increases from 50°C to 70°C, the free carrier concentration in the absorber layer decreases (table 6.6). The decrease in carrier concentration increase the built-in potential value from 50 to 70°C, as built-in potential varies with the donor and acceptor carrier concentration (eq.26). On the other hand, depletion region width, also, depends on the doping concentration of p and n layer. Since, the carrier concentration in Cu_2O lowers than the n-layer, the width of depletion region will be extended more into Cu_2O film. The width of depletion region, also, increases with bath temperature. Table 6.6 shows the V_{bi}, N, and depletion layer width (W) values obtained from the C-V measurements as function of ECD bath temperature.

Table 6.6: Capacitance-voltage measurements of the Cr/ITO/Cu_2O/$Zn_{1-x}Mg_xO$/AZO solar cells for different ECD bath temperatures

ECD bath temp. (°C)	V_{bi} mV	Slope ($x10^{16}$)	N($x10^{17}$) cm^{-3}	W_p nm
T = 50	480	-1.18	3.3	32
T = 60	530	-3.6	2.5	39
T = 70	576	-1.1	2.2	43

Furthermore, capacitance was also measured as a function of applied bias at different frequencies as shown in figure 6.12. The capacitance varies as the function of frequency in all three samples deposited at different bath temperatures indicating the deep-level traps in the Cu_2O layer. The capacitance at the lower frequencies is determined by carriers that re-emit from the deep-traps states whereas at high frequency only the fast emitting traps contribute to capacitance. Deep the trap is, longer it takes time to emit. Hence, as the frequency increases, capacitance decreases in all studied sample because less traps contribute to the measured capacitance, resulting in a drop of the capacitance value.

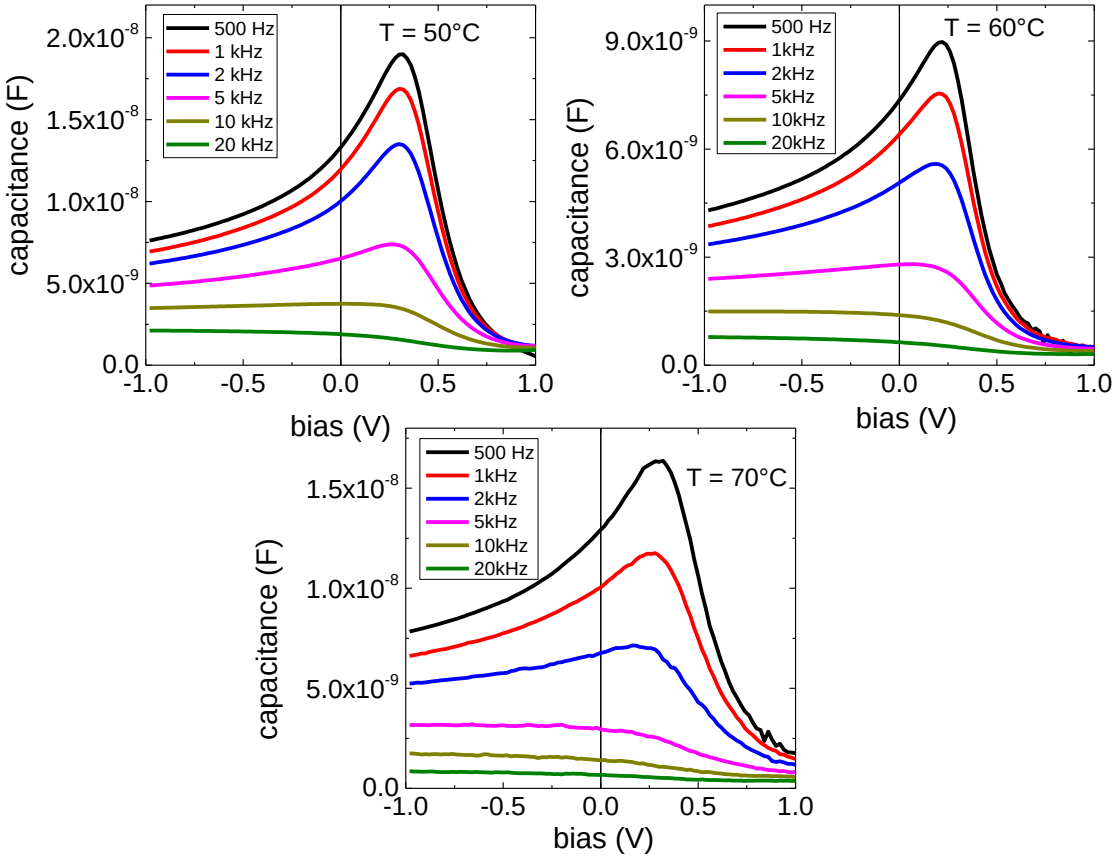

Figure 6.12: Capacitance versus voltage characteristics at different frequencies for the $Cu_2O/Zn_{0.9}Mg_{0.1}O$ solar cells electrodeposited at 50°C, 60°C and 70°C

The CV measurements provide the in-detailed information about the j-V characterization obtained for the $Cu_2O/Zn_{0.9}Mg_{0.1}O$ solar cells. For the state-of-the-art deposited Cu_2O films, the V_{bi} and free carrier density values for the best performing $Cu_2O/Zn_{0.9}Mg_{0.1}O$ solar cells are obtained as 480 mV and $3.3 \cdot 10^{17}$ cm^{-3}. As the bath temperature increased from 50 to 70°C, the Cu_2O (60 and 70°C)/$Zn_{0.9}Mg_{0.1}O$ solar cells showed an improvement in V_{oc} values (table 6.5) as compared to Cu_2O (50°C)/$Zn_{0.9}Mg_{0.1}O$ solar cells which is attributed to the increase in V_{bi} values obtained at higher bath temperatures (table 6.6). However, the current density obtained for Cu_2O (60 and 70°C)/$Zn_{0.9}Mg_{0.1}O$ solar cells is low. With the increase of V_{OC} we would expect an increase of FF as well as shunt resistance but obtained lower shunt resistance values and frequency dependent capacitance measurements illustrate high level of trap centers in the absorber layer. These deep trap centers can reduce the minority carrier lifetime and results in less photo-current collection.

Hence the charge transportation at the junction is effected by the defects recombination where deep-level traps play an important role as indicated by C-V measurements. Therefore, decreasing the defect densities in the p-layer as well as at the interface and enhancement of carrier collection by lowering of series resistance is required to achieve high efficiencies in Cu_2O-based solar cells.

6.5 Optical simulation

Optical simulations were employed to investigate the effect of Cu_2O morphology on the light absorption in the solar cell. The simulations were carried out by using the finite difference time domain (FDTD) method. FDTD, a numerical method, is very useful in solving Maxwell's equations in complex geometries. All the FDTD calculations were performed by using the commercial LUMERICAL software [188].

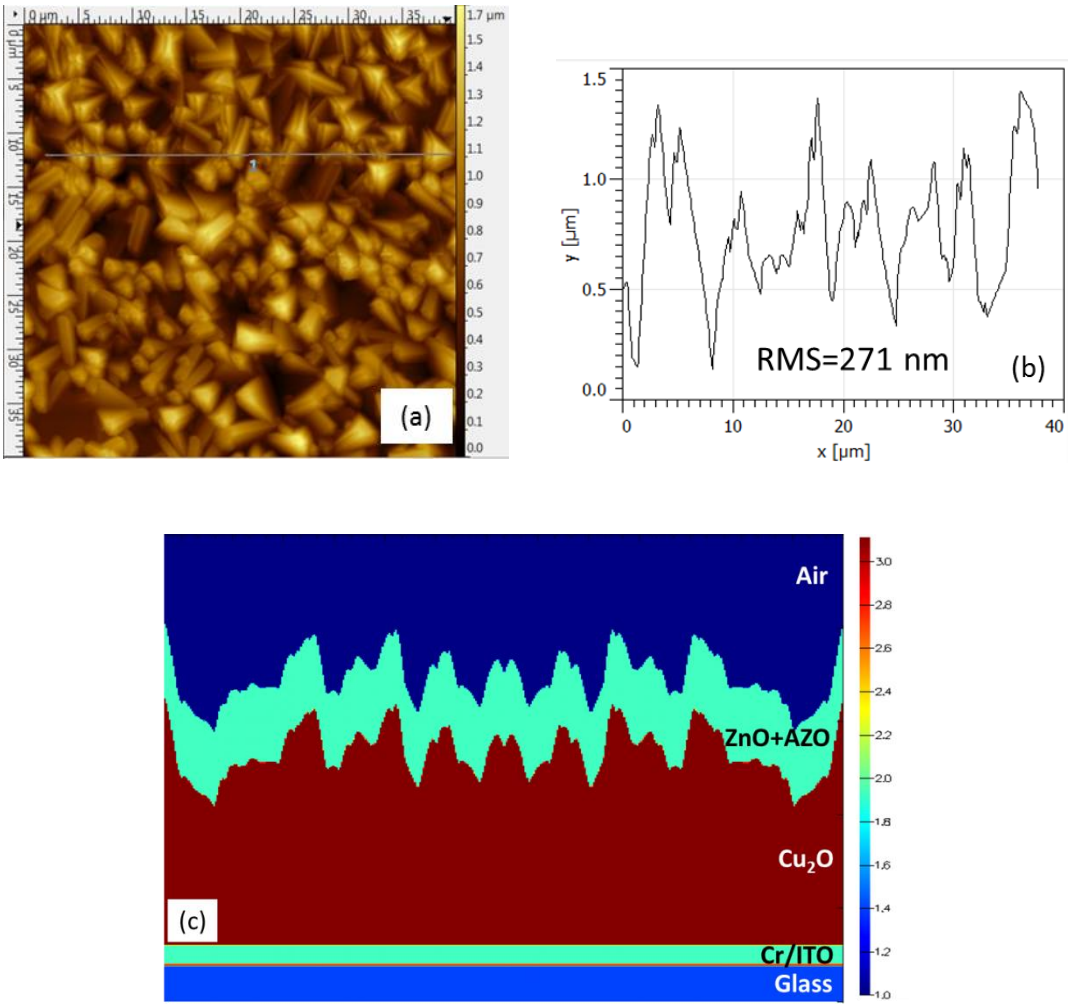

Figure 6.13: (a) AFM image of the Cu_2O surface, (b) Root mean square (RMS) roughness and the roughness cross section profile, (c) solar cell structure based on the surface texture obtained from SEM and AFM used for simulating the optical properties where the colors display the different refractive indices of the films

The surface texture of Cu_2O was determined by SEM (figure 6.3 (c)) and atomic force microscopy (AFM) as shown in figure 6.13 (a and b). The variation of refractive index and extinction coefficient of the different layers, used for the optical simulation, as a function of wavelength, is shown in Figure 6.15. The simulated solar cell was Cr (20 nm)/ITO (160 nm)/Cu_2O (2.5 µm)/ZnO (20 nm)/AZO (800 nm) as shown in figure 6.13 (c), based on the refractive indices data (figure 6.15) and surface texture obtained from SEM and AFM measurements.

The solar cell structure was simulated with flat and rough Cu_2O surface morphology to investigate the light absorption and reflectance in the absorber layer. The simulations showed that the rough Cu_2O surface enhances the light absorption, since the light is scattered on the pyramid-like grains and directed back into the absorber, thus increasing the optical path. Compared to a flat absorber, the optical absorption is larger by up to 3% over the window 400-700 nm (Figure 6.14 (a)). The specular and diffuse reflectivity simulation showed that the reflectance is reduced to the same amount of 3%, owing to the rough surface. Apart from the increased absorption, the rough absorber surface gives rise to a larger surface of the heterojunction, thus enhancing the extracted current.

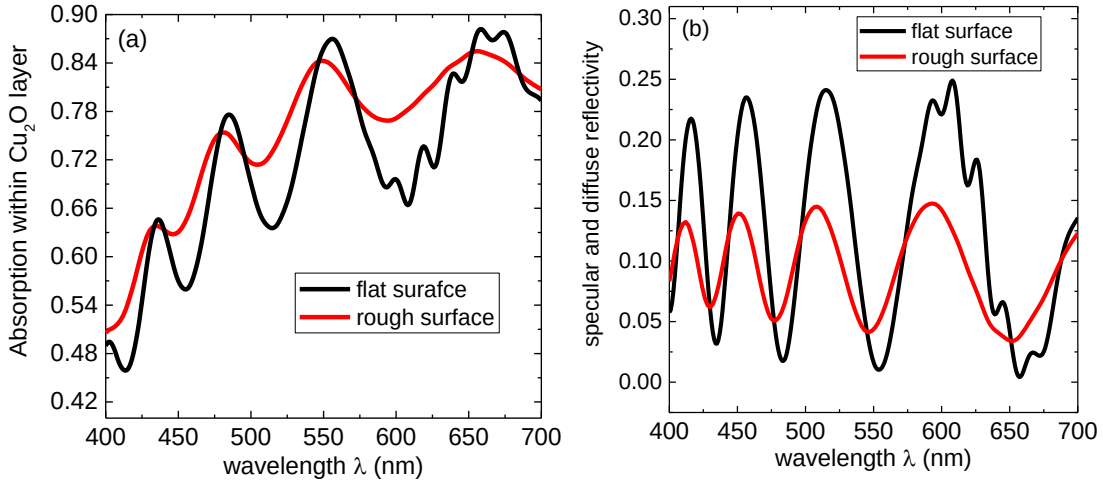

Figure 6.14: Simulated (a) absorption and (b) specular and diffuse reflectivity for a flat and rough Cu_2O surface

With the optical simulation, we can say that the absorber morphology plays a significant role in the light absorption. The rough Cu_2O surface obtained by electrochemical deposition is beneficial to enhance light absorption, as opposed to a flat surface.

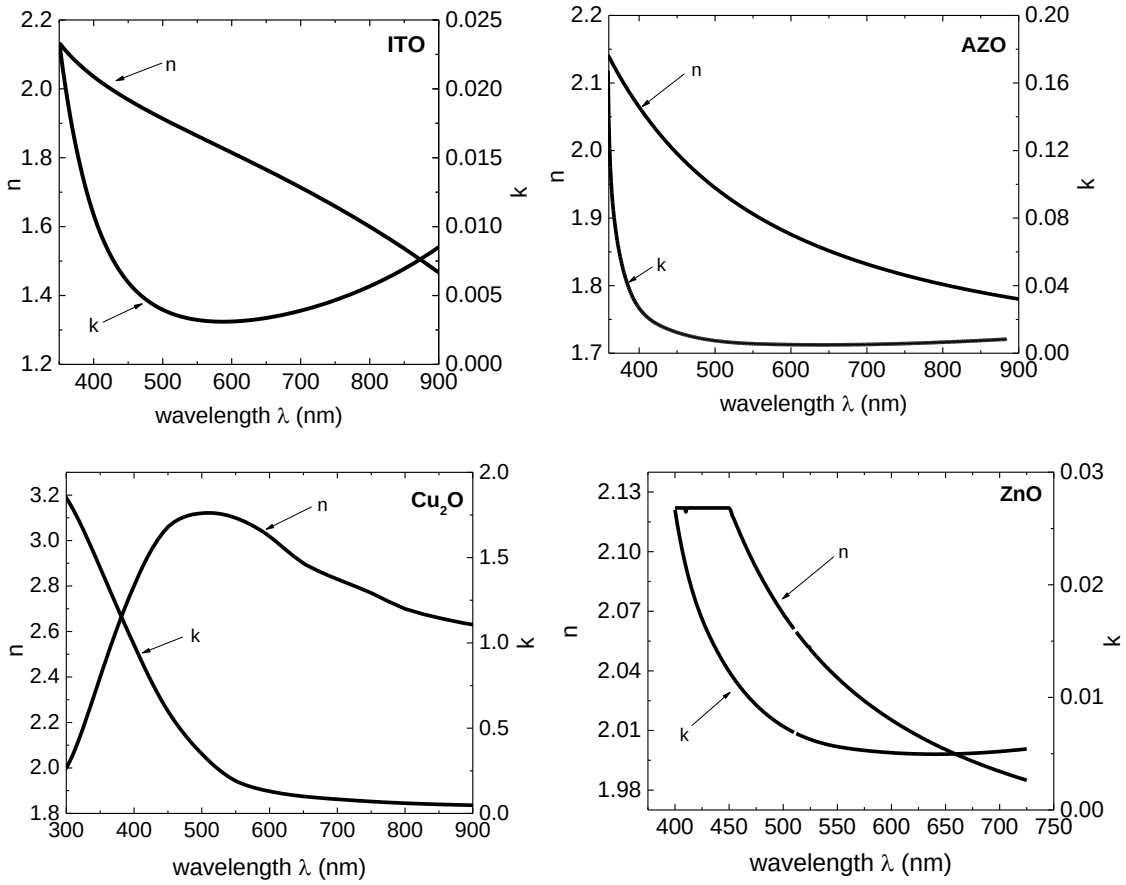

Figure 6.15: Refractive index and extinction coefficient of (a) ITO, (b) AZO, (c) Cu_2O, and (d) ZnO layers as a function of wavelength (data taken from [189])

Chapter 7

Summary and Conclusions

In this thesis, all-oxide solar cells based on electrodeposited p-type Cu_2O absorber and atomic layer deposited n-type $Zn_{1-x}Mg_xO$ were investigated. The solar cell architecture studied here is of the substrate type and almost exclusively composed of oxide layers i.e. glass/Cr/ITO/p-Cu_2O/n-$Zn_{1-x}Mg_xO$/AZO. The work has focused on enhancing the performance of Cu_2O/$Zn_{1-x}Mg_xO$ solar cells by: (1) improving the quality of Cu_2O film to obtain efficient absorber properties on a low-cost conductive back electrode (BE) by optimizing the deposition parameters of ECD and (2) improving the energy band alignment at the heterojunction between ECD-Cu_2O and ALD-$Zn_{1-x}Mg_xO$ with varying x (from 0 to 0.248).

The ECD deposition parameters, as well as the structural and electrical properties of the conducting substrate play a significant role in determining the structure and morphology of the Cu_2O films. To this regards, three different back electrodes were employed, namely Ti/Au, Ti/Ag and Cr/ITO. Electrodes employing precious metals (Ag, Au) have already been used in the literature, while Cr/ITO provides a low-cost alternative. For a solar cell, a highly conductive electrode is required for the efficient charge carrier extraction but, on the same time, for the ECD this provides less control over the current density through the applied potential, eventually leading to defect-rich deposits due to mass-transport-controlled electrode reactions. The use of the Cr/ITO electrode proved advantageous, providing the best combination of properties and cost. Its sheet resistance is low enough (17 Ω/□) to be used as a solar cell electrode and, at the same time, allows control over the current density during ECD to obtain high-quality Cu_2O growth, controlled by charge-transfer. Thus, a detailed analysis was made on Cr/ITO electrode to optimize the ECD parameters to obtain large grains and void-free Cu_2O films.

The ECD of Cu_2O was performed at different negative potentials on the Cr/ITO electrode to study (1) the growth evolution as a function of deposition time and (2) the over-potential effect on the morphology of Cu_2O films. We observed that the Cu_2O films, under the used deposition conditions, grow by instantaneous nucleation. Clusters of nuclei at close proximity eventually merge to form single islands and as the deposition continuous the island density decreases from its initial value. With increasing electrodeposition potential for the Cu_2O, and

as we enter in the growth region controlled by mass transport, the grain size of the Cu_2O film becomes smaller and the films become more defect-rich, which is not desirable for the solar cell absorber. Suitable absorber properties, such as large grains, textured and void-free films are obtained by setting the electrodeposition potential at the threshold between the kinetic- and the mass-transport-controlled regime. The obtained film features a rough surface due to the large (>2 μm) and well-faceted grains of Cu_2O with optical band gap of 1.93 eV. The XRD analysis reveals a multi-textured film with prominent (111), (200) and (220) reflections in which (111) is the strongest peak. Thus, with the proper choice of the electrodeposition parameters it is possible to control and enhance the grain size and quality of the absorber. Furthermore, Cu_2O deposition was performed at different ECD bath temperatures i.e. at 60°C and 70°C on the Cr/ITO electrode. With increased bath temperature, the current density during ECD increased, which accelerates the electrode kinetics. XRD analysis illustrates that the preferred crystal orientation for the Cu_2O films remains unchanged with increasing bath temperature i.e. (111) is the strongest peak in all cases.

The $Zn_{1-x}Mg_xO$ layers were fabricated by ALD at deposition temperature of 150°C and the Mg concentration in the ZnO layers was controlled by varying the number of MgO cycles. The incorporation of Mg^{2+} to the ZnO lattice and the precise atomic concentration of Mg in the ZnO layers, were analyzed by XPS. In the XPS spectra, the Mg 1s peak of all $Zn_{1-x}Mg_xO$ layers showed a considerable shift to higher binding energies as compared to MgO, whereas a much less significant shift to lower binding energies was observed for the Zn doublet peak for $Zn_{1-x}Mg_xO$ compared to ZnO. This suggests the substitutional incorporation of Mg into the ZnO lattice, with the corresponding change of the Mg coordination number from octahedral to tetrahedral. In addition, the valence band maximum positions of $Zn_{1-x}Mg_xO$ for varying x (from x = 0 to x = 0.163) was also analyzed by XPS. The VBM position of $Zn_{1-x}Mg_xO$ layers shifts down as compared to un-doped ZnO with increasing Mg content. This also correlated with the optical transmittance spectra of $Zn_{1-x}Mg_xO$ films. The transmittance of the films increased with increasing x due to the widening of the optical band gap. A linear relation of the optical bandgap was found from 3.2 eV (x = 0) to 3.9 eV (x = 0.33).

The structural properties of the ALD $Zn_{1-x}Mg_xO$ films were investigated by XRD. Very thin films (20 nm) had an extremely weak ZnO (002) peak for small Mg contents (<10%). The films are therefore amorphous/nanocrystalline with the onset of crystallization being visible for low Mg content. On the other hand, thicker films (100 nm) were textured. While the undoped ZnO has a strong (002) texture, for all Mg-containing films, the (100) texture dominates, while the (002) peak becomes gradually weaker. Besides, the position of the

(002) peak is shifted to higher 2θ values with increasing Mg, indicating the substitutional incorporation of the small ionic radius Mg^{2+} into Zn^{2+} sites.

XPS was also used to determine experimentally the band-offset positions at the $Cu_2O/Zn_{1-x}Mg_xO$ hetero-interface. With increasing Mg content in the $Zn_{1-x}Mg_xO$ films, the bottom of the conduction band is shifted upwards (lower electron affinity). Therefore, an increase in the open circuit voltage and decrease of the carrier recombination in solar cells is expected.

Indeed, solar cells incorporating $Zn_{1-x}Mg_xO$ with Mg content ~0.1 show a significant improvement in their performance as opposed to cells with undoped ZnO. The V_{OC} is significantly increased from 360 mV (x = 0) to 550 mV (x = 0.103). The increase in V_{OC} can be attributed to the improved conduction band alignment at the $Cu_2O/Zn_{1-x}Mg_xO$ heterojunction with the resulting reduction of recombination losses. Also the j_{SC} and the FF were improved, giving rise to an increase in efficiency from η = 0.9% for x = 0 to η = 1.67% for x = 0.103. Further increase of the Mg content in the n-type film has a dramatically negative influence on the solar cell performance, with the efficiency decreasing to practically null for x > 0.15. The reason for this may be the increasing amount of deep level defect states in the $Zn_{1-x}Mg_xO$ film, which provide a tunneling recombination path for the carriers, thus, decreasing the efficiency.

From the evaluation of the solar cells' PV performance, combined with the characterization of the heterojunction, we can conclude that, although the bandgap of $Zn_{1-x}Mg_xO$ can be widely modified through the Mg content, the desired effect of improving the heterojunction band alignment is not as significant as we would expect. This is because the bandgap widening is shared between the valence and the conduction band of the $Zn_{1-x}Mg_xO$. On the other hand, the Mg content cannot be significantly increased without adversely affecting the cell efficiency. In view of these limitations, the Ga_2O_3, $Al_xGa_{1-x}O$ and $Zn_x Ge_{1-x}O$ n-layers, as discussed in the introduction, with an electron affinity matching the low electron affinity of Cu_2O, provide a better matching to the absorber.

The choice of a suitable n-type layer is, undoubtedly, vital for the solar cell performance. On the other hand, an equally important factor is the optimization of the absorber itself. The electrochemical deposition of Cu_2O is more attractive for large scale production than the thermal oxidation of Cu sheets, assuming that comparable levels of efficiency are obtained. To achieve this, the quality of the electrodeposited Cu_2O has to be improved. The present work has shown that through a proper choice of the electrodeposition parameters it is

possible to enhance the grain size and quality of the absorber on a conductive substrate that is free of precious metals. Considering these results and the recent literature on Cu_2O solar cells, it can be anticipated that all-oxide solar cells develop to a low-cost and efficient PV technology in the near future.

BIBLIOGRAPHY

[1] P. Würfel and U. Würfel, *Physics of solar cells: from basic principles to advanced concepts*, 3rd edition. Weinheim: Wiley-VCH Verlag GmbH & Co. KGaA, 2016.

[2] N. S. Lewis and D. G. Nocera, 'Powering the planet: Chemical challenges in solar energy utilization', *Proc. Natl. Acad. Sci.*, vol. 103, no. 43, pp. 15729–15735, Oct. 2006.

[3] 'Renewables 2016 Global Status Report'. [Online]. Available: http://www.ren21.net/gsr-online/. [Accessed: 07-Mar-2017].

[4] 'Renewables 2018 Global Status Report'. .

[5] M. A. Green, Y. Hishikawa, E. D. Dunlop, D. H. Levi, J. Hohl-Ebinger, and A. W. Y. Ho-Baillie, 'Solar cell efficiency tables (version 51)', *Prog. Photovolt. Res. Appl.*, vol. 26, no. 1, pp. 3–12, Jan. 2018.

[6] C. Candelise, J. F. Speirs, and R. J. K. Gross, 'Materials availability for thin film (TF) PV technologies development: A real concern?', *Renew. Sustain. Energy Rev.*, vol. 15, no. 9, pp. 4972–4981, Dec. 2011.

[7] C. Wadia, A. P. Alivisatos, and D. M. Kammen, 'Materials Availability Expands the Opportunity for Large-Scale Photovoltaics Deployment', *Environ. Sci. Technol.*, vol. 43, no. 6, pp. 2072–2077, Mar. 2009.

[8] Y. S. Lee, M. T. Winkler, S. C. Siah, R. Brandt, and T. Buonassisi, 'Hall mobility of cuprous oxide thin films deposited by reactive direct-current magnetron sputtering', *Appl. Phys. Lett.*, vol. 98, no. 19, p. 192115, May 2011.

[9] T. Minami, Y. Nishi, and T. Miyata, 'Efficiency enhancement using a $Zn_{1-x}Ge_x$ -O thin film as an n-type window layer in Cu_2O-based heterojunction solar cells', *Appl. Phys. Express*, vol. 9, no. 5, p. 052301, Apr. 2016.

[10] 'A.E. Becquerel, Comt. Rend. Acad. Sci. 9, 561, 1839'. .

[11] 'File:Solar Spectrum.png - Wikimedia Commons'. [Online]. Available: https://commons.wikimedia.org/wiki/File:Solar_Spectrum.png. [Accessed: 28-Mar-2017].

[12] W. Shockley and H. J. Queisser, 'Detailed Balance Limit of Efficiency of p-n Junction Solar Cells', *J. Appl. Phys.*, vol. 32, no. 3, pp. 510–519, Mar. 1961.

[13] V. Vijayakumar and D. P. Birnie, 'Optical and electronic simulation of gallium arsenide/silicon tandem four terminal solar cells', *Sol. Energy*, vol. 97, pp. 85–92, Nov. 2013.

[14] G. Barbarino, R. de, G. De, C. Maximiliano, S. Russo, and D. Vivolo, 'Silicon Photo Multipliers Detectors Operating in Geiger Regime: an Unlimited Device for Future Applications', in *Photodiodes - World Activities in 2011*, J. W. Park, Ed. InTech, 2011.

[15] J. Nelson, *The Physics of Solar Cells*. PUBLISHED BY IMPERIAL COLLEGE PRESS AND DISTRIBUTED BY WORLD SCIENTIFIC PUBLISHING CO., 2003.

[16] 'Dr. Dietmar Knipp, introduction to electronic devices'. .

[17] C. Sah, R. Noyce, and W. Shockley, 'Carrier Generation and Recombination in P-N Junctions and P-N Junction Characteristics', *Proc. IRE*, vol. 45, no. 9, pp. 1228–1243, Sep. 1957.

[18] T. Markvart and L. Castañer, 'Principles of Solar Cell Operation', in *Solar Cells*, Elsevier, 2013, pp. 3–25.

[19] 'Rahul Dewan,phD thesis, OPTICS IN THIN-FILM SILICON SOLAR CELLS WITH PERIODIC SURFACE TEXTURE'. .

[20] T. Minemoto *et al.*, 'Theoretical analysis of the effect of conduction band offset of window/CIS layers on performance of CIS solar cells using device simulation', *Sol. Energy Mater. Sol. Cells*, vol. 67, no. 1–4, pp. 83–88, Mar. 2001.

[21] T. Takamoto, E. Ikeda, H. Kurita, and M. Ohmori, 'Over 30% efficient InGaP/GaAs tandem solar cells', *Appl. Phys. Lett.*, vol. 70, no. 3, pp. 381–383, Jan. 1997.

[22] K. A. Bertness, S. R. Kurtz, D. J. Friedman, A. E. Kibbler, C. Kramer, and J. M. Olson, '29.5%-efficient GaInP/GaAs tandem solar cells', *Appl. Phys. Lett.*, vol. 65, no. 8, pp. 989–991, Aug. 1994.

[23] K. Sasaki, T. Agui, K. Nakaido, N. Takahashi, R. Onitsuka, and T. Takamoto, 'Development of InGaP/GaAs/InGaAs inverted triple junction concentrator solar cells', 2013, pp. 22–25.
[24] F. Dimroth *et al.*, 'Four-Junction Wafer-Bonded Concentrator Solar Cells', *IEEE J. Photovolt.*, vol. 6, no. 1, pp. 343–349, Jan. 2016.
[25] M. Riede *et al.*, 'Efficient Organic Tandem Solar Cells based on Small Molecules', *Adv. Funct. Mater.*, vol. 21, no. 16, pp. 3019–3028, Aug. 2011.
[26] L. Dou *et al.*, 'Tandem polymer solar cells featuring a spectrally matched low-bandgap polymer', *Nat. Photonics*, vol. 6, no. 3, pp. 180–185, Feb. 2012.
[27] J. Üpping *et al.*, 'Three-Dimensional Photonic Crystal Intermediate Reflectors for Enhanced Light-Trapping in Tandem Solar Cells', *Adv. Mater.*, vol. 23, no. 34, pp. 3896–3900, Sep. 2011.
[28] J. H. Seo *et al.*, 'High Efficiency Inorganic/Organic Hybrid Tandem Solar Cells', *Adv. Mater.*, vol. 24, no. 33, pp. 4523–4527, Aug. 2012.
[29] N. J. Jeon *et al.*, 'Compositional engineering of perovskite materials for high-performance solar cells', *Nature*, vol. 517, no. 7535, pp. 476–480, Jan. 2015.
[30] D. P. McMeekin *et al.*, 'A mixed-cation lead mixed-halide perovskite absorber for tandem solar cells', *Science*, vol. 351, no. 6269, pp. 151–155, Jan. 2016.
[31] S. Foster and S. John, 'Light-trapping design for thin-film silicon-perovskite tandem solar cells', *J. Appl. Phys.*, vol. 120, no. 10, p. 103103, Sep. 2016.
[32] N.-G. Park, 'Crystal growth engineering for high efficiency perovskite solar cells', *CrystEngComm*, vol. 18, no. 32, pp. 5977–5985, 2016.
[33] 'Perovskite-silicon tandem solar cells reach 25.5% efficiency, https://www.perovskite-info.com/perovskite-silicon-tandem-solar-cells-reach-255-efficiency'. .
[34] A. S. Brown and M. A. Green, 'Detailed balance limit for the series constrained two terminal tandem solar cell', *Phys. E Low-Dimens. Syst. Nanostructures*, vol. 14, no. 1–2, pp. 96–100, Apr. 2002.
[35] M. Wolf, 'Limitations and Possibilities for Improvement of Photovoltaic Solar Energy Converters: Part I: Considerations for Earth's Surface Operation', *Proc. IRE*, vol. 48, no. 7, pp. 1246–1263, Jul. 1960.
[36] A. Luque and A. Martí, 'Increasing the Efficiency of Ideal Solar Cells by Photon Induced Transitions at Intermediate Levels', *Phys. Rev. Lett.*, vol. 78, no. 26, pp. 5014–5017, Jun. 1997.
[37] A. S. Brown, M. A. Green, and R. P. Corkish, 'Limiting efficiency for a multi-band solar cell containing three and four bands', *Phys. E Low-Dimens. Syst. Nanostructures*, vol. 14, no. 1–2, pp. 121–125, Apr. 2002.
[38] A. Martí, D. F. Marrón, and A. Luque, 'Evaluation of the efficiency potential of intermediate band solar cells based on thin-film chalcopyrite materials', *J. Appl. Phys.*, vol. 103, no. 7, p. 073706, Apr. 2008.
[39] M. Wiemer, V. Sabnis, and H. Yuen, '43.5% efficient lattice matched solar cells', 2011, vol. 8108, pp. 810804-810804–5.
[40] Y. Okada *et al.*, 'Increase in photocurrent by optical transitions via intermediate quantum states in direct-doped InAs/GaNAs strain-compensated quantum dot solar cell', *J. Appl. Phys.*, vol. 109, no. 2, p. 024301, Jan. 2011.
[41] N. López, L. A. Reichertz, K. M. Yu, K. Campman, and W. Walukiewicz, 'Engineering the Electronic Band Structure for Multiband Solar Cells', *Phys. Rev. Lett.*, vol. 106, no. 2, p. 028701, Jan. 2011.
[42] T. Tanaka *et al.*, 'Photocurrent induced by two-photon excitation in ZnTeO intermediate band solar cells', *Appl. Phys. Lett.*, vol. 102, no. 5, p. 052111, Feb. 2013.
[43] C. Malerba, C. L. Azanza Ricardo, M. D'Incau, F. Biccari, P. Scardi, and A. Mittiga, 'Nitrogen doped Cu_2O: A possible material for intermediate band solar cells?', *Sol. Energy Mater. Sol. Cells*, vol. 105, pp. 192–195, Oct. 2012.
[44] J. Ramanujam *et al.*, 'Inorganic photovoltaics – Planar and nanostructured devices', *Prog. Mater. Sci.*, vol. 82, pp. 294–404, Sep. 2016.

[45] P. Hiralal, H. E. Unalan, and G. A. J. Amaratunga, 'Nanowires for energy generation', *Nanotechnology*, vol. 23, no. 19, p. 194002, May 2012.
[46] B. M. Kayes, H. A. Atwater, and N. S. Lewis, 'Comparison of the device physics principles of planar and radial p-n junction nanorod solar cells', *J. Appl. Phys.*, vol. 97, no. 11, p. 114302, Jun. 2005.
[47] D.-C. Perng, J.-W. Chen, T.-T. Kao, and R.-P. Chang, 'Cu_2O growth characteristics on an array of ZnO nanorods for the nano-structured solar cells', *Surf. Coat. Technol.*, vol. 231, pp. 261–266, Sep. 2013.
[48] M. Abd-Ellah, J. P. Thomas, L. Zhang, and K. T. Leung, 'Enhancement of solar cell performance of p-Cu_2O/n-ZnO-nanotube and nanorod heterojunction devices', *Sol. Energy Mater. Sol. Cells*, vol. 152, pp. 87–93, Aug. 2016.
[49] T.-J. Hsueh, C.-L. Hsu, S.-J. Chang, P.-W. Guo, J.-H. Hsieh, and I.-C. Chen, 'Cu_2O/n-ZnO nanowire solar cells on ZnO:Ga/glass templates', *Scr. Mater.*, vol. 57, no. 1, pp. 53–56, Jul. 2007.
[50] J. Cui and U. J. Gibson, 'A Simple Two-Step Electrodeposition of Cu_2O/ZnO Nanopillar Solar Cells', *J. Phys. Chem. C*, vol. 114, no. 14, pp. 6408–6412, Apr. 2010.
[51] K. P. Musselman *et al.*, 'Strong Efficiency Improvements in Ultra-low-Cost Inorganic Nanowire Solar Cells', *Adv. Mater.*, vol. 22, no. 35, pp. E254–E258, Sep. 2010.
[52] J.-W. Chen, D.-C. Perng, and J.-F. Fang, 'Nano-structured Cu_2O solar cells fabricated on sparse ZnO nanorods', *Sol. Energy Mater. Sol. Cells*, vol. 95, no. 8, pp. 2471–2477, Aug. 2011.
[53] A. Werner and H. D. Hochheimer, 'High-pressure x-ray study of Cu_2O and Ag_2O', *Phys. Rev. B*, vol. 25, no. 9, pp. 5929–5934, May 1982.
[54] F. Yang, Y. Choi, P. Liu, D. Stacchiola, J. Hrbek, and J. A. Rodriguez, 'Identification of 5–7 Defects in a Copper Oxide Surface', *J. Am. Chem. Soc.*, vol. 133, no. 30, pp. 11474–11477, Aug. 2011.
[55] A. Martínez-Ruiz, M. G. Moreno, and N. Takeuchi, 'First principles calculations of the electronic properties of bulk Cu2O, clean and doped with Ag, Ni, and Zn', *Solid State Sci.*, vol. 5, no. 2, pp. 291–295, Feb. 2003.
[56] A. Soon, X.-Y. Cui, B. Delley, S.-H. Wei, and C. Stampfl, 'Native defect-induced multifarious magnetism in nonstoichiometric cuprous oxide: First-principles study of bulk and surface properties of $Cu_{2-\delta}O$', *Phys. Rev. B*, vol. 79, no. 3, Jan. 2009.
[57] H. Raebiger, S. Lany, and A. Zunger, 'Origins of the p -type nature and cation deficiency in Cu_2O and related materials', *Phys. Rev. B*, vol. 76, no. 4, Jul. 2007.
[58] Y. Tsur and I. Riess, 'Self-compensation in semiconductors', *Phys. Rev. B*, vol. 60, no. 11, pp. 8138–8146, Sep. 1999.
[59] R. J. Elliott, 'Symmetry of Excitons in Cu_2O', *Phys. Rev.*, vol. 124, no. 2, pp. 340–345, Oct. 1961.
[60] M. Nolan and S. D. Elliott, 'The p-type conduction mechanism in Cu2O: a first principles study', *Phys. Chem. Chem. Phys.*, vol. 8, no. 45, p. 5350, 2006.
[61] C. Malerba, F. Biccari, C. Leonor Azanza Ricardo, M. D'Incau, P. Scardi, and A. Mittiga, 'Absorption coefficient of bulk and thin film Cu_2O', *Sol. Energy Mater. Sol. Cells*, vol. 95, no. 10, pp. 2848–2854, Oct. 2011.
[62] A. Mittiga, E. Salza, F. Sarto, M. Tucci, and R. Vasanthi, 'Heterojunction solar cell with 2% efficiency based on a Cu2O substrate', *Appl. Phys. Lett.*, vol. 88, no. 16, p. 163502, Apr. 2006.
[63] T. Minami, Y. Nishi, T. Miyata, and J. Nomoto, 'High-Efficiency Oxide Solar Cells with ZnO/Cu_2O Heterojunction Fabricated on Thermally Oxidized Cu_2O Sheets', *Appl. Phys. Express*, vol. 4, no. 6, p. 062301, May 2011.
[64] Y. Liu, H. K. Turley, J. R. Tumbleston, E. T. Samulski, and R. Lopez, 'Minority carrier transport length of electrodeposited Cu_2O in ZnO/Cu_2O heterojunction solar cells', *Appl. Phys. Lett.*, vol. 98, no. 16, p. 162105, Apr. 2011.
[65] A. Paracchino, J. C. Brauer, J.-E. Moser, E. Thimsen, and M. Graetzel, 'Synthesis and Characterization of High-Photoactivity Electrodeposited Cu_2O Solar Absorber by Photoelectrochemistry and Ultrafast Spectroscopy', *J. Phys. Chem. C*, vol. 116, no. 13, pp. 7341–7350, Apr. 2012.

[66] F. Biccari, C. Malerba, and A. Mittiga, 'Chlorine doping of Cu_2O', *Sol. Energy Mater. Sol. Cells*, vol. 94, no. 11, pp. 1947–1952, Nov. 2010.
[67] S. Ishizuka and K. Akimoto, 'Control of the growth orientation and electrical properties of polycrystalline Cu_2O thin films by group-IV elements doping', *Appl. Phys. Lett.*, vol. 85, no. 21, pp. 4920–4922, Nov. 2004.
[68] Y. Nakano, S. Saeki, and T. Morikawa, 'Optical bandgap widening of p-type Cu_2O films by nitrogen doping', *Appl. Phys. Lett.*, vol. 94, no. 2, p. 022111, Jan. 2009.
[69] N. Kikuchi and K. Tonooka, 'Electrical and structural properties of Ni-doped Cu_2O films prepared by pulsed laser deposition', *Thin Solid Films*, vol. 486, no. 1–2, pp. 33–37, Aug. 2005.
[70] S. Ishizuka, S. Kato, Y. Okamoto, and K. Akimoto, 'Control of hole carrier density of polycrystalline Cu_2O thin films by Si doping', *Appl. Phys. Lett.*, vol. 80, no. 6, pp. 950–952, Feb. 2002.
[71] 'D. Trivich, E. Y. Wang, R. J. Komp, and A. S. Kakar, Proceedings of the 13th IEEE Photovoltaic Specialists Conference, Washington, DC (IEEE, New York, 1978), p. 174'. .
[72] Y. Nishi, T. Miyata, and T. Minami, 'The impact of heterojunction formation temperature on obtainable conversion efficiency in n-ZnO/p-Cu_2O solar cells', *Thin Solid Films*, vol. 528, pp. 72–76, Jan. 2013.
[73] S. Laidoudi *et al.*, 'Growth and characterization of electrodeposited Cu_2O thin films', *Semicond. Sci. Technol.*, vol. 28, no. 11, p. 115005, Nov. 2013.
[74] E. Fortin and D. Masson, 'Photovoltaic effects in Cu_2O/Cu solar cells grown by anodic oxidation', *Solid-State Electron.*, vol. 25, no. 4, pp. 281–283, Apr. 1982.
[75] H. Zhu, J. Zhang, C. Li, F. Pan, T. Wang, and B. Huang, 'Cu_2O thin films deposited by reactive direct current magnetron sputtering', *Thin Solid Films*, vol. 517, no. 19, pp. 5700–5704, Aug. 2009.
[76] S. Eisermann *et al.*, 'Copper oxide thin films by chemical vapor deposition: Synthesis, characterization and electrical properties', *Phys. Status Solidi A*, vol. 209, no. 3, pp. 531–536, Mar. 2012.
[77] T. Kosugi and S. Kaneko, 'Novel Spray-Pyrolysis Deposition of Cuprous Oxide Thin Films', *J. Am. Ceram. Soc.*, vol. 81, no. 12, pp. 3117–3124, Dec. 1998.
[78] S. Rühle *et al.*, 'Combinatorial solar cell libraries for the investigation of different metal back contacts for TiO_2 –Cu_2O hetero-junction solar cells', *Phys Chem Chem Phys*, vol. 16, no. 15, pp. 7066–7073, 2014.
[79] L. C. Olsen, R. C. Bohara, and M. W. Urie, 'Explanation for low-efficiency Cu_2O Schottky-barrier solar cells', *Appl. Phys. Lett.*, vol. 34, no. 1, pp. 47–49, Jan. 1979.
[80] L. O. Grondahl, 'The Copper-Cuprous-Oxide Rectifier and Photoelectric Cell', *Rev. Mod. Phys.*, vol. 5, no. 2, pp. 141–168, Apr. 1933.
[81] A. O. Musa, T. Akomolafe, and M. J. Carter, 'Production of cuprous oxide, a solar cell material, by thermal oxidation and a study of its physical and electrical properties', *Sol. Energy Mater. Sol. Cells*, vol. 51, no. 3–4, pp. 305–316, Feb. 1998.
[82] 'Economou, N.A. Toth, R.S. Komp R.J. and Trivich, D. (1982). Photovoltaic cells of electrodeposited cuprous oxide. 14th IEEE Photovoltaic Spec. Conf. Proc. New York: 1180-1185'. .
[83] C. Noguet *et al.*, 'Cuprous oxide as a photovoltaic converter', presented at the Photovoltaic Solar Energy Conference, 1978, pp. 1170–1179.
[84] L. M. Abrantes, L. M. Castillo, C. Norman, and L. M. Peter, 'A photoelectrochemical study of the anodic oxidation of copper in alkaline solution', *J. Electroanal. Chem. Interfacial Electrochem.*, vol. 163, no. 1–2, pp. 209–221, Mar. 1984.
[85] H.-H. Strehblow and B. Titze, 'The investigation of the passive behaviour of copper in weakly acid and alkaline solutions and the examination of the passive film by esca and ISS', *Electrochimica Acta*, vol. 25, no. 6, pp. 839–850, Jun. 1980.
[86] V. F. Drobny and L. Pulfrey, 'Properties of reactively-sputtered copper oxide thin films', *Thin Solid Films*, vol. 61, no. 1, pp. 89–98, Jul. 1979.

[87] J. Pinkas, J. C. Huffman, D. V. Baxter, M. H. Chisholm, and K. G. Caulton, 'Mechanistic Role of H_2O and the Ligand in the Chemical Vapor Deposition of Cu, Cu_2O, CuO, and Cu_3N from Bis(1,1,1,5,5,5-hexafluoropentane-2,4-dionato)copper(II)', *Chem. Mater.*, vol. 7, no. 8, pp. 1589–1596, Aug. 1995.
[88] T. Kosugi and S. Kaneko, 'Novel Spray-Pyrolysis Deposition of Cuprous Oxide Thin Films', *J. Am. Ceram. Soc.*, vol. 81, no. 12, pp. 3117–3124, Dec. 1998.
[89] A. Chen, H. Long, X. Li, Y. Li, G. Yang, and P. Lu, 'Controlled growth and characteristics of single-phase Cu_2O and CuO films by pulsed laser deposition', *Vacuum*, vol. 83, no. 6, pp. 927–930, Feb. 2009.
[90] T. Prasada Rao and M. C. Santhoshkumar, 'Effect of thickness on structural, optical and electrical properties of nanostructured ZnO thin films by spray pyrolysis', *Appl. Surf. Sci.*, vol. 255, no. 8, pp. 4579–4584, Feb. 2009.
[91] ü. Özgür *et al.*, 'A comprehensive review of ZnO materials and devices', *J. Appl. Phys.*, vol. 98, no. 4, p. 041301, Aug. 2005.
[92] P. Banerjee, W.-J. Lee, K.-R. Bae, S. B. Lee, and G. W. Rubloff, 'Structural, electrical, and optical properties of atomic layer deposition Al-doped ZnO films', *J. Appl. Phys.*, vol. 108, no. 4, p. 043504, Aug. 2010.
[93] *Jagadish, C., & Pearton, S. J. (Eds.). (2011). Zinc oxide bulk, thin films and nanostructures: processing, properties, and applications. Elsevier.* .
[94] W. J. Jeong, S. K. Kim, and G. C. Park, 'Preparation and characteristic of ZnO thin film with high and low resistivity for an application of solar cell', *Thin Solid Films*, vol. 506–507, pp. 180–183, May 2006.
[95] M. Suchea, S. Christoulakis, K. Moschovis, N. Katsarakis, and G. Kiriakidis, 'ZnO transparent thin films for gas sensor applications', *Thin Solid Films*, vol. 515, no. 2, pp. 551–554, Oct. 2006.
[96] Y. S. Lee *et al.*, 'Atomic Layer Deposited Gallium Oxide Buffer Layer Enables 1.2 V Open-Circuit Voltage in Cuprous Oxide Solar Cells', *Adv. Mater.*, vol. 26, no. 27, pp. 4704–4710, Jul. 2014.
[97] A. Goyal and S. Kachhwaha, 'ZnO thin films preparation by spray pyrolysis and electrical characterization', *Mater. Lett.*, vol. 68, pp. 354–356, Feb. 2012.
[98] C.-Y. Tsay, K.-S. Fan, Y.-W. Wang, C.-J. Chang, Y.-K. Tseng, and C.-K. Lin, 'Transparent semiconductor zinc oxide thin films deposited on glass substrates by sol–gel process', *Ceram. Int.*, vol. 36, no. 6, pp. 1791–1795, Aug. 2010.
[99] T. Tynell and M. Karppinen, 'Atomic layer deposition of ZnO: a review', *Semicond. Sci. Technol.*, vol. 29, no. 4, p. 043001, Apr. 2014.
[100] P. Bilkova, J. Zemek, B. Mitu, V. Marotta, and S. Orlando, 'Deposition of zinc oxide thin films by reactive pulsed laser ablation', *Appl. Surf. Sci.*, vol. 252, no. 13, pp. 4604–4609, Apr. 2006.
[101] T. Minami, H. Nanto, and S. Takata, 'Highly conductive and transparent zinc oxide films prepared by rf magnetron sputtering under an applied external magnetic field', *Appl. Phys. Lett.*, vol. 41, no. 10, pp. 958–960, Nov. 1982.
[102] H. Sato, T. Minami, T. Miyata, S. Takata, and M. Ishii, 'Transparent conducting ZnO thin films prepared on low temperature substrates by chemical vapour deposition using $Zn(C_5H_7O_2)_2$', *Thin Solid Films*, vol. 246, no. 1–2, pp. 65–70, Jun. 1994.
[103] O. Fouad, A. Ismail, Z. Zaki, and R. Mohamed, 'Zinc oxide thin films prepared by thermal evaporation deposition and its photocatalytic activity', *Appl. Catal. B Environ.*, vol. 62, no. 1–2, pp. 144–149, Jan. 2006.
[104] A. Janotti and C. G. Van de Walle, 'Fundamentals of zinc oxide as a semiconductor', *Rep. Prog. Phys.*, vol. 72, no. 12, p. 126501, Dec. 2009.
[105] L. S. Vlasenko and G. D. Watkins, 'Optical detection of electron paramagnetic resonance for intrinsic defects produced in ZnO by 2.5-MeV electron irradiation ***in situ*** at 4.2 K', *Phys. Rev. B*, vol. 72, no. 3, Jul. 2005.
[106] L. S. Vlasenko and G. D. Watkins, 'Optical detection of electron paramagnetic resonance in room-temperature electron-irradiated ZnO', *Phys. Rev. B*, vol. 71, no. 12, Mar. 2005.

[107] A. Janotti and C. G. Van de Walle, 'Oxygen vacancies in ZnO', *Appl. Phys. Lett.*, vol. 87, no. 12, p. 122102, Sep. 2005.
[108] C. G. Van de Walle and J. Neugebauer, 'Universal alignment of hydrogen levels in semiconductors, insulators and solutions', *Nature*, vol. 423, no. 6940, pp. 626–628, Jun. 2003.
[109] A. Ohtomo *et al.*, '$Mg_xZn_{1-x}O$ as a II–VI widegap semiconductor alloy', *Appl. Phys. Lett.*, vol. 72, no. 19, pp. 2466–2468, May 1998.
[110] A. Kaushal, D. Pathak, R. K. Bedi, and D. Kaur, 'Structural, electrical and optical properties of transparent $Zn_{1-x}Mg_xO$ nanocomposite thin films', *Thin Solid Films*, vol. 518, no. 5, pp. 1394–1398, Dec. 2009.
[111] S. Choopun, R. D. Vispute, W. Yang, R. P. Sharma, T. Venkatesan, and H. Shen, 'Realization of band gap above 5.0 eV in metastable cubic-phase $Mg_xZn_{1-x}O$ alloy films', *Appl. Phys. Lett.*, vol. 80, no. 9, pp. 1529–1531, Mar. 2002.
[112] Z. Duan, A. Du Pasquier, Y. Lu, Y. Xu, and E. Garfunkel, 'Effects of Mg composition on open circuit voltage of Cu_2O–$Mg_xZn_{1-x}O$ heterojunction solar cells', *Sol. Energy Mater. Sol. Cells*, vol. 96, pp. 292–297, Jan. 2012.
[113] R. E. Brandt *et al.*, 'Band offsets of *n* -type electron-selective contacts on cuprous oxide (Cu_2O) for photovoltaics', *Appl. Phys. Lett.*, vol. 105, no. 26, p. 263901, Dec. 2014.
[114] G. P. Pollack and D. Trivich, 'Photoelectric properties of cuprous oxide', *J. Appl. Phys.*, vol. 46, no. 1, pp. 163–172, Jan. 1975.
[115] L. C. Olsen, F. W. Addis, and W. Miller, 'Experimental and theoretical studies of Cu_2O solar cells', *Sol. Cells*, vol. 7, no. 3, pp. 247–279, Dec. 1982.
[116] R. J. Iwanowski and D. Trivich, 'The influence of hydrogen ion bombardment on the photovoltaic properties of Cu/Cu $_2$ O schottky barrier solar cells', *Radiat. Eff.*, vol. 76, no. 3, pp. 87–92, Jan. 1983.
[117] R. J. Iwanowski and D. Trivih, 'Cu/Cu2O Schottky barrier solar cells prepared by multistep irradiation of a Cu_2O substrate by H+ ions', *Sol. Cells*, vol. 13, no. 3, pp. 253–264, Jan. 1985.
[118] J. Herion, E. A. Niekisch, and G. Scharl, 'Investigation of metal oxide/cuprous oxide heterojunction solar cells', *Sol. Energy Mater.*, vol. 4, no. 1, pp. 101–112, Dec. 1980.
[119] L. Papadimitriou, N. A. Economou, and D. Trivich, 'Heterojunction solar cells on cuprous oxide', *Sol. Cells*, vol. 3, no. 1, pp. 73–80, Feb. 1981.
[120] H. Tanaka, T. Shimakawa, T. Miyata, H. Sato, and T. Minami, 'Electrical and optical properties of TCO–Cu_2O heterojunction devices', *Thin Solid Films*, vol. 469–470, pp. 80–85, Dec. 2004.
[121] K. Akimoto, S. Ishizuka, M. Yanagita, Y. Nawa, G. K. Paul, and T. Sakurai, 'Thin film deposition of Cu_2O and application for solar cells', *Sol. Energy*, vol. 80, no. 6, pp. 715–722, Jun. 2006.
[122] T. Minami, Y. Nishi, T. Miyata, and S. Abe, 'Photovoltaic Properties in Al-doped ZnO/non-doped Zn1-XMgXO/Cu2O Heterojunction Solar Cells', *ECS Trans.*, vol. 50, no. 51, pp. 59–68, Apr. 2013.
[123] T. Minami, Y. Nishi, and T. Miyata, 'High-Efficiency Cu_2O-Based Heterojunction Solar Cells Fabricated Using a Ga_2 O_3 Thin Film as N-Type Layer', *Appl. Phys. Express*, vol. 6, no. 4, p. 044101, Apr. 2013.
[124] T. Minami, Y. Nishi, and T. Miyata, 'Heterojunction solar cell with 6% efficiency based on an n-type aluminum–gallium–oxide thin film and p-type sodium-doped Cu_2O sheet', *Appl. Phys. Express*, vol. 8, no. 2, p. 022301, Feb. 2015.
[125] M. Izaki, T. Shinagawa, K.-T. Mizuno, Y. Ida, M. Inaba, and A. Tasaka, 'Electrochemically constructed p-Cu_2O/n-ZnO heterojunction diode for photovoltaic device', *J. Phys. Appl. Phys.*, vol. 40, no. 11, pp. 3326–3329, Jun. 2007.
[126] Y. S. Lee *et al.*, 'Ultrathin amorphous zinc-tin-oxide buffer layer for enhancing heterojunction interface quality in metal-oxide solar cells', *Energy Environ. Sci.*, vol. 6, no. 7, p. 2112, 2013.
[127] S. W. Lee *et al.*, 'Improved Cu_2O-Based Solar Cells Using Atomic Layer Deposition to Control the Cu Oxidation State at the p-n Junction', *Adv. Energy Mater.*, vol. 4, no. 11, p. 1301916, Aug. 2014.
[128] K. Wasa, 'Sputtering Phenomena', in *Handbook of Sputtering Technology*, Elsevier, 2012, pp. 41–75.

[129] R. G. Ehl and A. J. Ihde, 'Faraday's electrochemical laws and the determination of equivalent weights', *J. Chem. Educ.*, vol. 31, no. 5, p. 226, May 1954.
[130] Piero Zanello, *Inorganic Electrochemistry*. The Royal Society of Chemistry, 2003.
[131] A. J. Bard and L. R. Faulkner, *Electrochemical methods: fundamentals and applications*, 2. ed. Hoboken, NJ: Wiley, 2001.
[132] D. Pletcher and University of Southampton, Eds., *Instrumental methods in electrochemistry*, Repr. Oxford: Woodhead Publ, 2011.
[133] B. Scharifker and G. Hills, 'Theoretical and experimental studies of multiple nucleation', *Electrochimica Acta*, vol. 28, no. 7, pp. 879–889, Jul. 1983.
[134] 'Wiley: Fundamentals of Electrochemical Deposition, 2nd Edition - Milan Paunovic, Mordechay Schlesinger'. [Online]. Available: http://www.wiley.com/WileyCDA/WileyTitle/productCd-0471712213.html. [Accessed: 26-Jan-2017].
[135] T. Suntola, 'Atomic layer epitaxy', *Mater. Sci. Rep.*, vol. 4, no. 5, pp. 261–312, Jan. 1989.
[136] 'Method for producing compound thin films'.
[137] 'T. Suntola, J. Antson, International patent, FIN 52359, US 4 058 430, priority Nov 29, 1974 , publication Nov 15, 1977'. .
[138] R. L. Puurunen, 'Growth Per Cycle in Atomic Layer Deposition: A Theoretical Model', *Chem. Vap. Depos.*, vol. 9, no. 5, pp. 249–257, Oct. 2003.
[139] 'CompleteEASE Manual - Ellipsometry_manual.pdf'. [Online]. Available: https://physlab.lums.edu.pk/images/f/f4/Ellipsometry_manual.pdf. [Accessed: 31-Jan-2017].
[140] M. Eckert, 'Max von Laue and the discovery of X-ray diffraction in 1912', *Ann. Phys.*, vol. 524, no. 5, pp. A83–A85, May 2012.
[141] W. Zhou and Z. L. Wang, Eds., *Scanning microscopy for nanotechnology: techniques and applications*. New York, NY: Springer, 2007.
[142] J. Tauc, 'Optical properties and electronic structure of amorphous Ge and Si', *Mater. Res. Bull.*, vol. 3, no. 1, pp. 37–46, Jan. 1968.
[143] K. Siegbahn and K. Edvarson, 'β-Ray spectroscopy in the precision range of 1 : 105', *Nucl. Phys.*, vol. 1, no. 8, pp. 137–159, Jan. 1956.
[144] P. van der Heide, *X-Ray Photoelectron Spectroscopy: An Introduction to Principles and Practices*. Hoboken, NJ, USA: John Wiley & Sons, Inc., 2011.
[145] 'Charles C Chusuei and D Wayne Goodman. X-ray photoelectron spec- troscopy. Encyclopedia of physical science and technology , 17:921–938, 2002.', .
[146] E. A. Kraut, R. W. Grant, J. R. Waldrop, and S. P. Kowalczyk, 'Semiconductor core-level to valence-band maximum binding-energy differences: Precise determination by x-ray photoelectron spectroscopy', *Phys. Rev. B*, vol. 28, no. 4, pp. 1965–1977, Aug. 1983.
[147] J. Matthew, 'Surface analysis by Auger and x-ray photoelectron spectroscopy. D. Briggs and J. T. Grant (eds). IMPublications, Chichester, UK and SurfaceSpectra, Manchester, UK, 2003. 900 pp., ISBN 1-901019-04-7, 900 pp', *Surf. Interface Anal.*, vol. 36, no. 13, pp. 1647–1647, 2004.
[148] Y. S. Lee *et al.*, 'Nitrogen-doped cuprous oxide as a p-type hole-transporting layer in thin-film solar cells', *J. Mater. Chem. A*, vol. 1, no. 48, p. 15416, 2013.
[149] Y. Park, V. Choong, Y. Gao, B. R. Hsieh, and C. W. Tang, 'Work function of indium tin oxide transparent conductor measured by photoelectron spectroscopy', *Appl. Phys. Lett.*, vol. 68, no. 19, pp. 2699–2701, May 1996.
[150] H. B. Michaelson, 'The work function of the elements and its periodicity', *J. Appl. Phys.*, vol. 48, no. 11, pp. 4729–4733, Nov. 1977.
[151] D. R. Lide and Chemical Rubber Company, Eds., *CRC handbook of chemistry and physics: a ready-reference book of chemical and physical data*, 90. ed., 2009–2010. Boca Raton, FLa.: CRC Press, 2009.
[152] J. Vancea, G. Reiss, F. Schneider, K. Bauer, and H. Hoffmann, 'Substrate effects on the surface topography of evaporated gold films—A scanning tunnelling microscopy investigation', *Surf. Sci.*, vol. 218, no. 1, pp. 108–126, Aug. 1989.

[153] C. H. F. Peden, K. B. Kidd, and N. D. Shinn, 'Metal/metal-oxide interfaces: A surface science approach to the study of adhesion', *J. Vac. Sci. Technol. Vac. Surf. Films*, vol. 9, no. 3, pp. 1518–1524, May 1991.
[154] T.-M. Wu, J.-Z. Tong, J.-H. J. Hsieh, and Y. S. Yang, 'Improvement of interfacial adhesion of Al/Cr films deposited on indium tin oxide coated glasses by interfacial oxidation', *Surf. Coat. Technol.*, vol. 183, no. 1, pp. 89–95, May 2004.
[155] K. Nakaoka and K. Ogura, 'Electrochemical Preparation of p-Type Cupric and Cuprous Oxides on Platinum and Gold Substrates from Copper(II) Solutions with Various Amino Acids', *J. Electrochem. Soc.*, vol. 149, no. 11, p. C579, 2002.
[156] R. P. Wijesundera, M. Hidaka, K. Koga, M. Sakai, and W. Siripala, 'Growth and characterisation of potentiostatically electrodeposited Cu_2O and Cu thin films', *Thin Solid Films*, vol. 500, no. 1–2, pp. 241–246, Apr. 2006.
[157] P. Sharma and H. S. Bhatti, 'Synthesis of fluorescent hollow and porous Cu_2O nanopolyhedras in the presence of poly(vinyl pyrrolidone)', *Mater. Chem. Phys.*, vol. 114, no. 2–3, pp. 889–896, Apr. 2009.
[158] T. D. Golden, M. G. Shumsky, Y. Zhou, R. A. VanderWerf, R. A. Van Leeuwen, and J. A. Switzer, 'Electrochemical Deposition of Copper(I) Oxide Films', *Chem. Mater.*, vol. 8, no. 10, pp. 2499–2504, Jan. 1996.
[159] M. Izaki, T. Shinagawa, K.-T. Mizuno, Y. Ida, M. Inaba, and A. Tasaka, 'Electrochemically constructed p-Cu_2O/n-ZnO heterojunction diode for photovoltaic device', *J. Phys. Appl. Phys.*, vol. 40, no. 11, pp. 3326–3329, Jun. 2007.
[160] P. E. de Jongh, D. Vanmaekelbergh, and J. J. Kelly, 'Cu_2O: Electrodeposition and Characterization', *Chem. Mater.*, vol. 11, no. 12, pp. 3512–3517, Dec. 1999.
[161] R. Guidelli *et al.*, 'Defining the transfer coefficient in electrochemistry: An assessment (IUPAC Technical Report)', *Pure Appl. Chem.*, vol. 86, no. 2, Jan. 2014.
[162] L. Guo, G. Oskam, A. Radisic, P. M. Hoffmann, and P. C. Searson, 'Island growth in electrodeposition', *J. Phys. Appl. Phys.*, vol. 44, no. 44, p. 443001, Nov. 2011.
[163] L. Guo and P. C. Searson, 'On the influence of the nucleation overpotential on island growth in electrodeposition', *Electrochimica Acta*, vol. 55, no. 13, pp. 4086–4091, May 2010.
[164] 'L. Wang, U. of T. at A. ProQuest Dissertations and Theses (Electronic resource collection), College of Engineering, Preparation and characterization of properties of electrodeposited copper oxide films, 2006'. .
[165] S. I. Boldish and W. B. White, 'Optical band gaps of selected ternary sulfide minerals', *Am. Mineral.*, vol. 83, no. 7–8, pp. 865–871, Aug. 1998.
[166] T. Dimopoulos, A. Peić, S. Abermann, M. Postl, E. J. W. List-Kratochvil, and R. Resel, 'Effect of thermal annealing in vacuum on the photovoltaic properties of electrodeposited Cu_2O-absorber solar cell', *EPJ Photovolt.*, vol. 5, p. 50301, 2014.
[167] N. Huby, S. Ferrari, E. Guziewicz, M. Godlewski, and V. Osinniy, 'Electrical behavior of zinc oxide layers grown by low temperature atomic layer deposition', *Appl. Phys. Lett.*, vol. 92, no. 2, p. 023502, Jan. 2008.
[168] E. Guziewicz *et al.*, 'ZnO grown by atomic layer deposition: A material for transparent electronics and organic heterojunctions', *J. Appl. Phys.*, vol. 105, no. 12, p. 122413, Jun. 2009.
[169] M. A. Thomas and J. B. Cui, 'Highly Tunable Electrical Properties in Undoped ZnO Grown by Plasma Enhanced Thermal-Atomic Layer Deposition', *ACS Appl. Mater. Interfaces*, vol. 4, no. 6, pp. 3122–3128, Jun. 2012.
[170] E. Guziewicz *et al.*, 'ALD grown zinc oxide with controllable electrical properties', *Semicond. Sci. Technol.*, vol. 27, no. 7, p. 074011, Jul. 2012.
[171] D. Briggs, 'Handbook of X-ray Photoelectron Spectroscopy C. D. Wanger, W. M. Riggs, L. E. Davis, J. F. Moulder and G. E.Muilenberg Perkin-Elmer Corp., Physical Electronics Division, Eden Prairie, Minnesota, USA, 1979. 190 pp. $195', *Surf. Interface Anal.*, vol. 3, no. 4, pp. v–v, Aug. 1981.

[172] S. R. Achary *et al.*, 'Self-assembled $Mg_xZn_{1-x}O$ quantum dots ($0 \leq x \leq 1$) on different substrates using spray pyrolysis methodology', *CrystEngComm*, vol. 15, no. 1, pp. 182–191, 2013.
[173] *B.V. Crist, Handbook of Monochromatic XPS spectra, Wiley, Chichester; New York, 2000*. .
[174] M. Gabás *et al.*, 'Unraveling the conduction mechanism of Al-doped ZnO films by valence band soft x-ray photoemission spectroscopy', *Appl. Phys. Lett.*, vol. 86, no. 4, p. 042104, Jan. 2005.
[175] A. Suryanarayana Reddy, P. Prathap, Y. P. V. Subbaiah, K. T. Ramakrishna Reddy, and J. Yi, 'Growth and physical behaviour of $Zn_{1-x}Mg_xO$ films', *Thin Solid Films*, vol. 516, no. 20, pp. 7084–7087, Aug. 2008.
[176] A. Kaushal and D. Kaur, 'Effect of Mg content on structural, electrical and optical properties of $Zn_{1-x}Mg_xO$ nanocomposite thin films', *Sol. Energy Mater. Sol. Cells*, vol. 93, no. 2, pp. 193–198, Feb. 2009.
[177] 'André Bikowski,, The relation between the deposition process and the structural, electronic, and transport properties of magnetron sputtered doped ZnO and $Zn_{1-x}Mg_xO$ films, Mathematisch -Naturwissenschaftlichen Fakultät I der Humboldt- Universität zu Berlin, 2014.' .
[178] T. Han, F. Y. Meng, S. Zhang, X. M. Cheng, and J. I. Oh, 'Band gap and electronic properties of wurtzite-structure ZnO co-doped with *IIA* and *IIIA*', *J. Appl. Phys.*, vol. 110, no. 6, p. 063724, Sep. 2011.
[179] A. Janotti and C. G. Van de Walle, 'Absolute deformation potentials and band alignment of wurtzite ZnO, MgO, and CdO', *Phys. Rev. B*, vol. 75, no. 12, Mar. 2007.
[180] X. D. Zhang *et al.*, 'First-principles investigation of electronic and optical properties in wurtzite $Zn_{1-x}Mg_xO$', *Eur. Phys. J. B*, vol. 62, no. 4, pp. 417–421, Apr. 2008.
[181] M. Ichimura and Y. Song, 'Band Alignment at the Cu_2O/ZnO Heterojunction', *Jpn. J. Appl. Phys.*, vol. 50, no. 5, p. 051002, May 2011.
[182] S. S. Wilson, J. P. Bosco, Y. Tolstova, D. O. Scanlon, G. W. Watson, and H. A. Atwater, 'Interface stoichiometry control to improve device voltage and modify band alignment in ZnO/Cu_2O heterojunction solar cells', *Energy Env. Sci*, vol. 7, no. 11, pp. 3606–3610, Sep. 2014.
[183] D. . Zhang, Y. . Liu, Y. . Liu, and H. Yang, 'The electrical properties and the interfaces of Cu_2O/ZnO/ITO p–i–n heterojunction', *Phys. B Condens. Matter*, vol. 351, no. 1–2, pp. 178–183, Aug. 2004.
[184] C.-S. Lee, S. Kim, Y.-M. Shin, B. G. Park, B. T. Ahn, and H. Kwon, 'Performance improvement in Cd-free Cu(In,Ga)Se_2 solar cells by modifying the electronic structure of the ZnMgO buffer layer', *RSC Adv.*, vol. 4, no. 69, p. 36784, Aug. 2014.
[185] M. Trunk, V. Venkatachalapathy, A. Galeckas, and A. Y. Kuznetsov, 'Deep level related photoluminescence in ZnMgO', *Appl. Phys. Lett.*, vol. 97, no. 21, p. 211901, Nov. 2010.
[186] Y. Takiguchi and S. Miyajima, 'Device simulation of cuprous oxide heterojunction solar cells', *Jpn. J. Appl. Phys.*, vol. 54, no. 11, p. 112303, Nov. 2015.
[187] R. R. King *et al.*, 'Band gap-voltage offset and energy production in next-generation multijunction solar cells', *Prog. Photovolt. Res. Appl.*, vol. 19, no. 7, pp. 797–812, Nov. 2011.
[188] 'FDTD Solutions 7.5 (Lumerical, 2011)'.
[189] 'refractive index database, https://refractiveindex.info/'.

Conferences/Publications

Conferences:

- **Quantsol**, European summer school on solar cells, Germany 07-14.09.2014.
- **Poster presentation** at the E-MRS 2015 Conference in Lille, France, 11-15.05.2015, “Solar cells based on electrodeposited cuprous oxide absorber and ALD-grown ZnO”.
- **Oral presentation** at the E-MRS 2016 Conference in Lille, France 02-06.05.2016, "Properties of Mg-doped ZnO films grown by atomic layer deposition".

Publications:

- All-oxide solar cells based on electrodeposited Cu_2O absorber and atomic layer deposited ZnMgO on precious-metal-free electrode, **J. Kaur**, O. Bethge, N. Bansal, A. R. Wibowo, M. Bauch, R. Hamid, E. Bertagnolli, T. Dimopoulos, Solar Energy Materials and Solar Cells, 161,449 (2017).
- Solution-processed all-oxide solar cell based on electrodeposited Cu_2O and ZnMgO by spray pyrolysis, N. Winkler, S. Edinger, **J. Kaur**, R. A. Wibowo, W. Kautek, T. Dimopoulos, Journal of Materials Science, DOI: 10.1007/s10853-018-2482-2 (2018).